THERMAL EMISSION FROM NANOPLASMONIC STRUCTURES IN NEAR- AND FAR-FIELDS: NUMERICAL SIMULATION, DEVICE FABRICATION, AND CHARACTERIZATION

Submitted in partial fulfillment of the requirement for

the degree of

Doctor of Philosophy

in

Department of Engineering

Bowen Yu

B.S., School of Mechatronics Engineering, Harbin Institute of Technology

M.S., School of Mechatronics Engineering, Harbin Institute of Technology

Carnegie Mellon University

Pittsburgh, PA

February 2021

ACKNOWLEDGEMENTS

First of all, I would like to show my genuine gratitude to my PhD advisor, Prof. Sheng Shen (Committee chair). During my PhD study, he was extensively involved in every aspect of my research and gave me his insightful suggestion and guidance. His attitude on pushing the ultimate limit and pursuing the truth of engineering and technology, as well as his strictness on our research helped me grow tremendously in my academic career development as a researcher and an engineering PhD student. Apart from the research and school work, he also gave me his valuable guidance on my personal life and shared his own experience to inspire me. And all those helped me go through this challenging yet meaningful PhD experience.

I would like to thank Prof. Maysam Chamanzar, Prof. Paul R. Ohodnicki, and Prof. Xu Zhang for being on my thesis committee and giving me their insightful and earnest suggestions to my research and future career. I would like to express my appreciation to Prof. Paul R. Ohodnicki, Prof. Maysam Chamanzar, Prof. Xu Zhang, for the support and advice on my research of thermal emission from nanoplasmonic structures in near- and far fields. Their inspirational advice helped me walk through the hardest time during my PhD.

I would like to express my gratitude to all of my colleagues for their support and all the technicians, professionals, staff members I have interacted not just at CMU but also all over the states. In particular, the encouragement and insight I received from Pengfei Li, Baoan Liu, Jiawei Shi, Wei Gong, Ramesh Shrestha, Jiayu, Phil Smith, Laisuo Su, Yuxuan Luan, Xiao Luo, Kun Kim, Shen Du, Xiu Liu, Lin Jing, Yang Li, Michael Whiston, Qiyun Xu, Lutong Cai, Xiaonan Huang, Yong Zhuang, Ke Wang, Wenhuan Sun, Chenyu Wang, Tong Lv, Simon Lu, Kevin Parrish, Yue Teng, Leiming Hu, Xiao Ling, Josh Gyory, Ernest Kabuye, Justin Bobo, Zeikun Lv, Dongwen

Wu, Wei Chen, Zane Zheng, Mario Quinn Lyles, Tom Fitzgerald, Jose Caraballo and all staff members the nanofab, material characterization and machine shop are highly appreciated. I feel honored to have shared this experience with each of them. I would like to acknowledge the funding support from National Science Foundation (Grant no. CBET-1931964) and Steinbrenner Doctoral Fellowship from Carnegie Mellon University for my research on thermal emission.

Lastly, my sincere thanks goes to my family and friends. I am so thankful that I was surrounded positive people who love me no matter what, support me when I was really frustrated and depressed. Lastly, I am blessed that all the great and good people around that helped me through this meaningful PhD and all the hard work and dedication have paid off.

ABSTRACT

Thermal radiation originates from photons which are spontaneously emitted by different points in a thermal source. All matter with a temperature greater than 0K emits thermal radiation, which in turn can extract temperature distribution for all optical and electronic materials and devices. The classic model was found by Max Planck, which describes the spectral density of electromagnetic radiation emitted by a blackbody in the thermal equilibrium at a given temperature. A blackbody is an ideal emitter which absorbs all incident electromagnetic radiation from all frequencies and angles of incidence. All other emissions are studied with the reference of the blackbody following the properties of emission and absorption. Emissivity is core in thermal devices, both source and receiver. Thermal emission is a fundamental phenomenon for which any object with temperature greater than absolute zero emits energy in the form of electromagnetic waves. The thermal emission from a blackbody (an ideal thermal emitter) only depends on its temperature, as described by Planck's law. For a nonideal thermal emitter, i.e., a gray body, thermal emission also depends on how effectively the emitter can radiate, quantified as its emissivity.

In this dissertation, I systematically investigate the thermal emission from nanoplamonic structures in both near- and far-field regimes such as metasurfaces, 2D materials, single plasmonic emitter, etc. I implement numerical simulations to investigate the directional control of narrow-band perfect thermal emission using a nanoscale Yagi–Uda antenna consisting of an array of nanowires. Then I fabricate single plasmonic device and plasmonic structures via the state-of-the-art micro and nanofabrication techniques including electron beam (e-beam) lithography, photolithography, e-beam evaporation, reactive ion etching (RIE), wet etching, focused ion beam

(FIB), etc. Finally, I demonstrate the unique properties of the nanoplasmonic structures we fabricate via thermal and optical characterization.

TABLE OF CONTENTS

LIST OF TABLES

LIST OF FIGURES

Figure 2-1 (a) Spatial distribution of the far field thermal emission from a single gold nanorod emitter. The plotted physical quantity is the normalized $|E|^2$ with respect to the peak

1 Introduction

1.1 Background and overview

All matter with a temperature greater 0K emits thermal radiation, which in turn can extract temperature distribution for all optical and electronic materials and devices. Thermal emission, which physically originates from the electromagnetic waves emitted from thermally induced random currents in materials, plays a vital role in many fields, such as energy conversion [1-6], infrared sensing [7,8], passive radiative cooling [9-14], and thermal management [15-21]. In recent years, structures consisting of an array of subwavelength nanoplasmonic thermal emitters have emerged as an important platform to actively control and manipulate far- and near-field thermal radiation [21-34]. Nanoplasmonic structures prove to be the ideal platform to control thermal radiation. The understanding of the thermal emission from nanoplamonic structures is still relatively immature in the aspects of numerical modeling, device fabrication characterization.

Thermal emission can be of great importance in many applications, such as energy harvesting, infrared sensing and imaging, thermophotovoltaics, and thermal management. In those applications, the ability to control thermal emission is critically important since the thermal emission by nature is incoherent, random and not 'organized'. For instance, the conventional thermal emission, such as incandescence, is typically incoherent, broadband, and unpolarized. These characteristics impose strong restrictions on the capability of controlling thermal emission. More importantly, the emission spectrum in infrared sensing should be narrow-band around the targeted frequency. Also, thermal emission from bulk materials is well studied either in the context of thermodynamics or heat transfer using phenomenological concepts like emissivity or in the

framework of classical electrodynamics, but there remains a significant gap in our understanding of thermal radiation at the nanoscale.

In contrast, nanoplasmonic structures, have the potential to radiate thermal emission dramatically different from conventional correspondents, which would be of great importance for further application. Even though the field of plasmonics has been well studied and developed in the past, the thermal emission from nanoplasmonic structures is still in the early stage. Due to the intrinsic difficulty of controlling thermal emission, the design principle for conventional nanoplamonic structures cannot be directly applied to thermal emission. Therefore, it is imperative to develop the methodology to design thermal emission from nanoplasmonic structures via numerical simulation, experimentation and testing. In this proposal, we dive deeply into the unique thermal emission properties of a nanoplamonic structures from the aspects of simulation, experimentation and testing, and the thermal emission of nanoplasmonic structures would be studied in both near- and far-fields, respectively.

1.2 Motivation and scope

The motivation of this dissertation is to study the thermal emission from the nanoplasmonic structures in both near- and far-field, such as metamaterial, metasurfaces, plasmonic emitters, etc. To achieve this goal, I first implement numerical simulations to investigate the directional control of narrow-band perfect thermal emission using a nanoscale Yagi–Uda antenna consisting of an array of nanowires. Then, I design and fabricate a single plasmonic device and plasmonic array structures via the state-of-the-art micro and nanofabrication including electron beam (e-beam) lithography, photolithography, e-beam evaporation, reactive ion etching (RIE), wet etching, focused ion beam (FIB), etc. Finally, I utilize the commercial system including microscope, FTIR, lock-in amplifier, etc. to demonstrate the unique properties of the nanoplasmonic structures via

thermal and optical measurement. Chapters of this dissertation are arranged in the following manner:

Chapter 2 presents the study of the far-field thermal emission from nanoplasmonic structures. I start from the demonstration of the directional control of narrow-band thermal emission from nanoantennas in the far-field regime via numerical simulation. Then, the optimal design of the thermal Yagi-Uda antenna is well studied and developed, which would be a promising platform for controlling the directionality of thermal infrared sources. Then, I study the thermal emission from nanoplasmonic thermal emitters and the nanoplasmonic structures we made and present a narrow-band spectrum with ultra-high emissivity. The optical measurement characterization is conducted via our modified FTIR system, lock-in amplifier, and circuit design. Also, large-scale single plasmonic structure demonstrates a unique peak spectrum related to its dimension.

Chapter 3 presents the study of the near-field thermal emission from nanoplasmonic structures. I fabricate the emitter and detector system on a chip for near-field thermal radiation from nanoplasmonic structures. The near-field emission is largely enhanced due to the plasmonic cavity design. Thermal and mechanical performance analyses of the nanoplasmonic device in the near-field radiation regime are conducted to demonstrate the validity and feasibility for the experiment. Then, the state-of-the-art nanofabrication is employed to fabricate the near-field nanowire system. Lastly, the thermal measurement is performed to characterize the device performance.

Chapter 4 concludes the major contributions of the dissertation. The further work is also discussed in this chapter.

2 Far-field thermal emission from nanoplasmonic structures

2.1 Overview

The spectral and directional control of thermal emission remains challenging because thermal emission is generally spatially and spectrally incoherent. However, by utilizing nanoplamonic structures, it has been recently demonstrated that thermal radiation can have both spatial and spectral coherence. Costantini et al. [35] used plasmonic metasurfaces to realize the directional and frequency selective thermal emission. Ribaudo et al. [36] showed that two-dimensional silicon structures can emit highly directional thermal emission. Campione et al. [37] experimentally achieved directional and monochromatic thermal emission at epsilon-near-zero conditions in semiconductor hyperbolic metamaterials. As highly directional emitting structures, Yagi–Uda antennas have been investigated and widely used for decades [38-45]. A Yagi–Uda antenna usually consists of a single driven element as the feed, a reflector, and several directors on either side of the feed to optimize and control the directionality of electromagnetic emission. With both continuous device miniaturization and growing demand on precise control of directionality, nanoscale Yagi–Uda antennas become increasingly important [46-54]. Kosako et al. [55] experimentally demonstrated the directional light emission from a nano-optical Yagi–Uda antenna composed of an array of finely tuned gold nanorods. Taminiau et al. numerically showed that the interaction of a single quantum emitter with electromagnetic fields can be enhanced by coupling with resonant plasmon modes in the near field. The angular emission of the coupled system is highly directed and determined by the design of the nanoscale Yagi–Uda antenna [56]. Although these nanoscale Yagi–Uda antennas have achieved the directional control in the traditional optical and radio frequency regimes, the directional control of thermal emission with a narrow-band spectrum remains a challenge. In this work, we investigate the directional control of narrow-band

perfect thermal emission using a nanoscale Yagi–Uda antenna consisting of an array of nanowires via numerical simulations. Based on nanoscale transmission line resonators as well as the design of Yagi–Uda antennas [57], we numerically demonstrate the directional tunablity of the narrow-band thermal emission from a nanoscale Yagi–Uda antenna. Direct simulation of thermal emission is obtained by the Wiener chaos expansion method [58,59] and further optimized by our recently developed quasi-normal mode (QNM) theory [60-64]. Our results clearly indicate that the nanoscale Yagi–Uda antenna array would be a promising component for the directional control of thermal infrared sources, infrared sensors, etc.

2.2 Directional control of narrow-band thermal emission from nanoantennas in the far-field

To detect the sensing signals of the nanoplasmonic structures from a specific direction in the far-field region, we integrate a nanoscale emitter into a Yagi-Uda antenna and demonstrate strong directional control of thermal emission with a narrow-band spectrum at the nanoscale. By exploring the effects of the reflector and the director of a Yagi-Uda antenna, the emission enhancement factor up to 8.3 is achieved through geometry optimization.

Here, we apply the fluctuating surface current method to optimize the gold nanorod emitter at the wavelength of 7.25μm. The corresponding optimized geometry parameters are 40nm for width 40nm for thickness, and 2.5μm for length. In the following sections, we will use this design of the gold nanorod emitter as the feed of the Yagi-Uda antenna.

Consequently, its resistive loss is closely related to the material properties and cross-section sizes, and its radiative loss is determined by the length of the emitter. In fact, the fundamental mode of its QNMs behaves like dipole-radiation as shown in Fig. 2-1(a) for the spatial distribution and Fig. 2-1(b) for the spectral thermal emission.

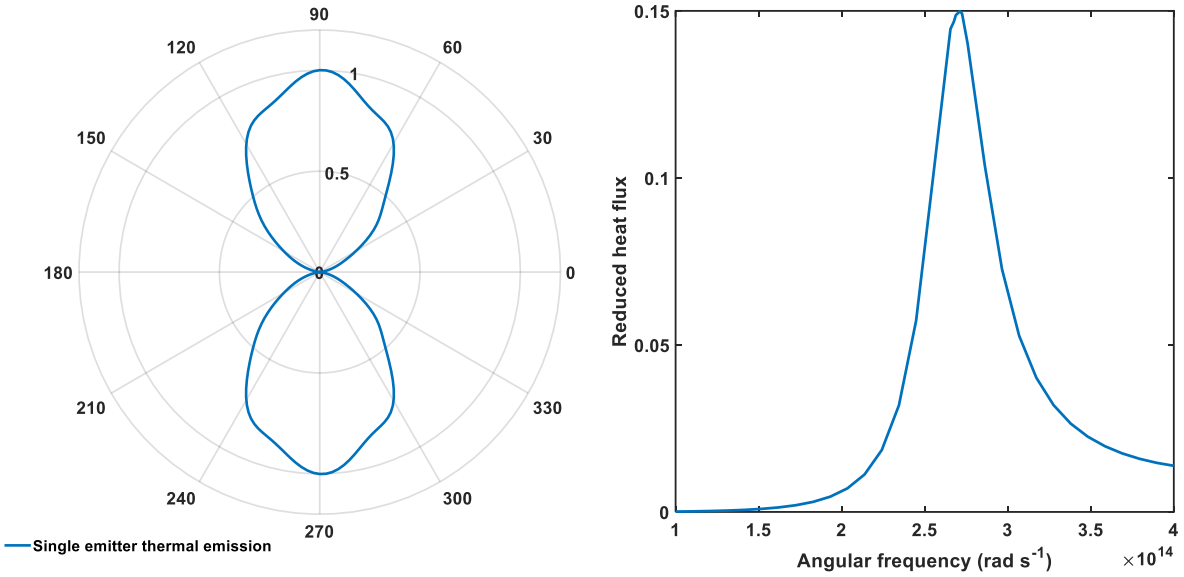

(a) (b)

Figure 2-1 (a) Spatial distribution of the far field thermal emission from a single gold nanorod emitter. The plotted physical quantity is the normalized $|E|^2$ with respect to the peak intensity. (b) Spectral thermal emission from the single gold nanorod emitter where the resonant wavelength is located around 7.25μm.

Based on the optimization of thermal emission from a single nanoscale emitter, we explore how to control the directionality of the nanowire arrays via numerical simulation. Later in this chapter, we present a broadband near-field thermal emitter/absorber based on metal wire arrays (MWAs) hyperbolic metamaterials, which can significantly enhance far-field radiative heat transfer with infrared surface-polariton-resonance materials and maintain the narrow-band spectrum.

In general, a Yagi-Uda antenna array consists of a reflector, a feed and multiple directors, as shown in Fig. 2-2.

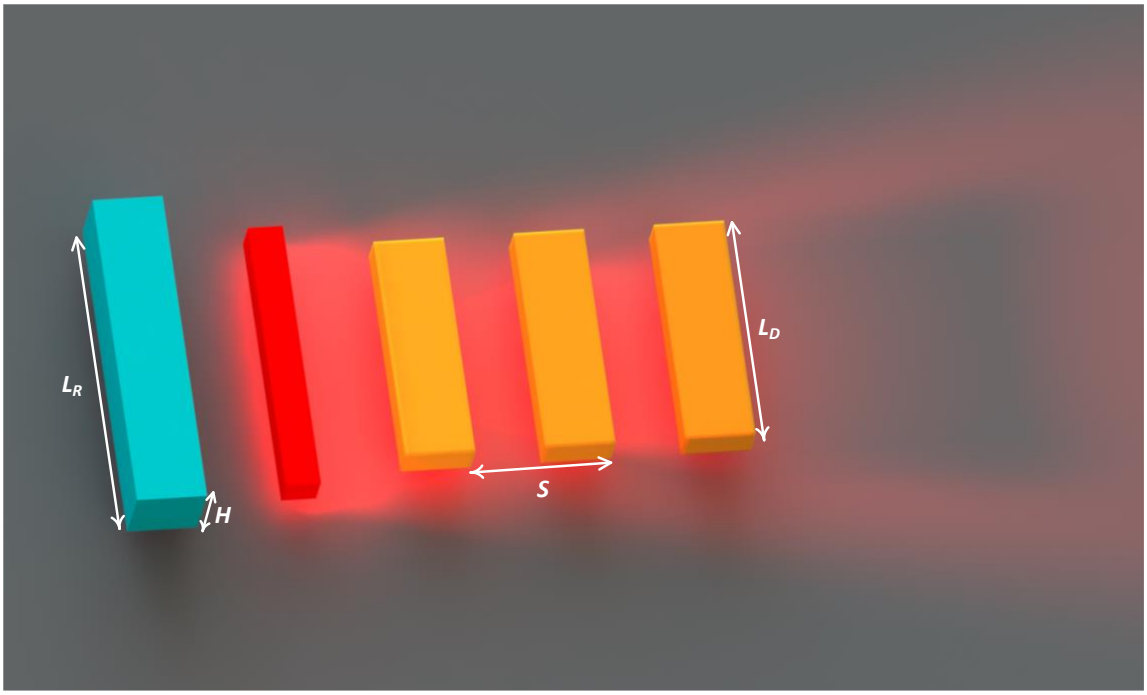

Figure 2-2 Schematic of a Yagi-Uda antenna with one feed, one reflector and three directors. LR, H, LD and S denote the length of the reflector, height of the director, length of director and spacing distance between directors, respectively.

The directionality of the Yagi-Uda antenna array mainly originates from the constructive interference of the propagating electromagnetic waves. The suppression of the backward propagation by the reflector also contributes to the directionality. Although thermal radiation is generally considered to be incoherent due to its stochastic feature, the introduction of the optimized QNM within a single thermal emitter could compensate the lack of coherence and facilitate the design of the whole Yagi-Uda antenna array. The surface plasmonic modes along the gold nanorod emitter increases the spatial coherence of its thermal emission. By optimizing the QNMs to make it spectrally narrow and sharp, the temporal coherence can be improved as well. Therefore, the concept of constructive interference of electromagnetic waves can still work properly in the thermal Yagi-Uda antenna. Yet, due to the randomness inherited in thermal radiation, the

directionality of the thermal Yagi-Uda antenna is expected to be weaker than that of the RF or the optical Yagi-Uda antenna. The challenges for designing a high-performance thermal Yagi-Uda antenna are two-fold. One is that the forward emission enhancement is weaker compared to optical antennas given its low coherence. The other is that the resulting contrast between the forward and the backward emission is small due to the weak suppression on the backward emission.

To quantitatively evaluate the performance of the directional control of a thermal Yagi-Uda antenna, we directly calculate the half-height emission angle φ and the forward and the backward emission enhancement factors I_F and I_B in terms of the thermal radiation intensity $|E_0|^2$ of the single emitter, namely $I_{F,B} = |E_{F,B}|^2 / |E_0|^2$.

Here, we address the impact of the directors and the reflectors on the thermal emission pattern of the Yagi-Uda antenna. By sweeping the geometry parameters of the antenna including director length, spacing distance, reflector length and height, we obtain the optimized Yagi-Uda antenna design at the interested wavelength.

2.2.1 Spacing of the directors

The distance between neighboring directors is the most crucial parameter in controlling the directionality of the Yagi-Uda antenna. As the enhancement of the forward emission lies in the constructive interference of propagating waves, the spacing between neighboring directors can significantly modify the forward emission by altering the relative phase of the adjacent directors. In the scenario of thermal radiation, the reflector and all the directors will simultaneously become secondary thermal sources once the feed emitter is thermally activated. As long as the spacing falls in the resonant wavelength of the feed which is 7.25μm in our case, the secondary thermal emission could interfere with each other either constructively or destructively. We choose the length of each

director to be 2.2μm and with the cross-section area of 40nm by 100nm. The reflector is 3μm long and separated from the feed by 1.8μm. The total number of the directors next to the feed is assumed to be 3μm. Fig. 2-3(a) plots the thermal emission pattern of the Yagi-Uda antenna for the spacing S in the range of 500nm to 6μm, whereas Fig. 2-3(b) represents the forward and the backward emission intensity enhancement factors. The forward emission intensity gradually increases with the increasing spacing and reaches the maximum when S is equal to 3μm, thus imposing strong constructive interference. The backward emission intensity shows a similar trend but experiences the suppression from the reflector due to the quarter-wavelength phase shift between the feed and itself. It is worth noting that the half-height emission angle φ does not vary much with the spacing. For all our calculations, the half-height emission angle maintains around 62° for the forward emission and 55° for the backward emission.

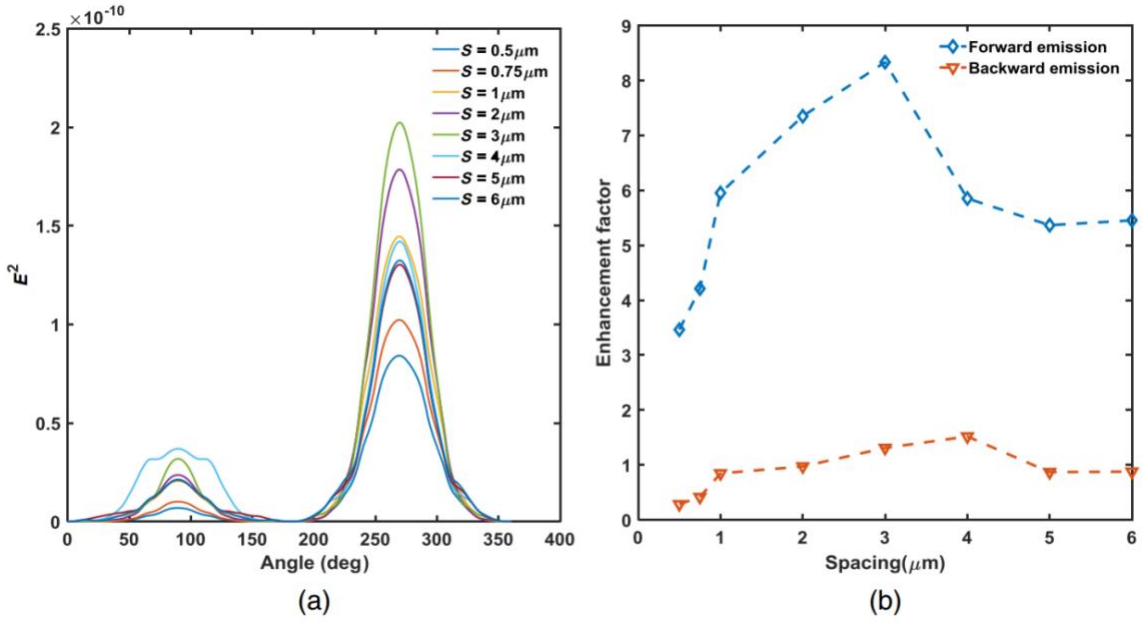

Figure 2-3 (a) Spatial distribution of the thermal emission projected to the XY plane at different director spacings. (b) Enhancement factors of the forward (270 deg) and the backward

(90 deg) emission. The calculation of the enhancement factors is based on the thermal radiation signal from the feed only.

2.2.2 Length of the directors

The length of the directors is another important factor for the directionality of the Yagi-Uda antenna. As described in the previous section, the directors could become secondary thermal sources and contribute to the final emission pattern. The length of the directors turns out to be the dominant parameter in determining the resonant wavelength. It seems that the ideal case in terms of the forward emission intensity should be that the length of the directors is the same with the feed's length. However, in choosing the same length for both the directors and the feed, the backward emission could also be boosted. So, it is necessary to avoid such resonance between the feed and the directors. Here, we calculate the thermal emission of the Yagi-Uda antenna with different lengths of the directors. The parameter of the reflector is the same as that described in the previous section. The total number of the directors is still 3 and the spacing is now fixed to be 3μm. The corresponding thermal emission pattern and emission intensity enhancement factors are plotted in Fig. 2-4. From Fig. 2-4(b), we can see that the forward emission indeed reaches the strongest point at the length of 2.5μm. But the backward emission intensity also becomes the highest. The ratio of the forward and backward emission intensity at the length of 2.5μm in this case is obviously worse than other cases. It should also be pointed out that the backward emission becomes dominant when the length of the directors is larger than 2.5μm, as shown in Fig. 2-4(a). In conclusion, the optimal length of the director should be slightly smaller than the feed's length, which is 2.2μm in this case.

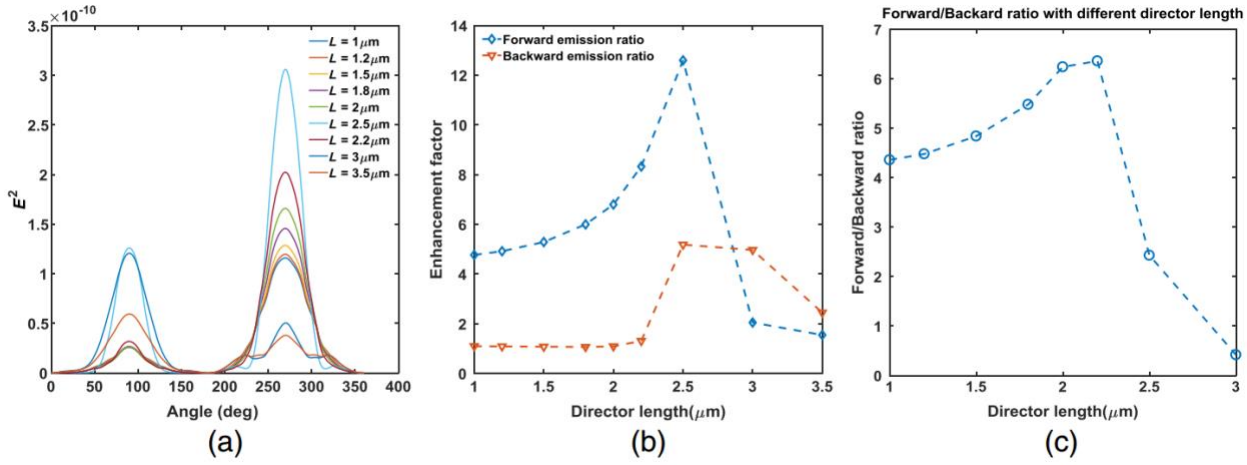

Figure 2-4 (a) Spatial distribution of the thermal emission projected to the XY plane with different director lengths. (b) Enhancement factors of the forward (270 deg) and the backward (90 deg) emission. The calculation of the enhancement factors is based on the thermal radiation signal from the feed only. (c) Forward/backward ratio under different director lengths.

2.2.3 Influence of the reflector

The role of the reflector in the Yagi-Uda antenna is to suppress the backward emission. To realize suppression, the reflector should be placed at a distance of approximately one-fourth resonant wavelength from the feed. The π phase shift generated by the quarter-wavelength gap therefore could effectively destruct the backward emission. On the other hand, the length of the reflector should be larger than that of the feed in order to block the direct thermal radiation coming from the feed. The length of the reflector turns out to be an important parameter in optimizing the antenna directionality. Here, we calculate the thermal emission pattern and emission intensity with different reflector lengths. As shown in Fig. 2-5(b), the antenna gives the best performance when the reflector length is 3μm. which is slightly larger than that of the feed. As the reflector length becomes larger, it further suppresses the backward emission below the emission of the single

emitter. When the reflector length is smaller than the feed length, the antenna begins to enhance both the forward and the backward emission and lose the directionality. The decrease of the forward emission when increasing the reflector length is due to the shift of the resonant wavelength from the reflector. Therefore, the reflector length should be chosen to be slightly larger than the feed length.

There exist some other parameters affecting the design of the Yagi-Uda antenna, such as the total number of the directors and the height of the reflector. In Fig. 2-6, we show that these two parameters play a minor role on the performance of the antenna. For the number of the directors, even one director is sufficient to enable the directionality because the director nearest to the feed is the one most strongly activated, as shown in Fig. 2-6 (a). For the height of the reflector, given that the spatial distribution of thermal emission is more oriented in the longitudinal direction, its influence on the directionality is negligible.

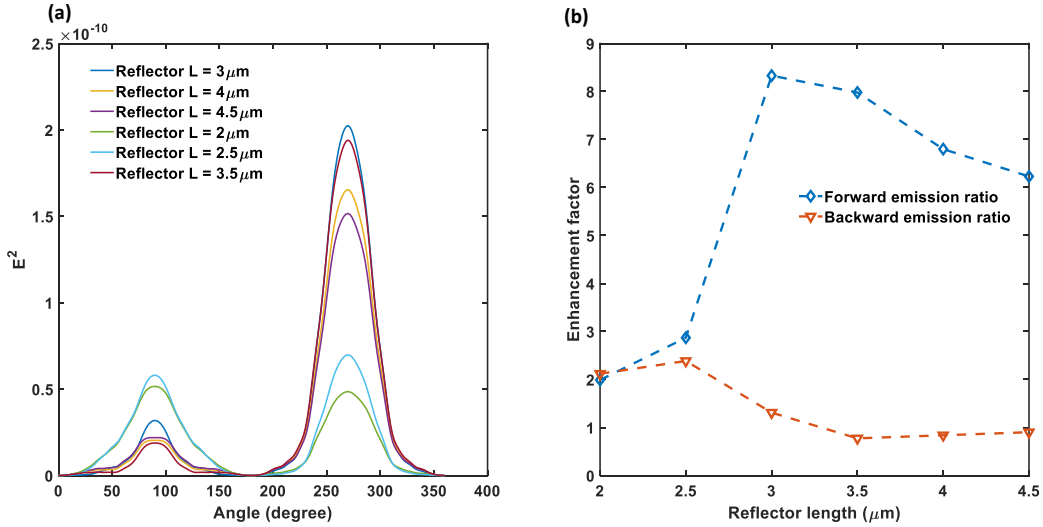

Figure 2-5 (a) Spatial distribution of the thermal emission projected to the XY plane with different reflector lengths. (b) Enhancement factor of the forward (270°) and the backward emission (90°). The calculation of the enhancement factor is based on the thermal radiation signal from the feed only.

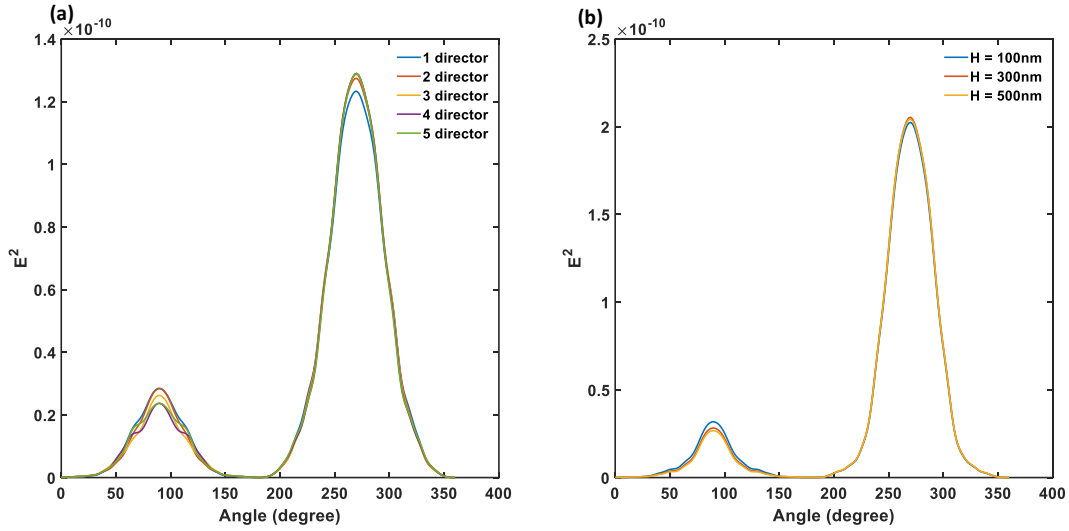

Figure 2-6 (a) Spatial distribution of the thermal emission projected to the XY plane with different numbers of directors. (b) Spatial distribution of the thermal emission projected to the XY plane with different reflector heights.

Finally, we can plot the spatial distribution of the thermal emission from the optimized Yagi–Uda antenna in comparison with the single nanorod emitter in Fig. 2-7, where an enhancement factor of the forward emission up to 8.3 is achieved.

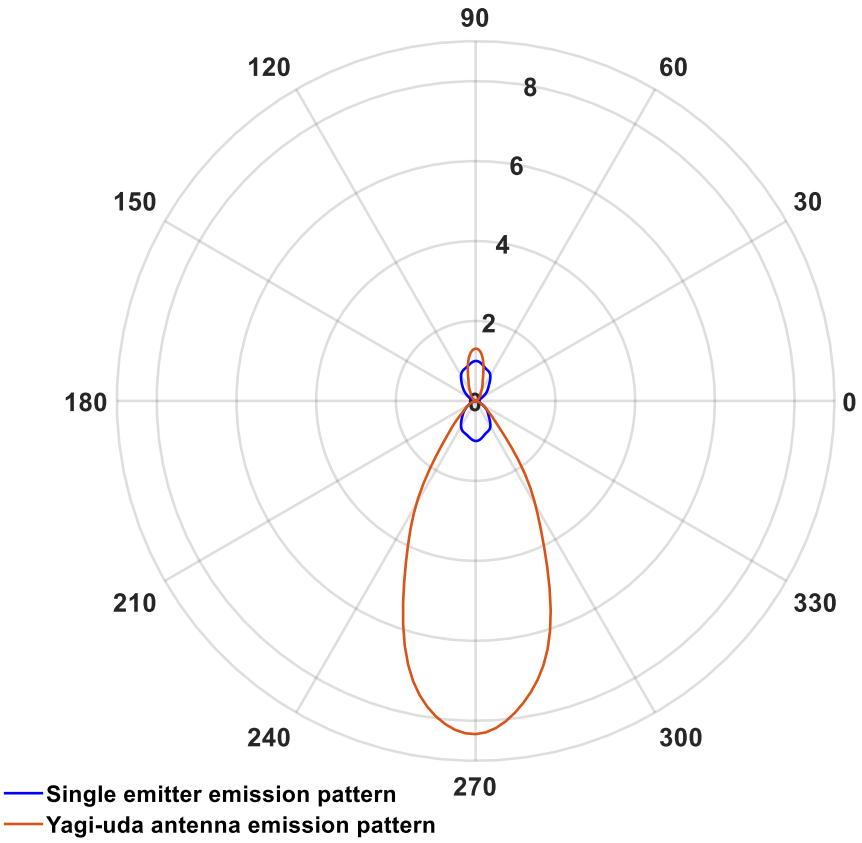

Figure 2-7 Spatial distribution of thermal emission from a single gold nanorod emitter and the Yagi-Uda antenna.

2.2.4 Conclusion

In conclusion, the optimal design of the thermal Yagi-Uda antenna varies with the wavelength of interest. For a given resonant wavelength, the spacing between the directors should be around half of the wavelength. The director length should be slightly smaller than the feed length, whereas the reflector length should be slightly larger than the feed length. For the optimized Yagi-Uda antenna in this work, an enhancement factor of the forward emission up to 8.3 is achieved. Hence, nanoscale Yagi-Uda antenna arrays would be a promising platform for controlling the directionality of thermal infrared sources.

2.3 Perfect and tunable nanoplasmonic thermal emitters in the far-field regime

2.3.1 Fabrication process

Because the thermal emission from each resonator usually emits in all directions, the substrate is chosen to be a metal plate with a dielectric spacer (as illustrated in Fig. 2-8(a)), where the metal plate performs as a mirror to reflect all the radiation to the upper space. The sample fabrication begins with the sputtering of a 50nm thick aluminum thin film as the metal ground plate on a SiO_2 thermal oxide wafer. Then a 150nm thick aluminum oxide layer is sputtered on top of the aluminum, which serves as the dielectric spacer.

We demonstrate that perfect thermal emission of the resonator arrays can always be approached by tuning the thickness H of the metal wires [65-67]. To prove the concept, all of the transmission line resonators in our experiment are aligned in the y-direction, indicating the maximized emissivity at the y-polarization. The gold nanorod arrays are fabricated by standard electron beam lithography techniques and a subsequent lift-off process. The scanning electron microscope (SEM) image of transmission line resonators is shown in Fig. 2-8 (b). The detailed process will be described in later chapter.

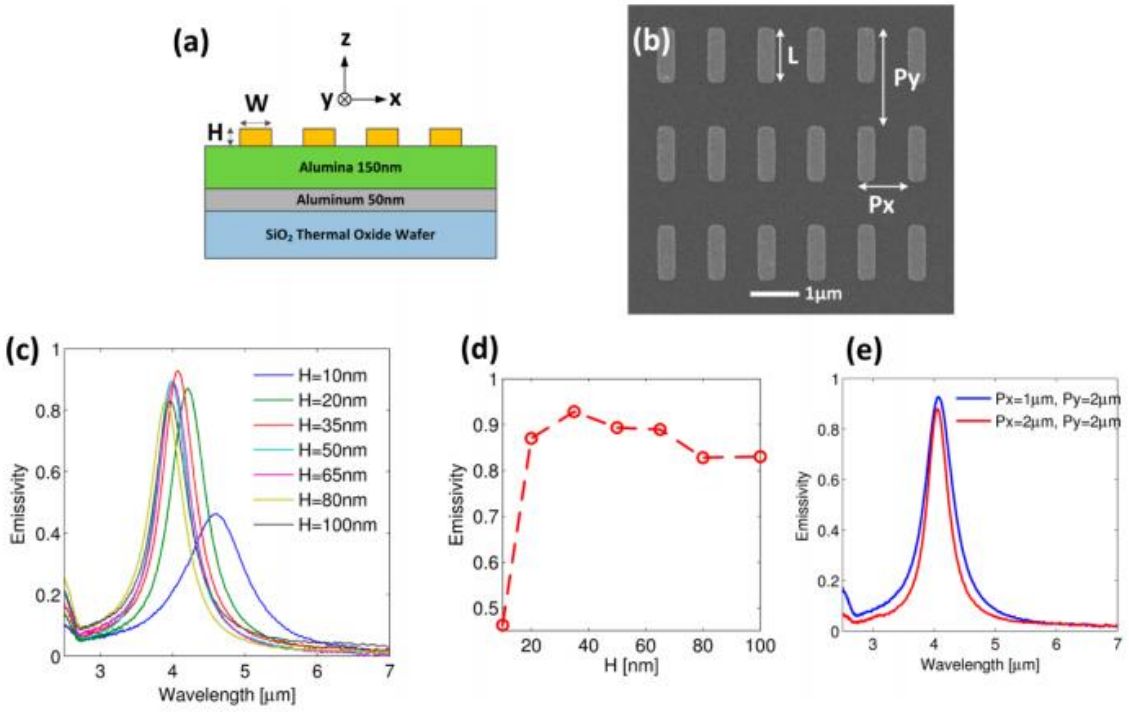

Figure 2-8 Emissivity of straight transmission line resonator arrays. (a) Schematic of the cross section of the transmission line resonator arrays. (b) SEM image of the top view of the transmission line resonator arrays. (c) Experimentally measured y-polarized emissivity spectra of the arrays with different H and (d) their corresponding peak values. The Q factor for the case with H=35nm equals 7.3. (e) Experimentally measured y-polarized emissivity spectra of the resonator arrays for H=35nm with different periodicities.

2.3.2 Fourier Transform Infrared Spectroscopy (FTIR) and Optical characterization

Our measurement system starts from FTIR, which is mostly applied for the broadband thermal radiation measurement, because radiation of all wavelengths is collected simultaneously without a silt blocking as of a dispersive spectrometer [68-70]. The resulting higher throughput, known as Jacquinot advantage, can increase up to 10 times SNR. The principle of FTIR is based on interference where radiation is first measured as a function of optical path difference (OPD)

and then mapped on a spectrum via Fourier transform. where $S(\delta)$ is detected signal and $B(\tilde{\nu})$ is the source signal. $\tilde{\nu} = 10^4/\lambda$ where $\tilde{\nu}$ is the signal wavenumber and λ is the signal wavelength. δ is OPD and equals two timesthe mirror distance difference for a Michelson interferometer. FTIR is based on the Fourier transformation for the wavelength separation in spectral measurement.

In common measurements, there is no difference between rapid-scan and step-scan. However, when demodulation techniques are included in signal-to-noise (SNR) improvement, step-scan is required. This is because the wavelength separation mechanism of FTIR with a moving mirror itself is a modulation, which cannot be distinguished from the external modulations (e.g., the input amplitude modulation electrically or by a chopper).

The thermal emissivity spectra of the samples are characterized in the wavelength range of 2-12μm. The emissivity is evaluated as the absorptivity according to Kirchhoff's law. This law is fully applicable in our experiment because the size of the arrays is much larger than the characteristic wavelength of thermal radiation. Because our samples are opaque, we directly measure their reflectivity. The emissivity can then be calculated by one minus the reflectivity.

To obtain the reflectivity, the y-polarized reflectivity spectra of the samples are measured by a Fourier-transform infrared (FTIR) spectrometer combined with an infrared microscope. An infrared linear polarizer is used in the infrared microscope, which only allows the y-polarized reflected light to pass through. The reflection spectra of the samples are normalized to that of a gold standard mirror. The reflectivity of the samples is measured by using a FTIR spectrometer (Bruker IFS 66/s) combined with an infrared microscope (Bruker Hyperion 3000, with liquid nitrogen cooled MCT detector, KBr beam splitter, 15×Cassegrain objective lens with a numerical aperture of 0.4, and a 40μm × 40μm focusing spot size).

2.4 Far-field thermal emission from single nanoplasmonic emitter

2.4.1 Overview

In terms of the applications of thermal emission, including infrared energy harvesting, radiative cooling, and thermal camouflage, the need for accurate and precise measurement of thermal emission is essential. In order to increase the sensitivity and portability of the device, a single working device is studied in this chapter. Since the signal from a single emitter is much smaller, so overcoming the noise from the background and instrument itself is key to the experiment.

Accurate thermal emission measurement is then fundamental in material characterization and increasingly demanding in modern densely packed microdevices. More importantly, the rapid development of engineered thermal emission, including efficient light sources, passive radiative cooling, and radiative energy harvesting, makes the measurement system and analysis crucial. Conventional thermal radiation measurement is performed via reflection and transmission. The subsequent application of Kirchhoff's law determines the emissivity from the net absorption of the sample. However, this indirect method requires the emission in thermal equilibrium and reciprocal. Otherwise, Kirchhoff's law is violated, and the equality of emissivity and absorptivity is no longer valid. Furthermore, this approach also becomes impractical once samples are highly absorptive or scattered because of the difficulties in refining reflective and transmissive spectra. Unfortunately, non-equilibrium, non-reciprocal, and extreme reflective or absorptive microdevices are ubiquitous in state-of-art thermal radiation engineering. Directly measuring the thermal radiation is, therefore, imperative.

However, direct thermal emission measurement can be challenging because of the ambient thermal background noise, which is especially true for microdevices whose thermal signal is weak. In this chapter, we have successfully measured the spectra of a microbar emitter with systematic signal enhancement and noise reduction. Lock-in amplifier (LIA) and FTIR serve as primary components in signal-to-noise ratio (SNR) improvement [71-77]. Their signal process is simulated and consistent with our experimental results. Besides, our system includes microscope and cryostat subsystems that can precisely localize a single working device and obtain its radiation solely under different temperatures. The system design and analysis can then provide general guidelines to set up a thermal, near-infrared, mid-infrared radiation measurement platform. The chapter will discuss the infrared thermal spectrum measurement based on FTIR with a focus on the demodulation or phase-sensitive detection technique for noise reduction [78-83].

2.4.2 Measurement system set up

The overall experimental setup is shown in Figure 1. The optical signal from the device is modulated, detected (transduced) by FTIR, and finally demodulated by a lock-in amplifier, which is a bandwidth filter automatically centered at the modulation frequency. In addition, the signal-to-noise (SNR) is further improved with a microscope extracting the optical signal from devices at the micro and nanoscale.

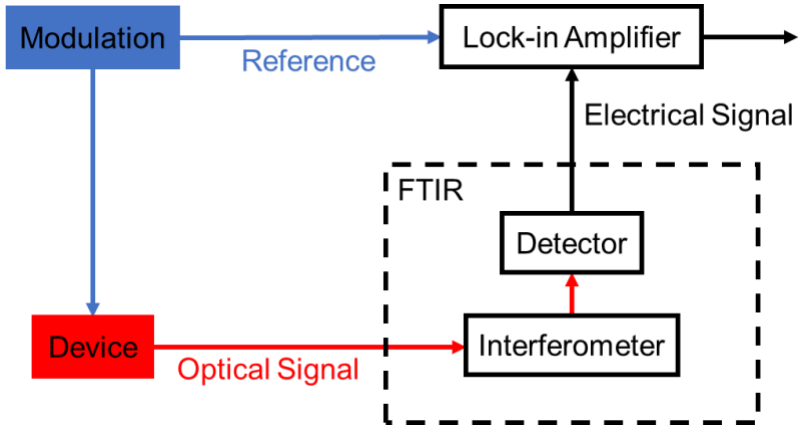

Figure 2-9 Experimental setup for infrared thermal emission spectrum measurement.

Fundamentally, noise reduction is the signal averaging in the time domain, or equivalently, the bandwidth filtering in the frequency domain based on the incoherence nature of noises. However, different sources of noise have different frequency dependencies as shown in Fig. 2-10. For our measurement setup, there are typically five kinds of noises. 1/f, thermal, and shot noises are inherent in electrical measurement (detection) systems, which includes the input noise of the lock-in amplifier, i.e., the lock-in amplifier's own noise. Thermal and shot noises are white noises that are more or less uniform over a wide range of frequencies. I/f noise is also broadband but increases with decreasing frequency.

Externally, there is also interference (peak) noises at some definite frequencies, such as $50/60\text{Hz}$ power lines. Since our measurement is initially at DC, their influence is small but is needed for consideration when choosing the modulation frequency. The main issues for infrared thermal spectrum measurement are the uncontrollable room-temperature (RT) blackbody radiation from surrounding objects at mid-infrared (centered at about 1000cm^{-1}) and stray-light background at near-infrared, both of which are at DC.

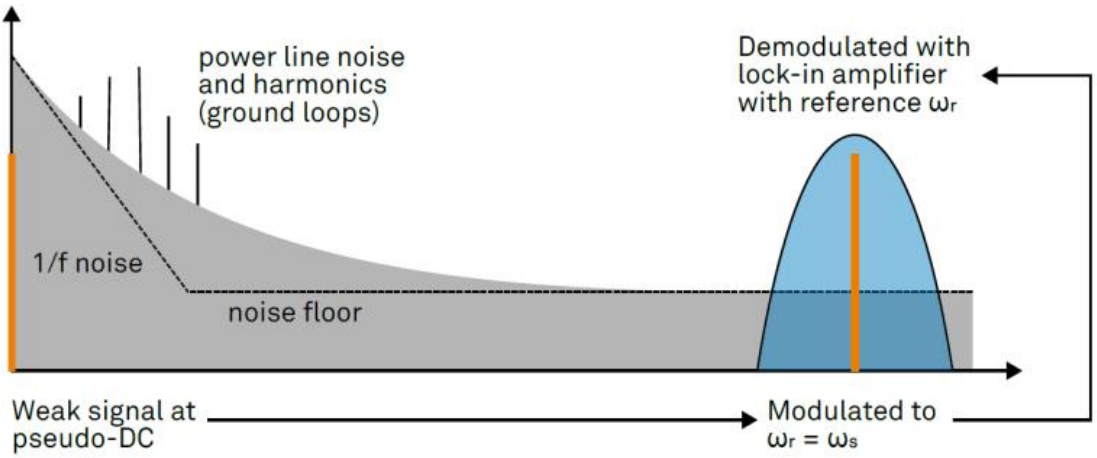

Figure 2-10 Frequency dependencies of different noises. Demodulation noise reduction is an effective bandpass filter centered at the modulation frequency.

Conventional noise reduction, including the average of the scans or lower the scan speed, is then inadequate because the weak signal at DC is buried in the strong RT thermal background noise and the 1/f noise around DC. However, the demodulation technique switches this bandwidth filtering process to a controlled frequency. Ideally, only a small amount of white noise will remain, and the higher the modulation frequency (the further away from DC), the higher the SNR.

For the optical signal capturing system, one of the advantages of our measurement design is that we have included a microscopy subsystem which precisely locates the single working micro device on chip. As shown in Fig. 2-11(a), the device under test (DUT) is illuminated by a while light source, and after a well-focused objective, the DUT reflection is then collected by a charge-coupled device (CCD) camera forming a microscopic image. With the help of the translation stages where DUT is fixed on, we can move the device that we are interested in precisely at the center of optical axis. This is helpful for testing modern micro devices, which are for the most part densely fabricated on a single wafer. Moreover, the DUT can be in a cryostat with temperature control.

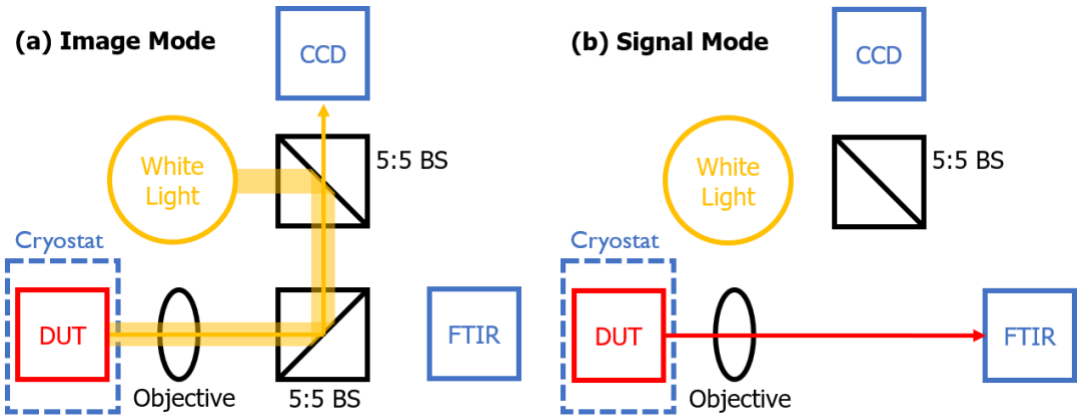

Figure 2-11 Microscopy subsystem in thermal radiation measurement design. (a) Image mode: forming an image of the microscopic device. Find and locate the target micro device. (b) Signal mode: measuring the device signal. Beam splitter is removed to increase the signal strength.

During the image mode, the DUT is in off-state, and we can use a linear translation stage for the objective focus. For the objective with larger magnitude for smaller devices, a motorized translation stage can be used because of the smaller depth of focus. After finishing the image mode, we can transfer to the signal mode, as shown in Fig. 2-11(b), and remove the beam splitter. Since the reflective microscope objective has already been well-focused, after turning on the DUT, we can have our emitting source radiation well-collimated and entering the FTIR. The removal of beam splitter is again intended to increase the signal strength. These operations are further summarized in our discussion about SNR improvement in next section.

2.4.3 SNR Improvement

Our thermal measurement setup can be generalized into a cascade system combing the DUT and the measurement system, as shown in Fig. 2-12. Our target is the response (input-output relation) of DUT. However, the result we can obtain is practically the response of the whole

cascade system, and a careful calibration and noise reduction are needed for accurate and precise device characterization.

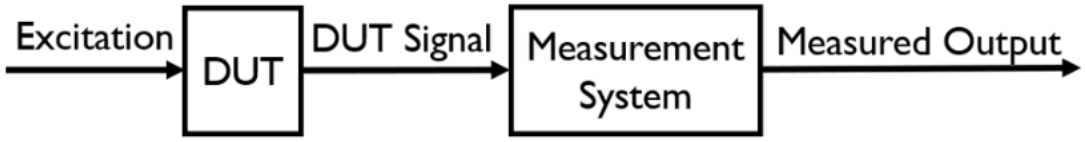

Figure 2-12 Schematic of the thermal measurement system.

To discuss the noise reduction strategies in our thermal measurement system, we need a radiometry modeling of the signal mode in Fig. 2-11(b). For a well-setup measurement system, as shown in Fig. 2-13, the angle dependence (θ, ϕ) and part of the temperature dependence T on radiance L are fixed.

1. $m(\lambda)$: the measurement system (FTIR+MCT) is in constant room temperature environment, and its response function is only depended on the signal wavelength.

2. $I_{DUT}(\lambda, T_{DUT})$: the radiance from DUT L_{DUT} is passing through a fixed number of lenses or apertures whose total angle dependence (θ, ϕ) is known. Then we can have the radiant intensity $I(\lambda, T_{DUT})$ whose temperature T_{DUT} is controlled by a current source.

3. $I_{error}(\lambda, T_{crystat}) = I_{error,DUT}(\lambda, T_{cryostat}) + I_{error,BG}(\lambda)$: the error radiance, also with fixed angle dependence, becomes the error intensity, which is further separated into two parts: one is from DUT whose temperature is controlled by a cryostat, the other is from measurement system which is in constant room temperature.

To summarize the radiometry model, we present the radiation transport Eq. (2.1) on which the model is based. We then split our noise reduction strategies into three levels in the following subsections.

$$I_{measured}(\lambda,T) = m(\lambda)\left[I_{DUT}(\lambda,T_{DUT}) + I_{error,DUT}\left(\lambda,T_{cyrstat}\right) + I_{error,BG}(\lambda)\right] \quad (2.1)$$

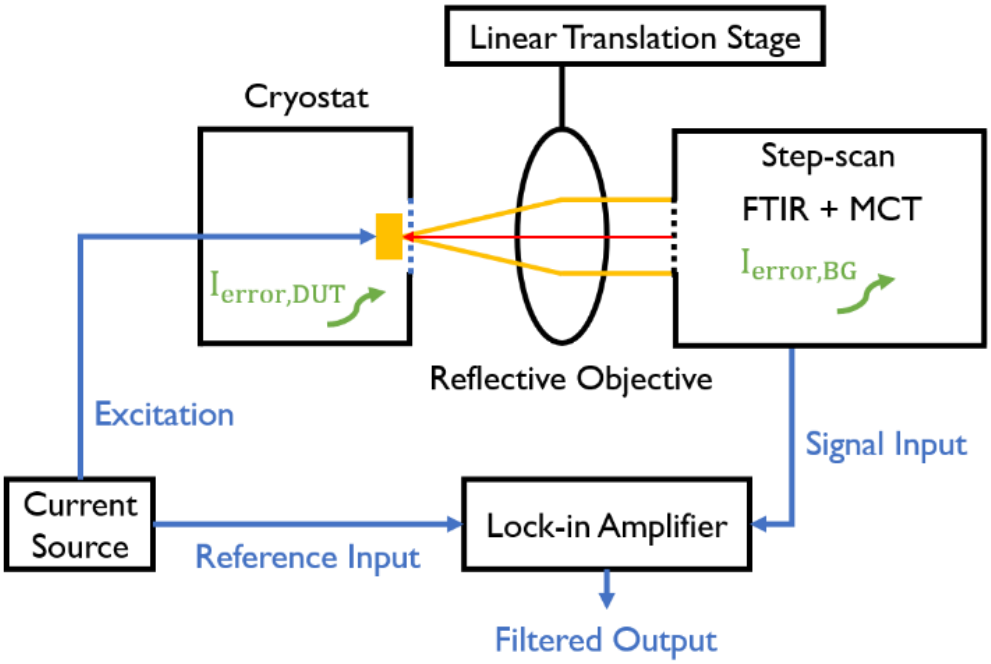

Figure 2-13 Signal mode including noise reduction strategies. Reflective objective and its accurate focus by a linear translation stage for signal enhancement. DUT noise $I_{error,DUT}$ is reduced by low temperature controlled by a Cryostat. Background noise $I_{error,BG}$ is filtered by a lock-in amplifier.

2.4.4 Signal enhancement for I_{DUT}

The most straightforward method to increase the signal-to-noise ratio in our measurement is to increase the signal intensity, which has already been partially discussed in the previous section including: First, the temperature of DUT is well controlled by a current source, and can be high for large thermal emission. Second, Jacquinot advantage of FTIR for higher sensitivity to weak signal is utilized. Third, reflective microscope objective with high reflectance is used and its motorized translation is well controlled for precise focus. Lastly, I aligned the DUT, reflective microscope objective, and FTIR entrance with an internal guiding red laser of FTIR.

2.4.5 Noise reduction for I_{error}

To reduce the noise I_{error} in our measurement, we have different strategies for $I_{error,DUT}$ and $I_{error,BG}$. Since $I_{error,DUT}$ is temperature dependent, the most effective way is to reduce the temperature around DUT via a cryostat. In our measurement, we have used JANIS ST-500 Cryostat with liquid nitrogen reducing the temperature down to 80K. The reduction of $I_{error,BG}$ is achieved by the mechanism of phase-sensitive detection (PSD), which applies a lock-in amplifier and FTIR step-scan mode to achieve a dynamic narrow filter to remove most of the background noise and pick up the signal.

2.4.6 System response calibration for $m(\lambda)$

The final part of our radiation transport equation analysis is the response function of measurement system (Eq. (2.2)), which is calibrated by a standard thermal emitter (with known outputs) measured under two different temperatures $T_{DUT} = T_1$ and T_2,

$$m(\lambda) = \frac{I_{measured}(\lambda,T_1) - I_{measured}(\lambda,T_1)}{I_{DUT}(\lambda,T_1) - I_{DUT}(\lambda,T_2)} \tag{2.2}$$

Note $I_{error,\ DUT}$ is independent of temperature after fixing the cryostat temperature $T_{cryostat}$, and becomes small when $T_{cryostat}$ is low. $I_{error,\ BG}$, as discussion above, has been well filtered by the lock-in amplifier. Therefore, I_{error} is not included in our response function calibration.

2.4.7 Lock-in amplifier

The lock-in amplifier is the central component in the demodulation noise reduction and mainly consists of three components: mixer, low-pass filter, and amplifier. For the purpose of noise reduction, we can focus on the mixer and low-pass filter first, as shown in Fig. 2-14. The signal is first modulated at frequency f_s, which is equal to the reference frequency $f_r = f_s$. The signal

processing of the mixer is easier to analyze in the time domain, and is the product of signal and reference sine wave $V_s(t) \cdot V_r(t)$, resulting in a difference-frequency $f_s - f_r = 0$ (DC) component and a sum-frequency $f_s + f_r = 2f_r$ component. The mixed-signal then passes through the low-pass filter, which is easier to analyze in the frequency domain, and the sum(high)-frequency $2f_r$ component is filtered out. Another way to consider the low-pass filter is an averager in the time domain, where the high-frequency component is then averaged to zero.

Implicitly, the noise at DC along with the signal is also mixed with the reference, resulting in $-f_r$ (difference) and f_r (sum) frequency components. This further requires the cutoff frequency of the low-pass filter lower than f_r to exclude all $\pm f_r$ and $2f_r$ components. Besides, the narrower bandwidth is, the more broadband noise can be reduced. Practical lock-in amplifiers use dual-phase demodulation to finish the coordinate transformation, i.e., we can obtain the demodulated output in Cartesian coordinate $X + iY$, or polar coordinate (A_s, θ) with the amplitude A_s and phase θ.

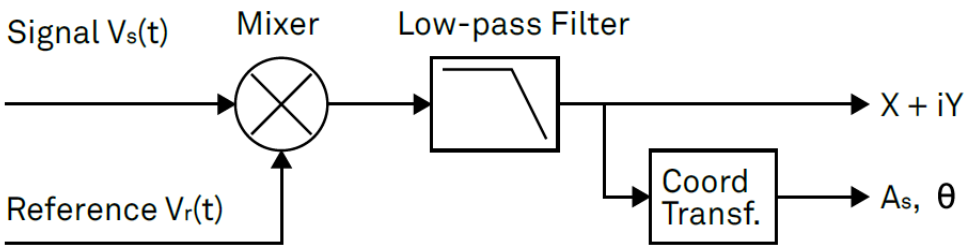

Figure 2-14 Mixing and low-pass filtering performed by the lock-in amplifier.

Note the signal is not necessary to be a sine wave even though the excitation (source) is typically a sine wave. We can finally analyze the sine harmonics for any possible waveform of the signal. For our measurement of a thermal device (heater) with a sine wave (f_r) current excitation, its emission, following the Joule heating I^2R , is a rectified sine wave whose 1st harmonic is $2f_r$.

Similarly, the reference is not necessary to be a sine wave, although our lock-in amplifiers use a sine wave for demodulation. Using a square wave as the reference can sometimes be beneficial and obtain a larger amplitude of demodulated output compared to using a sine wave. But when higher-order harmonics are considered, a square reference wave can only demodulate odd harmonics. For example, in our thermal device measurement, we need deliberately to choose the 2nd harmonic at $2f_r$.

2.4.8 Setting optimization

The formal end of our measurement system, as shown in Fig. 2-10, is the setting optimization since some of the setting parameters of each component may have certain trade-off effects. The optimization process depends on the specific DUT we are measuring. In the next section, we would use an Au micro bar emitter as a typical example to show the whole process.

(1) Time constant and filter order

The low-pass filter has two setting parameters: one is the cutoff frequency (bandwidth), where TC is the time constant; the other is the filter order *n*, which is the number of low-passfilters in series. The performances of different cutoff frequencies and different filter orders, in both time and the frequency domains, are summarized in Fig. 2-15. Specifically, from frequency response, we start from the cutoff frequency f_{co} (Eq. (2.3)) which is set to lower than f_r and then adjust the filter order *n* to avoid the leakage of DC and harmonics, which is particularly important for low demodulation frequencies when $\pm f_r$ is close to DC ($f_s - f_r$). The filter with higher-order approaches more to be an ideal rectangular wave and suppresses more of these leakage noises.

$$f_{co} \propto \frac{1}{2\pi\, TC} \tag{2.3}$$

From step response, we can also find the response time becomes longer when the cutoff frequency decreases or the filter order increases. This response delay can be an issue when the lock-in amplifier is used in some feedback control when system response speed is in concern. Even for steady-state measurements, an extremely long response time can challenge the system's stability and reliability. The guideline is, first, the cutoff frequency should be broad enough to cover all signal components and be narrow enough to exclude noise at f_r. Second, the filter order should be as low as possible and suppress all leakage noises.

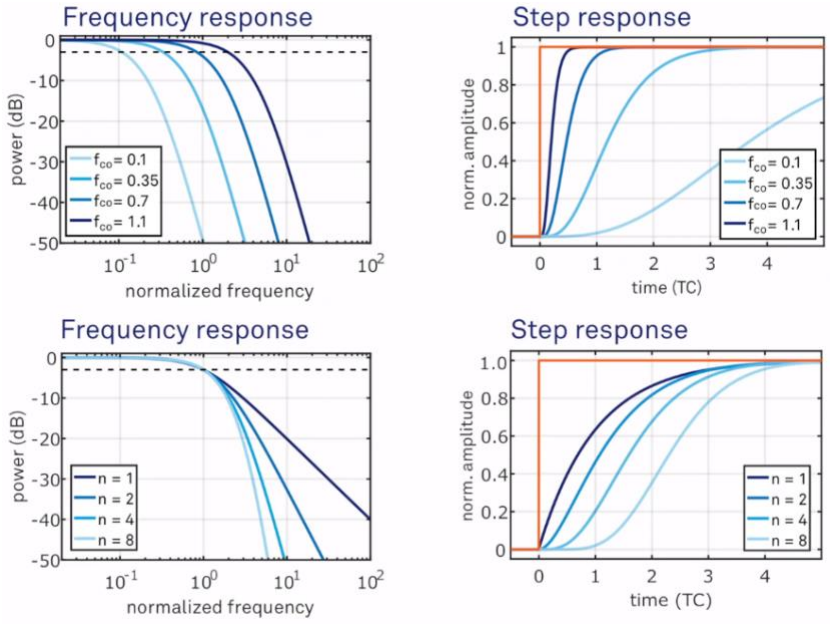

Figure 2-15 Frequency response and step response of different cutoff frequencies and filter orders.

In addition, when the demodulation frequency is extremely low and the mixed-DC ($f_s - f_r$) component is too close to the unwanted f_r and $2f_r$ terms, the setting of the low-pass filter becomes difficult, and an extremely large time constant is needed. The f_r and $2f_r$ components typically will leak out and affect the measured results. Sinc filtering allows for strong attenuation of the f_r and $2f_r$ components. Technically, the sinc filter is a comb filter with notches at integer

multiples of the demodulation frequencies (f_r, $2f_r$, $3f_r$, etc.) as shown in Fig. 2-16. Since the sinc filter takes out only the multiples of the demodulation frequency, the low-pass filter is still needed to reduce the broadband noises.

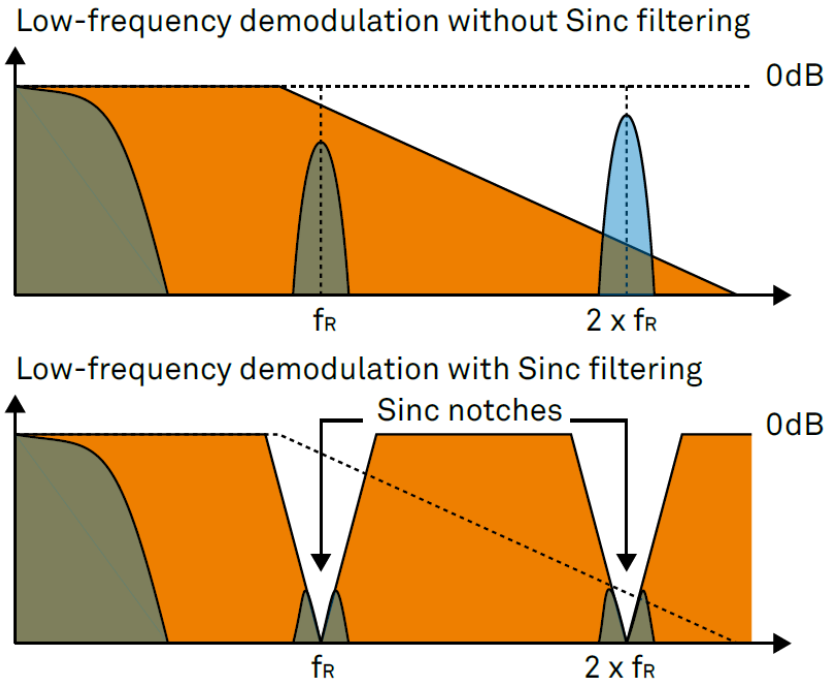

Figure 2-16 Effect of sinc filtering.

(2) Sensitivity and dynamic reserve

The final component of a lock-in amplifier is the amplifier, which determines the sensitivity, which is the total gain as the sum of the AC gain of the input amplifier before the mixer and the DC gain of the output amplifier after the low-pass filter. Modern lock-in amplifiers typically fix the AC gain to achieve a maximum dynamic reserve, which by definition is the ratio of the largest tolerable noise signal to the full-scale signal. For example, if the full scale is $1\mu V$ from the lock-in amplifier, then a dynamic reserve of $120dB$ means noise as large as $1V$ ($120dB$ greater than full scale) can be tolerated at the input without overload, as shown in Fig. 2-17. The

dynamic reserve thus represents the capability of an instrument to reject unwanted signal components while still providing accurate results.

The sensitivity is thus by definition the total gain but mainly controlled by the DC gain of the output amplifier (AC gain still contributes to the total gain, but we cannot use AC gain to control the sensitivity), and is always set to high but unsaturated (non-overload). The dynamic reserve is then the allocation between the AC and DC gains. Although the AC gain of the input amplifier enlarges signal and noise together, the noise can be finally filtered out via the following low-pass filter, leaving an enlarged pure signal. A higher AC gain therefore generally results in a higher dynamic reserve.

Note most modern lock-in amplifiers are digital with a digital-to-analog converter (ADC). Analog amplifier enlarges the signal and its noise together, and itself brings some additional noises, while digital amplifier (regenerator) enlarges signal and the original noise but does not add more noises, i.e., the digital amplifier only performs a numerical multiplication of the demodulated output with the scaling factor.

Note the definition of sensitivity does not take account into the SNR. Even though the noise is also enlarged by the DC gain and the result still has the same SNR, a larger DC gain helps to detect a weaker input resulting in a higher sensitivity. Finally, the output amplifier is followed by a digital-to-analog converter (DAC) with a fixed range of $10V$, which is a limitation for the enlargement scaling factor.

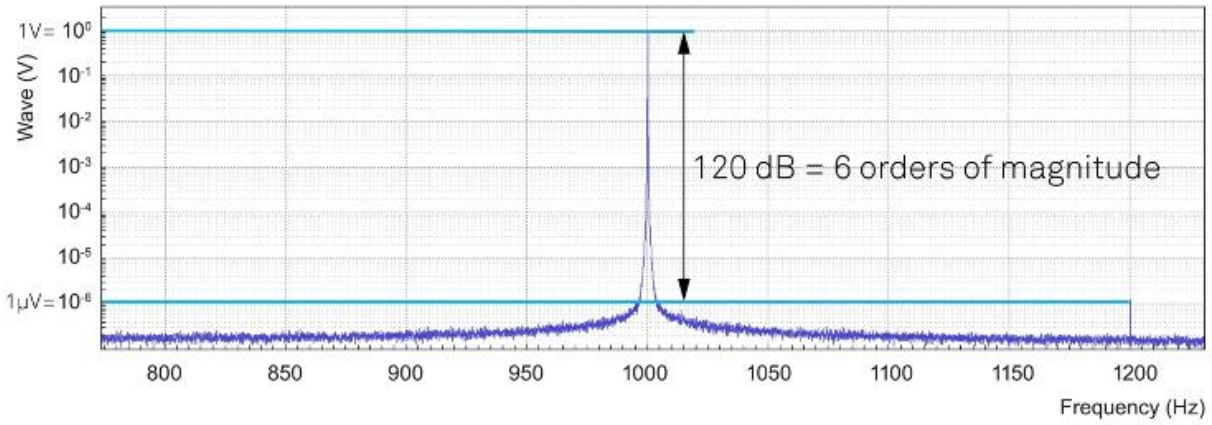

Figure 2-17 With a dynamic reserve of $120dB$, we are able to detect the $1\mu V$ broadband signal even with an interference (peak) noise of $1V$.

The dynamic reserve is generally fixed for a specific lock-in amplifier. Several guidelines then should be followed to fully utilize the dynamic reserve.

1. Select an appropriate input range: large enough to avoid clipping signal, and small enough to exploit the full dynamic reserve. Note since lock-in amplifiers do not proactively change the input range, we need to select the range considering the evolution of the signal throughout the entire measurement. For example, we need to consider our spectrum measurement at each mirror step (if step-scan modulation).

2. Remove the DC offset by setting the input to AC coupling. A large DC component at the input can use up most of the dynamic reserve resulting in reduced measurement performance.

3. Only removing the DC offset is not enough. The dynamic reserve will cost a lot to distinguish the non-signal interference (peak) noises, which will also contaminate the spectrum after mixing and make it difficult to set low-pass filtering. Either employ an appropriate external band-pass filter centered on the signal of interest and suppress the

parasitic components or generate a signal identical in frequency and amplitude to the spurious components and feed it into the differential input of the lock-in amplifier, as shown in Fig. 2-18.

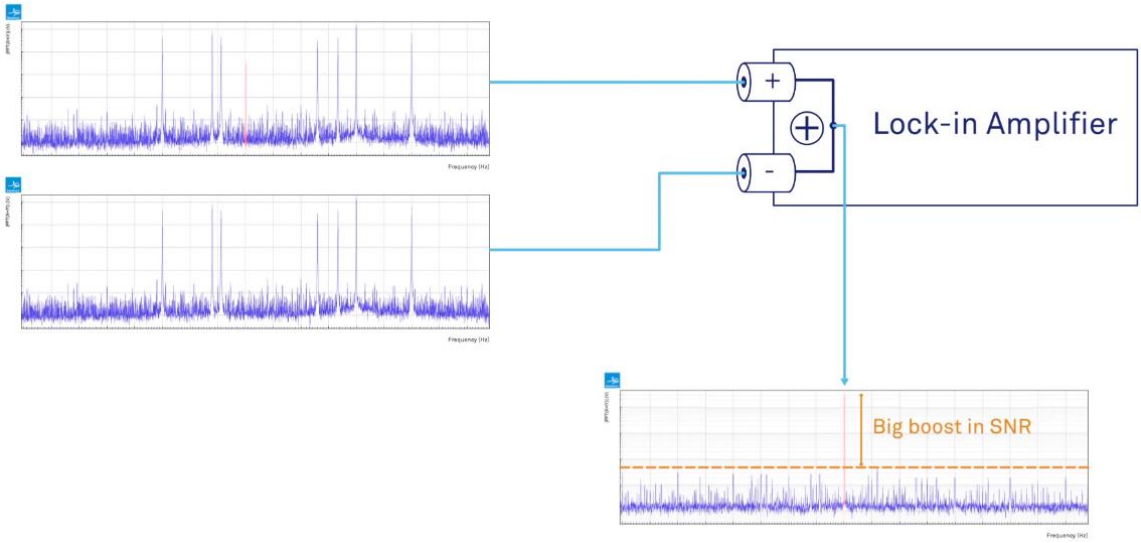

Figure 2-18 Use A-B input in the lock-in amplifier to reduce the non-signal interference (peak) noises (AC).

In summary, the workflow of using a lock-in amplifier is first to characterize noise floor (y-axis in log-scale) and use this information to finish the input noise preliminary reduction to fully use the dynamic reserve. The noise floor also guides us to select the best modulation frequency and optimize the filter bandwidth and order.

2.4.9 Signal modulation

(1) Double modulation

Double modulation (DM) refers to the use of demodulation under the FTIR rapid-scan mode. As discussed before, the Fourier pair under rapid-scan is the time-Fourier frequency ($t - f_F$), and the Fourier frequency $f_F = 2v\tilde{v}$ is non-physical because for a real optical signal the relation

between wavenumber and frequency, $\tilde{\nu} - t - f$, should apply the velocity of light c while the relation between wavenumber and Fourier frequency, $\tilde{\nu} - t - f$, is based on the velocity of moving mirror v. If the demodulation frequency f_r is too close to the Fourier frequency f_F, the lock-in amplifier cannot distinguish f_F from f_r, and FTIR cannot distinguish f_r from f_F. Then modulation frequency (and its harmonics) appears in the wavenumber spectrum measured by FTIR, and noises at DC are also demodulated with the Fourier frequency making the mixed spectrum too complicated (f_F mixing and its harmonics) to set a low-pass filter.

Therefore, the modulation frequency should be much higher than the Fourier frequency with the rule of thumb timeframe of about 5-10 times in case modulation frequency will not appear at the FTIR wavenumber spectrum and Fourier frequency mixed noise is far away from DC. In a practical setting, the velocity of the moving mirror can be set into a specific value, which means the Fourier frequency $f_F = 2v\tilde{\nu}$ becomes higher for larger wavenumber $\tilde{\nu}$ region at FTIR spectrum. For example, if $v = 0.04cm/s$ is set, we can assume a large wavenumber upper bound $\tilde{\nu}_{max} = 10000cm^{-1}$, although we may only measure the spectrum $4000 - 600cm^{-1}$, and the maximum Fourier frequency is then $f_{F_{max}} = 800Hz$ resulting in the lower bound of modulation frequency about $f_r = 4kHz$ in DM mode. Lower mirror moving velocities allow lower modulation frequencies, but can also increase the data collection time, since the total spectrum range of interest is typically fixed (4000-600cm^{-1}).

The setting of the lock-in amplifier should have the cutoff frequency and order of the low-pass filter include the Fourier frequency but exclude all other frequencies (modulation). This is the reason why f_F should be far away from f_r leaving enough space for low-pass filter parameter optimization.

DM mode is still under rapid scan and includes the setting of a number of scans. Larger scan times can have a higher average and improve the SNR. A further increase of the scan times has inconspicuous effects mainly due to the detector/amplifier noise. At this highest resolution, the repeatability of different scans and stability of the device under test could not be guaranteed, and therefore, only one scan is normally used even in DM mode.

(2) Step-scan modulation

Step-scan modulation (SSM) is the extreme case of the DM mode, and its Fourier frequency becomes zero since the mirror is moved step-by-step with no continuous velocity. Each step will finish a complete demodulation process. This means SSM mode ideally can be operated at any modulation frequency, but the price is the extraordinary long data collection time, during which the stability, reliability of the system, and random interference from the circumstance become uncontrollable, and the patience of the operator has also been tested. Furthermore, in SSM mode, the "instant" response feature of the FTIR is entirely lost, as the operator cannot instantly see the effects of operation (such as optical path alignment) but needs to wait a few minutes for the results. Without the help of catching a weak traceable signal at a previous rapid scan or double modulation, the operation of SSM mode independently becomes extremely difficult, especially for a new operator with an unknown sample at hand. Therefore, SSM mode is typically occurs at final stage after the survey by DM mode.

In addition, under extremely low modulation frequencies, the step-scan itself becomes nonvalid since the mirror is still moving and has a "velocity" although, it is moving step-by-step. Longer step settling time may mitigate this "velocity" but again there is concern due to the extremely long data collection times. The rule of thumb is that the average time per step should be set to a minimum of 10 full periods of modulation, even now under step-scan mode. For example,

in an experiment with modulation frequency as $5Hz$, set the average time per step to at least $(1/5)s \times 10 = 2s$.

Another issue of SSM mode is that its resolution is low since high resolution requires an extremely long data collection time. In addition, SSM mode is mainly for SNR improvement, but higher resolution can cause lower SNR. A rough resolution (larger step) can be regarded as an average effect and has easier and more stable controlling of the step moving. Lower resolution means we may only measure an envelope of the spectral feature, although the SNR is high.

In both DM and SSM modes, the data acquiring time is related to the spectral span and resolution directly. We thus can choose appropriate spectral span and resolution to balance the tradeoff between the data collection time and SNR.

2.4.10 Optical system design

The main optical system design is to include a microscope to extract the optical signal from some microdevices as shown in Fig. 2-11. There are two purposes of setting up a microscope with two working modes respectively. For the image mode (optical magnification; CCD), we need to find and locate the target micro-device. For the signal mode (infrared magnification; MCT), then we can extract/enlarge the beam size of the micro-device to the MCT element size. The further optical system includes the internal optical path of FTIR as shown in Fig. 2-19.

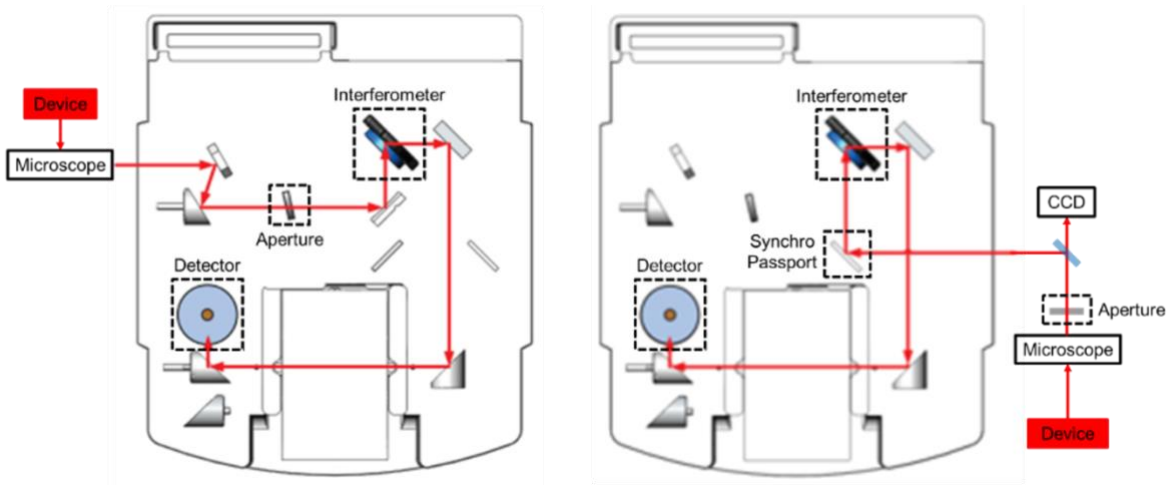

Figure 2-19 Our FTIR (Thermo Fisher iS50) has two optional entrances for an external source (emitter) controlled by the Synchro-passport. Left-entrance can be combined with a self-made microscope with more flexibility and a shorter optical path distance, while right-entrance applies the FTIR Continuum Microscopy with more stable and accurate operations. Note there is only one interferometer at FTIR Main.

The final beam size or mode profile of the device that will be collected depends on the field of view (FOV) of the reflective objective, as well as the size of the aperture after the microscope (for both left- and right- internal optical paths).

Aperture is conventionally a tradeoff between sensitivity + SNR and resolution. A larger aperture can result in a higher sensitivity since more light is hitting on the detector chip (finally saturated because of overfilling of a finite size of the chip). The SNR is also increased and saturated from underfilling to overfilling because of less chip area for dark current. A smaller aperture can make the measurement more stable and accurate and is needed for high-resolution. Resolution is not decided by the aperture but needs the aperture to reduce the grazing-incidence of light. For conventional measurements, notice the sample holder can possibly serve as an additional aperture when measuring the background spectrum.

The situation becomes more complicated for microscope FTIR. A microscope (reflective objective) is used to enlarge the beam size (mode profile) of the device at the microscale. Since the magnification of the reflective objective is typically not large (compared to the lens for optical wavelength), the FOV is relatively large, and the reflective objective thus also enlarges the light beams from surrounding backgrounds or unwanted areas. To solve this, we further implement an aperture to chop the enlarged total light beam's edges to make sure we only collect the IR light beam from the small device, as shown in Fig. 2-20. The aperture now has two roles: one is for CCD imaging; the other is for MCT sensing. The aperture chops the enlarged beam size (image), and only the sample image we want is left. The CCD imaging is then a monitor to help us pick up the device area with a motorized translation stage. Note the image formed by CCD is only a rough guide since the final MCT sensing is for infrared wavelengths, which are invisible. The longer infrared wavelengths typically have a larger field of view after an aperture (pinhole) compared to the visible wavelengths. However, if the device beam size, for example the aperture size, is above the diffraction limit, the CCD guiding is still considered to be accurate.

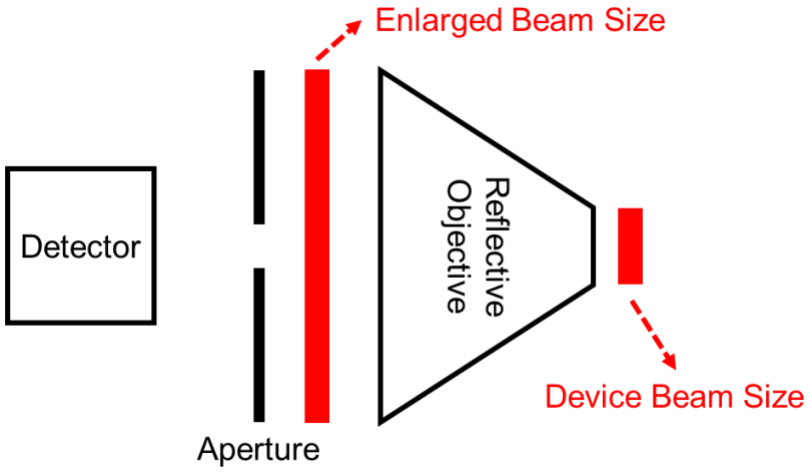

Figure 2-20 Zoom-in schematic of the optical system.

Shrinking the aperture size down to the enlarged device beam size can reduce the noise from device ambient areas and thus increase the SNR. However, a too-small aperture can cause the MCT chip to underfill, i.e., the final light beam that enters the detector cannot cover the whole area of the chip, leaving a large area experiencing dark currents. This can lower the SNR and sensitivity significantly. We thus have a trade-off: on the one hand, we want to use a smaller aperture to restrict enlarged beam size to make sure we only collect light from the small sample, which improves SNR; on the other hand, we need a not-too-small aperture to make sure the MCT chip is not underfilling, otherwise reducing SNR and sensitivity.

Influence of underfilling, fullfilling, and overfilling on MCT chip: underfilling is that the chip is not fully filled, thus reducing SNR. Fullfilling is the standard case. Overfilling a little bit can be beneficial since the directional detection (detectivity) of the chip, but "saturated" if the overfilling is too large. In summary, we need to avoid underfilling, while overfilling is unnecessary and may cause lower SNR and sensitivity when using a microscope.

To handle this tradeoff, we can first use a reflective objective with large magnification, and then the enlarged beam size (or larger percent of it) is already from the small sample, not from the surrounding. We then do not need a tiny aperture for a further restriction. However, the magnification of a reflective objective is typically unable to reach a FOV at the micron level. Even with a high-power objective, the working distance is typically too short compared to the gap between the device and the cryostat window. Also do not forget our device is working at high temperature and can damage the objective if they are too close to each other.

Therefore, it seems unavoidable to use an aperture and needs a careful balance for the tradeoff. We can adjust the aperture from fully open to close and find the optimal size. We may

also use a smaller size of the MCT chip, which is typically installed for current microscope FTIR, but this is only for SNR compensation (no dark current), not for the sensitivity (small area).

In summary, microscope FTIR has an additional requirement of the aperture for chopping the unwanted beam area compared to conventional measurement, with tradeoffs now in the sensitivity + SNR and resolution + background-chopping(SNR).

To experimentally demonstrate the narrow-band or spectrally-selective response from the fabricated emitter, we plan to measure its thermal emission spectrum, which is directly correlated with the resonant mode of the coupled emitter and detector in the transducer. The proposed setup for measuring the emission spectrum of an arbitrary nano-emitter is shown in Fig. 2-21. The setup consists of a microscope which first images the nano-emitter using visible light. Infrared radiation emitted by the nanoemitter is then collected by a Cassegrain-type reflective objective lens and guided to a FTIR spectrometer in which a nitrogen-cooled mercury cadmium telluride (MCT) detector measures infrared light from 0.8 to 16.7μm. The FTIR includes a Michelson interferometer and a beam splitter separating the incoming thermal emission into two beams. The electrically driven nano-emitter allows us to modulate its temperature and thereby thermal emission of the nano-emitter at a certain frequency while maintaining the environment (including the substrate and the detector) at a low temperature. An AC current oscillating at frequency ω with a DC offset will be applied across the nano-emitter. This induces a temperature variation of the nano-emitter at frequency 2ω. A lock-in amplifier that measures the signal at frequency 2ω is connected to the output of the MCT detector. In this case, the FTIR will be operated at a step-scan mode in which the optical path difference between two beams is changed step by step through moving mirrors. The AC measurements can significantly increase the signal-to-noise ratio by introducing the modulation in the heating.

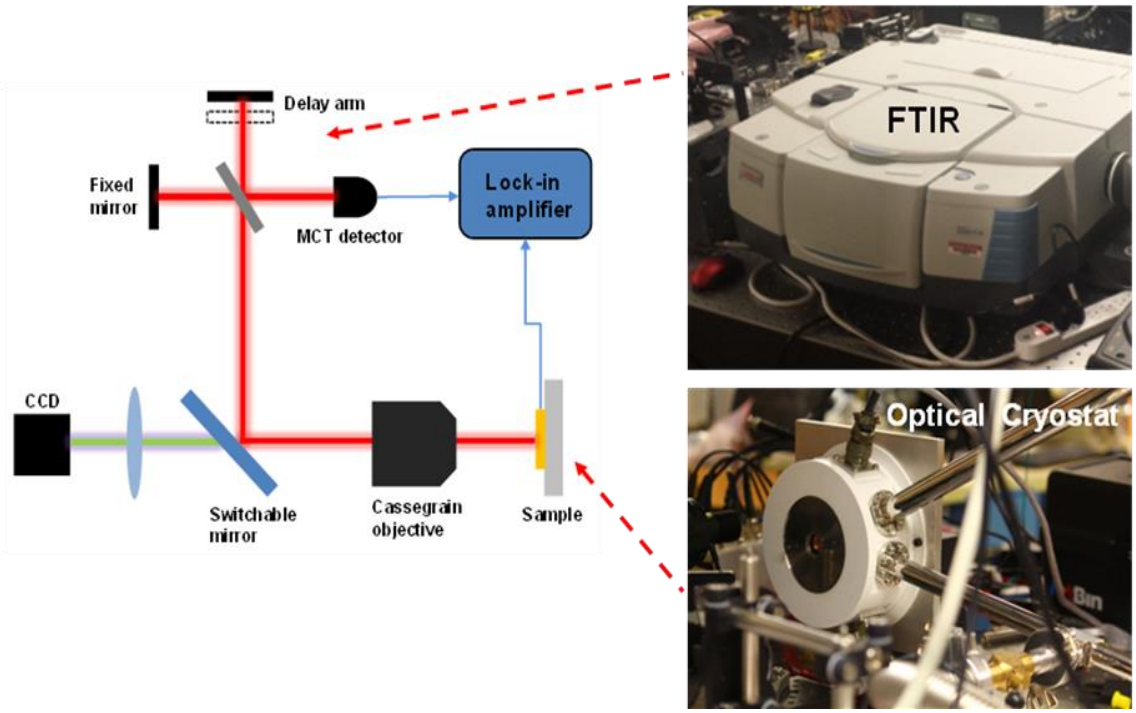

Figure 2-21 Schematic of the optical path and our FTIR direct emission measurement system.

As mentioned previously in Fig. 2-11, in term of the external optical path we need to use for measuring the emission from the emitter, we come up with two ideas as shown in Fig. 2-22. There are 2 steps before we can measure the emission spectrum from the external module of FTIR. First, aligning the red laser and objective lens to be coaxial in the horizontal direction, and then we need to align the red laser and white light source to be coaxial, and once these two steps finished, we can flip the switchable mirror to proceed with the emission measurement.

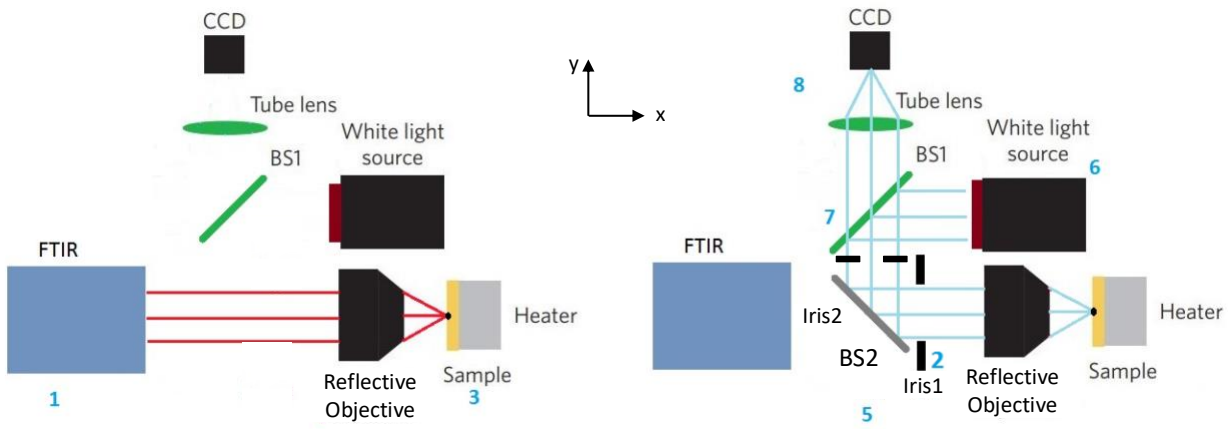

Figure 2-22 Schematic of two different measurement steps.

2.4.11 Microbar thermal emitter measurement results

To verify our analysis of the measurement system, we have fabricated a microbar thermal emitter as shown as inset of Fig. 2-23(a). 100nm thick Au microbar is directly deposited on a quartz substrate. With length of 1500μm and width of 80μm, the microbar is well connected with 4 electrodes. Based on the measurement setup in Fig. 2-13, the reflective objective is well focused by the linear translation stage, and we can see the shape of the microbar is well illuminated by the guiding red laser spot from the FTIR.

We measure the microbar thermal emission under 0mA (off-state) and 100mA (on-state) under rapid-scan of FTIR, and as shown in Fig. 2-23(a). Most spectral information is then buried in the thermal background centered at around $1000cm^{-1}$. Our measurement setup based on step-scan and PSD is then able to abstract this buried information as shown in Fig 2-23(b).

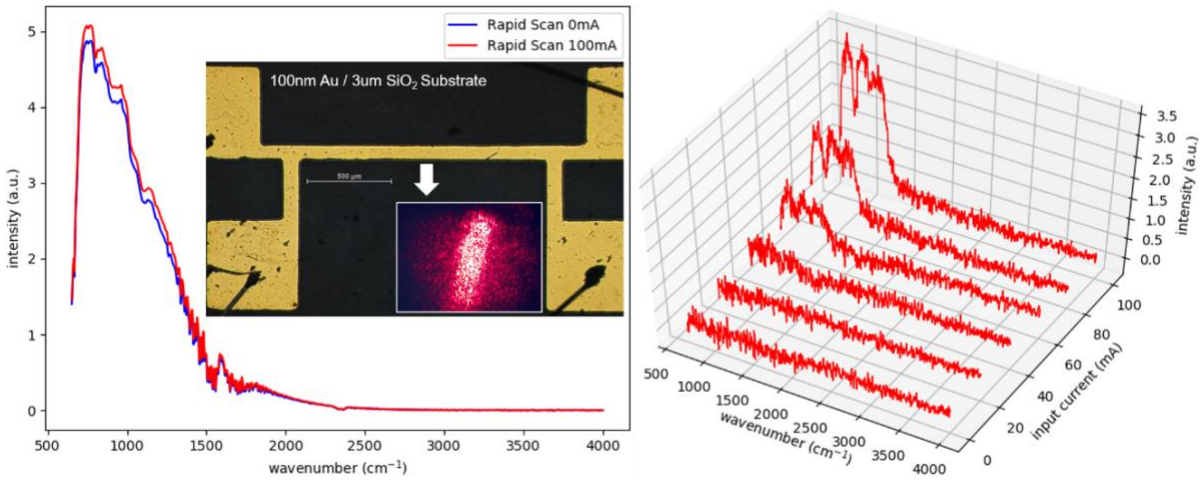

Figure 2-23 (a) Microscope image of the microbar thermal emitter, which is well focused by a reflective objective and illuminated by the guiding red laser from FTIR. Spectral information is buried in the thermal background under rapid-scan. (b) Spectra under different current input under our thermal measurement setup with step-scan and PSD for noise reduction. Clear dips are $700cm^{-1}$ for quartz substrate absorption.

The main effort is to optimize the signal process of the lock-in amplifier, and make sure the experimental results are consistent with the python simulation discussed above. As shown in Fig 2-24(a), with decreasing reference frequency, the effect of the Fourier frequency (non-ideal step-scan) becomes severe, and background noises appear when the reference frequency is below 125Hz. However, with a high reference frequency, the composite response of the emitter and FTIR measurement system is no longer fast enough, resulting in the decrease of signal intensity. Similar analysis is also on the time-constant. Larger time constant, i.e. smaller cutoff frequency, results in more noise reduction, and SNR is significantly improved when time constant increases from 1ms to 100ms as shown in Fig. 2-24(b). Some background noise peaks even appear when the time constant is too small. However, further increase of the time constant makes the bandwidth of low-pass filter too narrow to cover the full signal range, and the signal spectrum starts to deform and

then finally disappear when the time constant increases up to 1s. This tradeoff again sets an optimum of the time constant, and for our microbar thermal emitter, it is 100ms 6dB, as shown in Fig. 2-24(c).

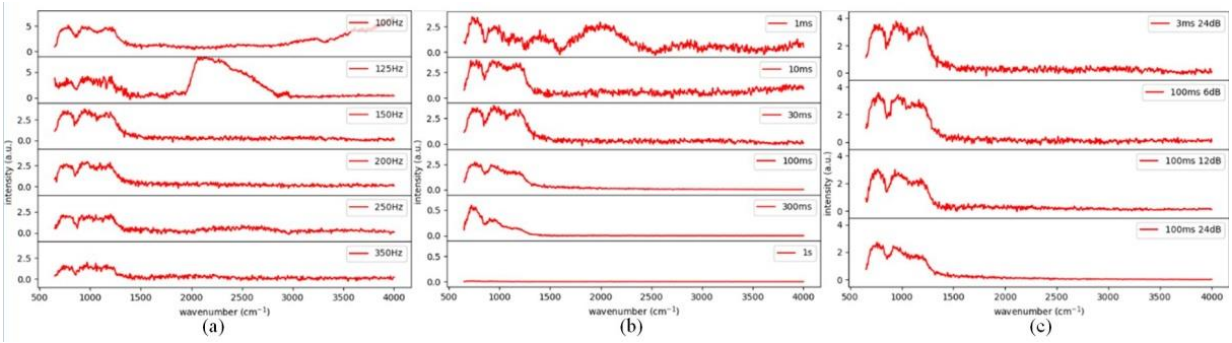

Figure 2-24 Reference frequency and time constant are optimized based on the effect of non-ideal step-scan and low-pass filter. (a) modulation frequency (b) time constant (c) filter order.

A further investigation is done on the harmonics of reference. Since the modulated thermal signal is the full-wave rectified sin wave whose frequency is double the reference frequency, only even harmonics of reference can pick up the thermal signal. As shown in Fig. 2-25(a), 1st order harmonic of reference is dominant, and higher orders only can barely see the signals because of not only the lower amplitude in the Fourier series but also the higher reference frequency resulting in lower response of the measurement system. In our spectral analysis, only the 1st order will be considered. Complementarily, we can also check the odd harmonics of reference, and no signal but just background peaks which appear both when the emitter is on (100mA) and off (0mA) as shown in Fig. 2-25(b).

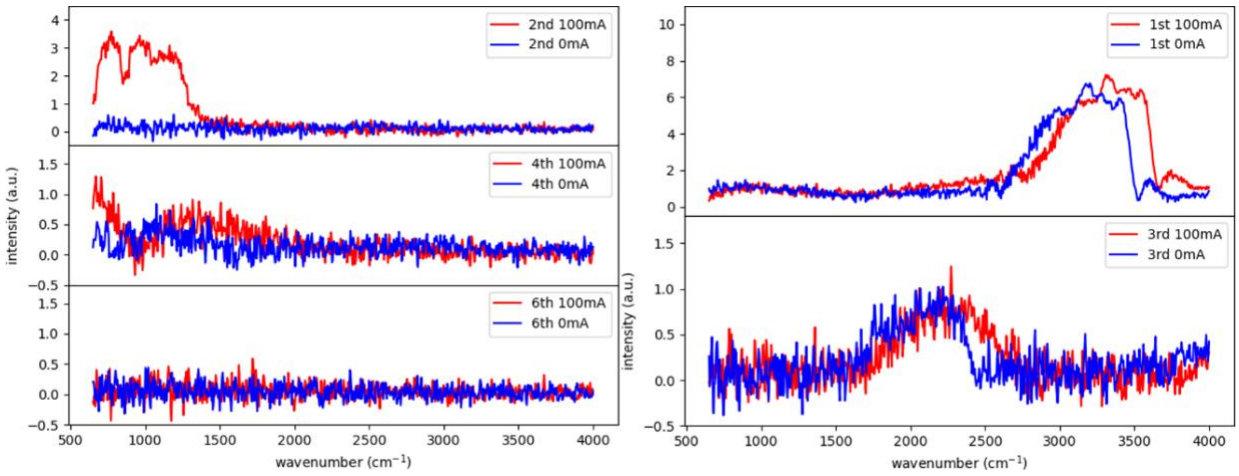

Figure 2-25 (a) Demodulated thermal signal under even harmonics of reference. 1st order is dominant. (b) Demodulated thermal signal under odd harmonics of reference. Only background peaks are picked up (both exist when microbar emitter is on and off).

Finally, we can check the emission spectra of our thermal emitter with increasing input current as shown in Fig. 2-25(b). Overall, we see a blackbody radiation since 80um width of microbar is considerably larger, and a clear dip at $700cm^{-1}$ is due to the absorption of quartz substrate.

3 Near-field thermal emission overview

3.1 Near-field thermal emission overview

As we discuss in the introduction, the near-field thermal radiation from nanoplasmonic structures could be of great interest due to the nano-scale size effect. Here, in order to study the near-field thermal radiation from nanoplasmonic structures, we fabricate the on-chip nanoplasmonic emitter and sensor, where the nano-scale infrared emitter and detector are separated by a gap as small as ~50 nm. The nano-resonators will be made from chromium or platinum due to the material properties and fabrication compatibility. As demonstrated in our preliminary work, we will fabricate the electrically driven nano-emitter and nano-detector using combined e-beam lithography and photolithography. The nano-emitter/-detector will be fabricated by e-beam lithography, whereas their respective four-probe electrodes are patterned by photolithography. The device fabrication will begin from a 525-μm-thick silicon wafer, and then a 300-nm-thick silicon nitride (SiNx) thin film is deposited on both sides of the substrate using plasma enhanced chemical vapor deposition, which serves as the infrared-transparent dielectric spacer, and the thermal insulating layer due to its low thermal conductivity around 3W/m·K. To separate the emitter and the detector with a nanoscale gap, and the gap distance varies from 50nm all the way to 500nm for the measurement purposes, however, all these values still fall into the near-field radiation regime. Therefore, we will employ FIB milling to build a trench between them. The schematic is shown below in Fig. 3-1, where the red nanowire is the emitter light source and the yellow one is the receiver in this case.

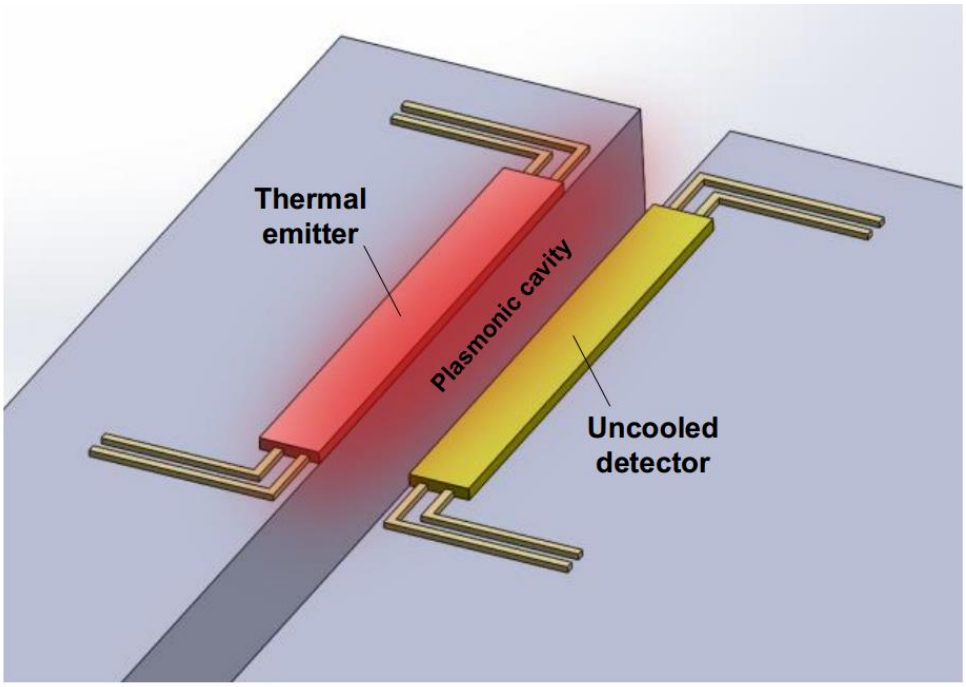

Figure 3-1 Schematics of the emitter and detector system on a chip for near-field thermal radiation from nanoplasmonic structures.

3.2 Single nanowire and plasmonic cavity design

For both the emitter and sensor, we enhance the emission and absorption properties via the same optimization method we use in the previous far-field thermal radiation discussion. To quantitatively evaluate the field enhancement effect in the plasmonic cavity formed by an emitter and a detector in Fig. 3-1, we perform proof-of-concept simulations on the electrical field intensity and the radiative heat flux between two gold nanorods at different gap distances and temperatures. As one example, we consider an emitter-detector pair made from two identical square-shape gold nanorods, where the length and the size of each nanorod are 3μm and 80nm, respectively. The gap distance between the emitter and the detector ranges from 50 nm to 5 μm. At the resonant frequency, Figures 3-2(a) and (b) plot the electric field profiles of the emitter-detector pair for a 50nm gap, where the electric field is highly concentrated in the gap (or plasmonic cavity) between

the emitter and the detector. Averaged electric field intensity was plotted as a function of gap size in Fig. 3-2(c). It can be clearly seen from Fig. 3-2(c) that even for this non-optimized emitter-detector pair, the enhancement of electric field intensity at a 50nm gap can be 4 orders of magnitude larger than the case for a 5μm gap. In Fig. 3-2 (d), we plot the total energy flux as a function of gap distance by integrating the corresponding spectral heat flux. At the gap size of 50nm, the calculated energy flux is ~ 100 times larger than the blackbody radiation.

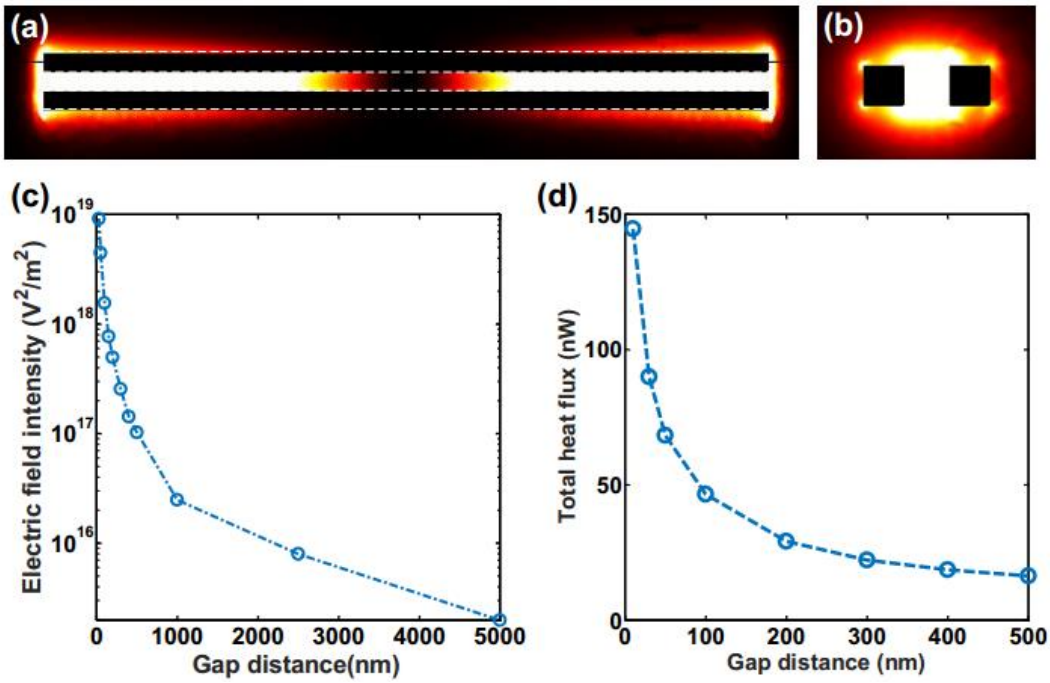

Figure 3-2 (a) Normalized electric field profile between two nanorods with a gap distance of 50 nm; (b) Electric field profile at the cross sectional plane that is 150 nm from the nanorod end; (c) Averaged electric field intensity as a function of gap distance; and (d) Total heat flux as a function of gap distance.

3.3 Thermal and mechanical performance analyses of the nanoplasmonic device in the near-field radiation regime

Here, our goal is to finalize the design of the device and substrate from perspectives of thermal, electrical and mechanical simulation by conducting thermoelectric simulations in ANSYS. From the temperature, stress and deformation analyses, we are able to find out the optimal design for the nanowire, required thickness of each substrate and effective ways to prevent heat transfer by conduction as well as to maximize the thermal emission. Important results and implications will be discussed in the following sections.

A nanoscale device for near-field radiation detection with excellent thermal and mechanical performances is designed based on the numerical simulation in commercial software ANSYS Workbench. The geometrical parameters of the device are delicately adjusted in order to balance multiple indicators of the device, which are listed as follows:

- Improve the emitter's temperature uniformity;
- Reduce the emitter's deformation due to thermal stress;
- Prevent heat conduction from emitter to detector;
- Evaluate the temperature increase of the detector due to thermal radiation.

3.3.1 Design of the device and substrate

Figure 3-3: Schematic of the substrate design.

As shown in Fig. 3-3, the nanoscale device includes a multiple layer design which are silicon substrate, SiNx thin film, and emitter/detector/electrodes layer. In order to prevent the heat conduction from the emitter to the detector, a rectangular bottom hole in the silicon wafer is drilled by wet etching and a groove between the emitter and the detector are fabricated using focused ion beam.

At the surface of the silicon nitride layer, electric heating pads are connected to the sensor and the emitter (both made of platinum or chromium), which are separated by a nanosized trench. As electricity loops through the heating pads, the emitter will be heated, thereby giving out thermal radiation to the detector. Such signal change will then be detected by the sensor on the other side of the trench and help us determine how much the near-field thermal emission transferred in between the emitter and detector.

The temperature drop inside the emitter is mainly attributed to the heat dissipation through the electrode. Therefore, a small heater is added to the emitter, and the emitter is heated up by heat conduction instead of by joule heat. Moreover, the structure and size of the groove as well as the bottom hole are well selected in order to balance the thermal and mechanical performances of the device, which will be presented in detail in the following section.

The emitter of the device is heated by current and irradiates thermal radiation to the detector. Such temperature increase in the detector due to the near-field thermal radiation serves as the signal that is monitored during experiment. A more uniform temperature distribution of the emitter is beneficial for the near-field radiative signal detection. However, both the emitter and detector are fabricated on the same substrate, and the temperature increase due to heat conduction could become a noise signal. Therefore, the numerical model of heat transfer in the device is necessary,

which is used to analyze the temperature uniformity of the emitter and design a special structure to block the heat conduction from the emitter to the detector.

3.3.2 Heat transfer simulation method

In the first step, the simulation method is established to evaluate the temperature distribution in the emitter and the heat conduction process from the emitter to the detector. The current flow and the heat conduction are coupled inside the device. The joule heat induced by current is an energy source which is added to the energy conservation equation. Therefore, the Thermal-Electric module in ANSYS Workbench is firstly selected to simulate the entire energy transfer process, as shown in Figure 3-4.

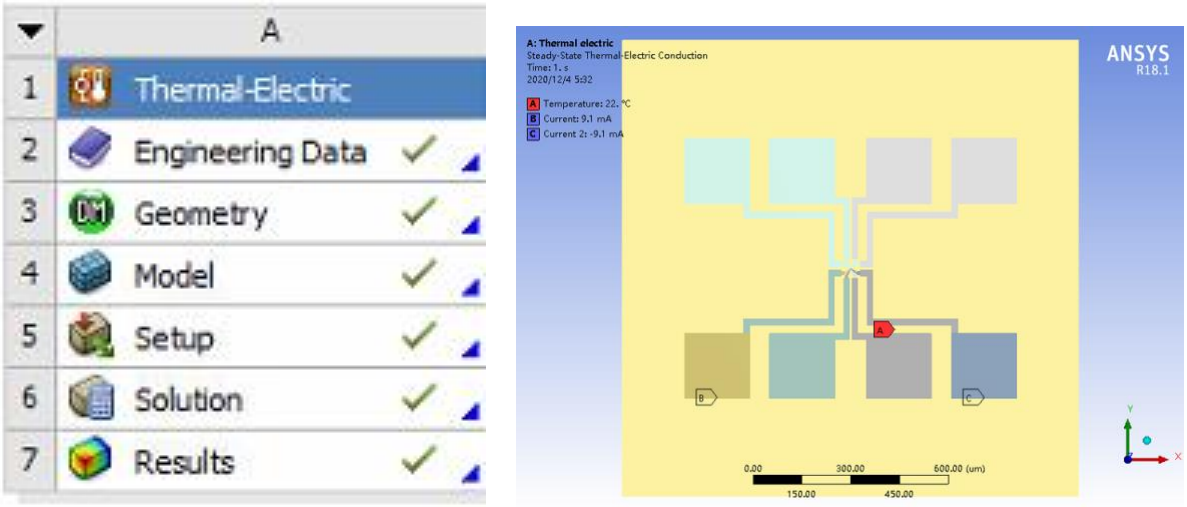

(a) (b)

Figure 3-4(a)Thermal-electric module (b)Boundary conditions in steady-state thermal-electric simulation.

The following procedure is implemented to set up the steady-state thermal-electric simulation:

1) Create a *Thermal-Electric* module in the current workspace;
2) Define material properties (thermal conductivity, resistivity) into the *Engineering Data* tab;
3) Establish geometrical model of the device into the *Geometry* tab;
4) Under the *Model* tab, define material for each part;
5) Under the *Model* tab, create contacts between every two contacting surfaces; All contacts are selected as "Bonded", meaning that two contacting surfaces are completely fixed relative to one another;
6) Under the *Model* tab, create meshing. Add refinement to smaller parts, such as emitter, heater and detector;
7) Set up boundary conditions. Set the temperature of the bottom surface to be 22°C (room temperature). Apply inlet and outlet Current boundary conditions.

From Fig. 3-4, it is shown that the entire simulation domain is extremely large compared to the size of the emitter. An extreme fine mesh is required, and it is found that the thermal-electric simulation is hard to converge because of the coupling between electricity and heat. Therefore, an alternative steady-state thermal model is recommended due to its simplicity in solution convergence. The joule heat induced by current is substituted by body heat source, which is calculated based on the current, resistivity of the material, and the cross-section area as presented in Eq. (3.1). Due to the largest resistivity difference between chromium, SiNx, and silicon wafer, the body heat source inside the SiN_x and silicon wafer is considered to be negligible.

$$q = \frac{I^2 R}{V} = \frac{I^2 \frac{\rho l}{S}}{Sl} = \frac{I^2 \rho}{S^2} \tag{3.1}$$

where, q is the equivalent energy source, I is the current, R and ρ are the resistance and resistivity of the material, l and S represent length and equivalent cross-section area of the device. In order to increase the accuracy of the simulation, the device is segmented to different pieces because the cross-section area in different sections is different. The simulation procedure is similar to that used in the steady-state thermal-electric simulation. The energy source is applied to the device as an internal heat generation term in the software. The bottom surface of wafer is fixed to constant temperature of 22°C, and other surfaces are set to adiabatic boundary conditions, as presented in Fig. 3-5.

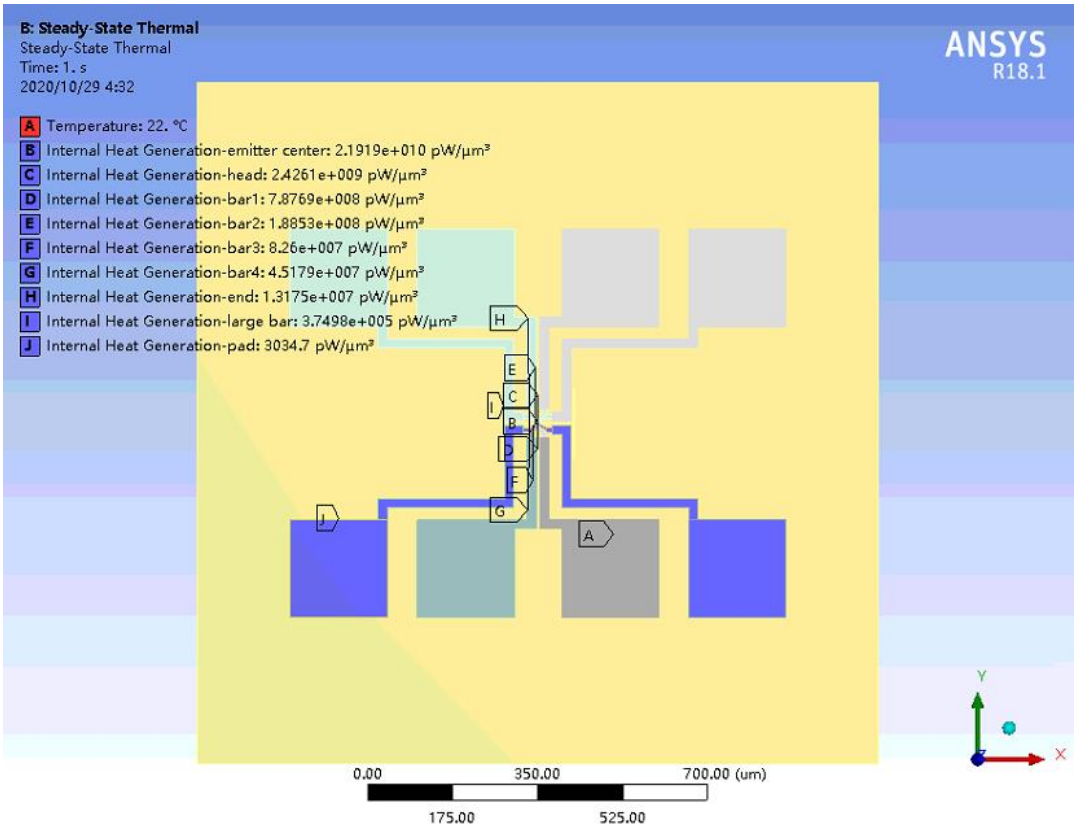

Figure 3-5 Setup for the steady-state thermal simulation.

3.3.3 Detector temperature evaluation method

During the experiment, the detector receives near-field radiation and its temperature increase is then measured as signal for determining near-field radiation. In order to ascertain that this temperature increase is measurable, the numerical simulation is established to estimate the detector temperature increase due to the near-field radiation. The steady-state thermal module in ANSYS Workbench is applied. Based on the near-field radiation simulation, the total amount of thermal energy input to the detector is assumed to be 10nW. The simulation setup is similar to that in the previous section, and geometry, contacts between surfaces, and mesh remain the same. The boundary condition is presented in Fig. 3-6, and a constant flow equaling 10nW is applied to the front surface of the detector.

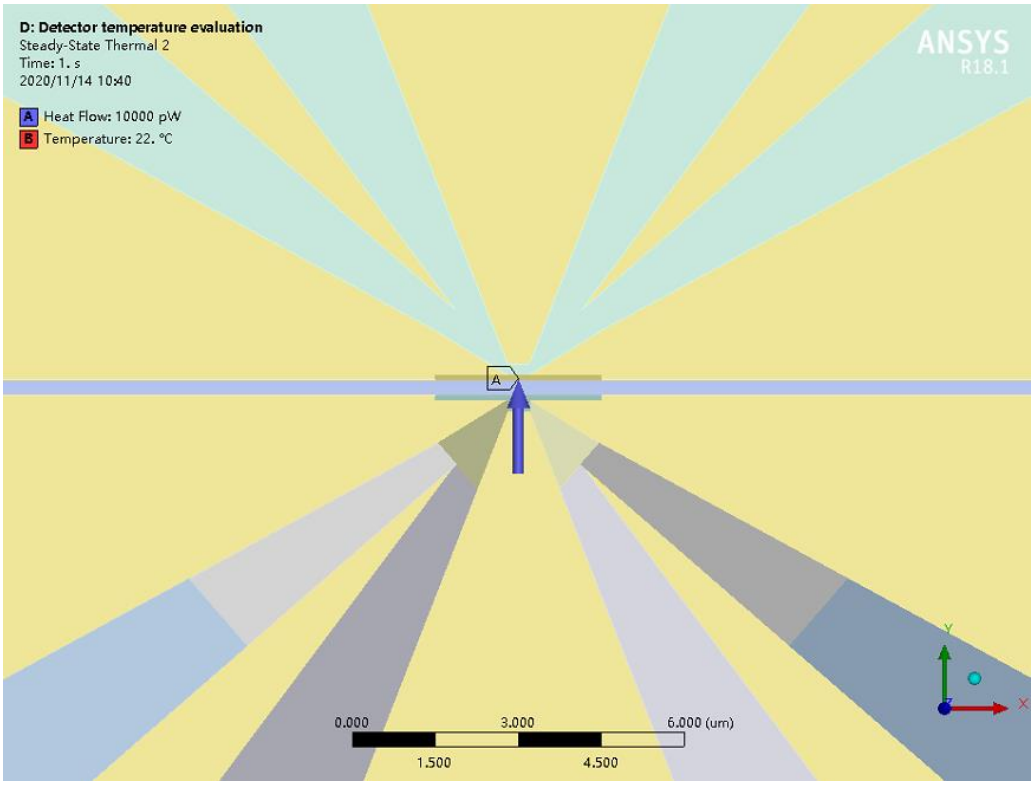

Figure 3-6 Setup for detector temperature evaluation.

3.3.4 Thermomechanical analysis method

Due to the high working temperature of the emitter, the deformation induced by thermal stress is inevitable. A coupling method based on the heat transfer analysis presented in the previous section and static structural method is built and shown in Fig. 3-7.

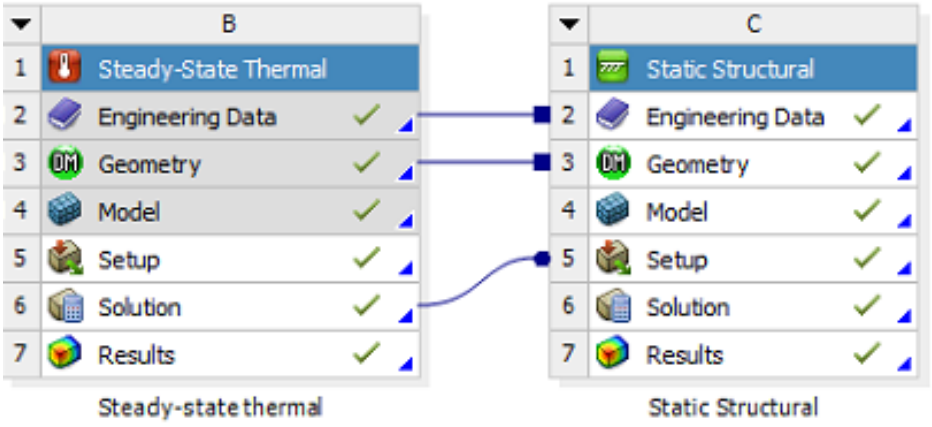

Figure 3-7 Thermomechanical coupling simulation method.

In the coupling method, the temperature distribution calculated by steady-state thermal module is imported as a body source to the static structural module. Different materials have different coefficients of thermal expansion and behave differently during the heating process. It should be mentioned that the meshes used in steady-state thermal module and static structural module are not identical. The static structural simulation normally requires a coarse mesh compared with thermal simulation. Excect for the imported temperature distribution, a fixed support boundary condition is applied to the bottom surface of the silicon wafer. The material properties, such as thermal conductivity λ, coefficient of thermal expansion α, Young's modulus E, and Poisson's ratio v are summarized in Table 3-1.

Table 3-1 Summary of material properties.

Material	λ (W·m^{-1}·K^{-1})	α (m^{-1})	E (GPa)	ν
Si	148	4.0×10^{-6}	150	0.28
SiN_x	5	3.3×10^{-6}	290	0.27
Cr	94	6.2×10^{-6}	297	0.21

3.4 Simulation results

3.4.1 Comparison of different emitter designs

In the preliminary design, the emitter is a cuboid structure and its two ends are directly connected with electrodes, as shown in Fig. 3-8(a). In this way, the current passes through the emitter and heats it up with joule heat. However, the electrodes could be considered as larger heat sinks and dissipate large amount of energy from emitter. The temperature distribution inside the emitter is therefore non-uniform with highest temperature occurring at its center. In order to mitigate this problem, an extra small cuboid structure is added which serves as a heater to heat up the emitter, as presented in Fig. 3-8(b). Compared with the emitter size, the length of the heater is small and the temperature drop inside the heater is limited. On the other hand, the emitter is separated from the electrode and its two ends are considered to be adiabatic.

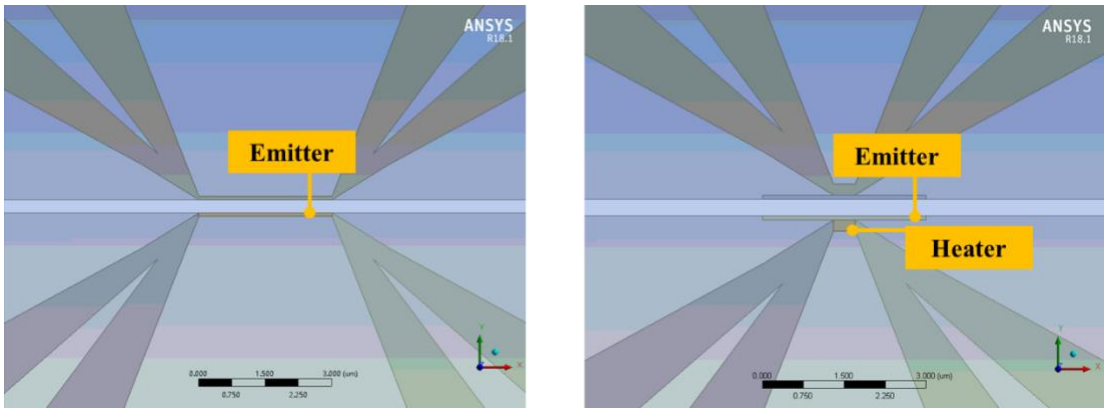

(a) (b)

Figure 3-8(a) Original design (b) Improved design of the emitter.

In order to compare the thermal performance of different emitter designs in a similar level, the emitter temperature is increased to about 400°C. The temperature contours are illustrated by Fig. 3-9. A large temperature drop from the center emitter to the end of the emitter could be seen in the original design. Quantitatively, the temperature distribution along the center line of the emitter is plotted and shown in Figure 3-10. It is obvious that the temperature uniformity in the improved design is much better. The temperature difference is 23.75°C in the new design while this value is 82.69°C in the original design.

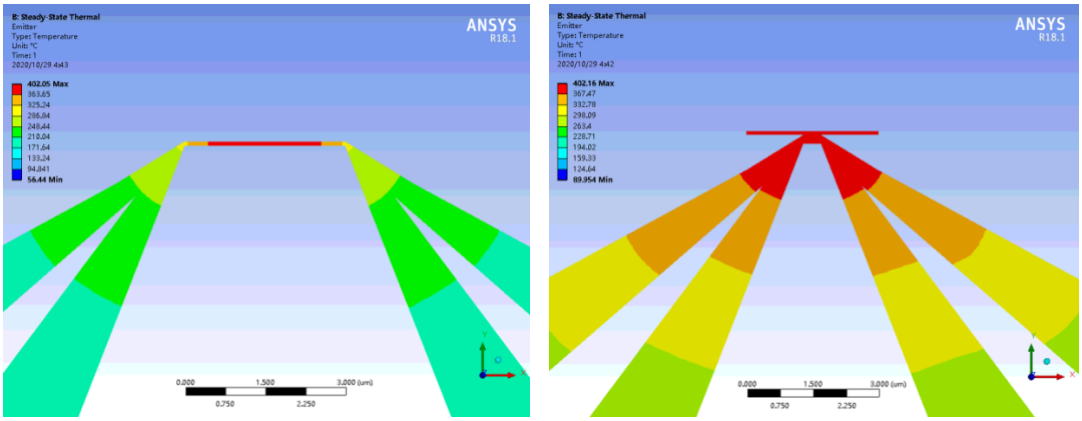

(a) (b)

Figure 3-9 Temperature contours in (a) Original design (b) Improved design of the emitter.

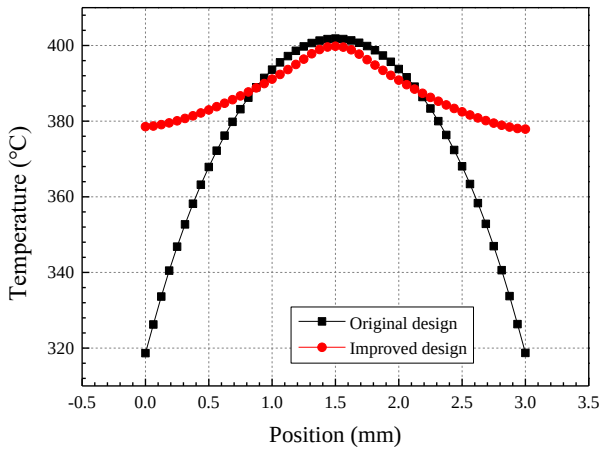

Figure 3-10 Temperature distribution along the center line of the emitter.

3.4.2 Comparison of different groove design

(1) H-shape groove design

In order to prevent the heat conduction from the emitter to the detector, the heat flow path should be large enough. Therefore, an h-shape groove is firstly put forward as shown in Fig. 3-11. With the aid of bottom hole in the wafer, the heat conduction only happens in the SiN_x layer. Furthermore, the thermal conductivity of SiN_x is relatively small compared with silicon and chromium. The h-shape groove separates the emitter and detector and confines the high temperature region on the emitter side.

A typical temperature contour is illustrated in Fig. 3-12 and the maximum emitter temperature reaches about 400°C. It is shown that the high temperature region is mostly located in the emitter side and the detector temperature increase is negligible. The influence of groove size is further analyzed, and two lengths of 150μm and 125μm are compared. The maximum and minimum temperature of the emitter are summarized in Table 3-2. The emitter temperature drop and the detector temperature increase are calculated to evaluate the temperature uniformity of the emitter and efficiency of heat conduction prevention.

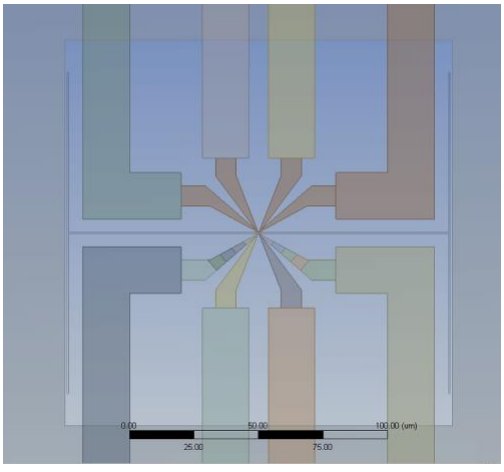

Figure 3-11 Illustration of h-shape groove.

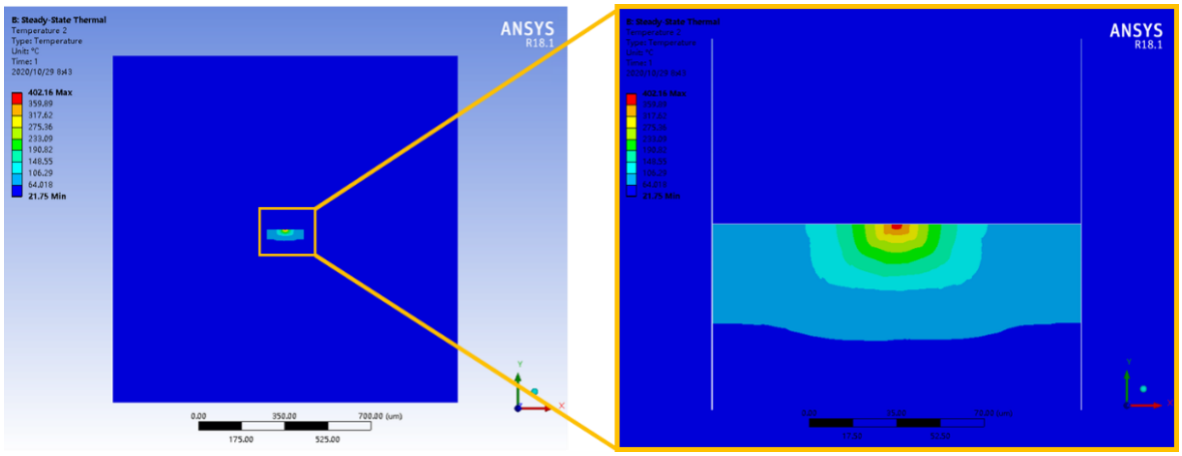

Figure 3-12 Temperature contour of the device.

From Table 3-2, it could be inferred that the groove size has small impacts on the emitter temperature uniformity and the emitter temperature drop increases as the maximum temperature of the emitter becomes larger. As for the detector temperature, a negligible temperature increase due to the heat conduction is detected (<0.001°C) even though the maximum temperature of the emitter reaches 600°C. Therefore, the h-shape groove design together with the bottom hole in silicon wafer is efficient in preventing heat conduction from the emitter to the detector.

Table 3-2 Influence of groove size on the thermal performance.

Groove size (μm)	$T_{E,max}$ (K)	$T_{E,min}$ (K)	ΔT_E (K)	$\Delta T_{D,max}$ (K)
150	401.79	378.04	23.75	0
150	604.84	568.40	36.44	0.001
125	410.76	385.13	25.63	0.001
125	608.79	570.10	38.69	0.001

Furthermore, the thermomechanical performance of the device is investigated by looking into the directional and total deformation of the device. Taking the device with 150μm groove size as an example, the directional deformation and total deformation of the emitter is shown in Table 3-3. It is found that the deformation in both x and y directions is relatively small compared with z

directional deformation, which means that the z directional deformation is the major component in total deformation. On the other hand, the temperature variation of the detector is so small that its deformation is negligible. In order to visualize the deformation of the device after temperature increase, an illustration is plotted in Fig. 3-13.

Table 3-3 Directional and total deformation of the emitter.

Groove size (μm)	$L_{emitter,x}$ (μm)	$L_{emitter,y}$ (μm)	$L_{emitter,z}$ (μm)	L_{total} (μm)
150	/	+0.041	-0.880	0.881

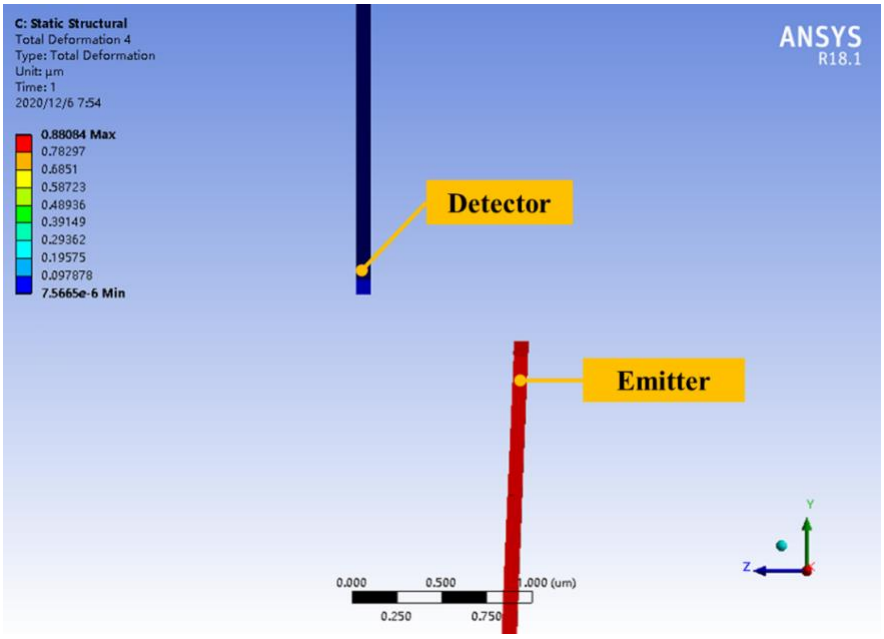

Figure 3-13 Total deformation of the device.

Due to the large temperature variation, the emitter evidently bends downwards in the *z* negative direction. In consequence, the emitter does not directly face the detector, which will possibly cause a reduction in near-field radiation received by the detector. To solve this issue, several solutions are proposed. By increasing the thickness of the SiN_x layer or decreasing the

working temperature of the emitter, the total deformation of the emitter could be limited. However, these methods are not applicable because of the fabrication or measurement limitations.

(2) Straight groove design

In the h-shape groove design, the larger deformation is partially attributed to the suspending structure of the emitter. Based on this analysis, the h-shape groove is changed to a long straight groove and the shape of bottom hole in the silicon wafer is selected as a rectangle.

In this way, the emitter is supported by the silicon wafer and the suspending part is reduced. However, the thermal performance of the device compromises due to the heat conduction through the silicon wafer. Therefore, the length of the emitter and the shape of the bottom hole should be carefully designed. The parameter sensitivity analysis is illustrated in Fig. 3-14 and the length of suspending part l_0, the vertical length of the rectangular hole l_1, and groove length l_2 are investigated. Four simulation cases are established, and the values of different parameters are summarized in Table 3-4.

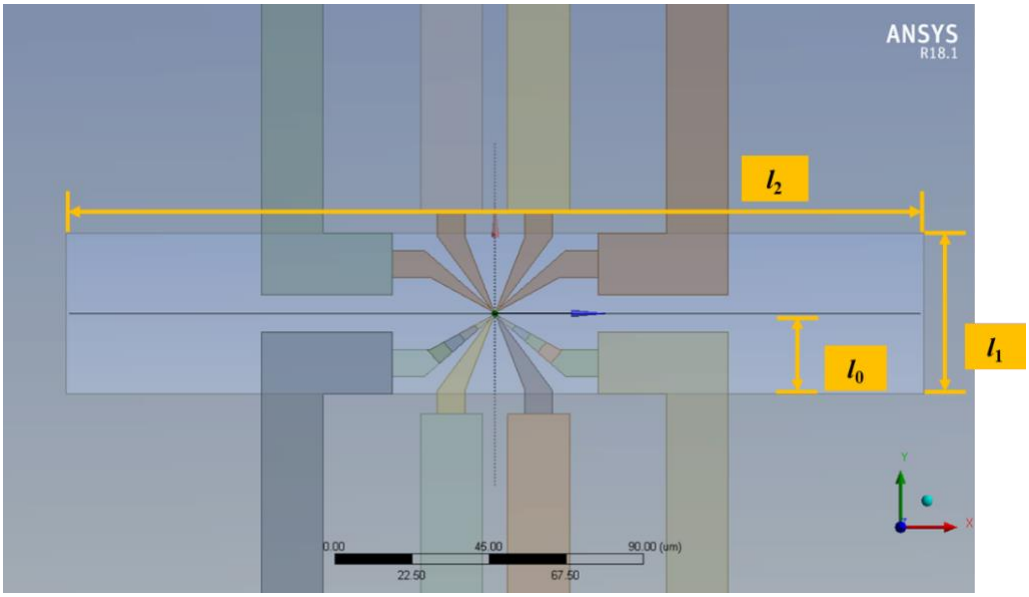

Figure 3-14. Straight groove and rectangular hole design.

Table 3-4 Parameter sensitivity analysis.

Case	l_0 (μm)	l_1 (μm)	l_2 (μm)
1	23.4	46.8	250
2	23.4	250	250
3	23.4	46.8	300
4	18.4	36.8	300

Comparing simulation results in case 1 and case 2 (as shown in Table 3-5), it is found that vertical length of bottom hole has almost no influence to the emitter temperature distribution and emitter deformation. The reason is that the silicon wafer in the detector side does not affect the emitter performance and the emitter is separated from the detector by straight groove.

Table 3-5 Influence of vertical length of bottom hole.

Case	$T_{E,max}$ (K)	$T_{E,min}$ (K)	ΔT_E (K)	$\Delta T_{D,max}$ (K)	$L_{emitter,y}$ (μm)	$L_{emitter,z}$ (μm)
1	405.80	374.50	31.30	0	+0.020	-0.105
2	405.80	374.50	31.30	0.001	+0.020	-0.104

The influence of groove length could be obtained by comparing simulation results in case 1 and case 3, as shown in Table 3-6. Based on the temperature increase in the detector, a groove length of 250 μm is large enough to prevent heat conduction from the emitter to detector. Slightly influence to the emitter temperature drop and directional deformation could be seen. However, the relative differences are only 1.4% and 5.3%.

Table 3-6 Influence of groove length.

Case	$T_{E,max}$ (K)	$T_{E,min}$ (K)	ΔT_E (K)	$\Delta T_{D,max}$ (K)	$L_{emitter,y}$ (μm)	$L_{emitter,z}$ (μm)
1	405.80	374.50	31.30	0	+0.020	-0.105
3	403.72	372.86	30.86	0	+0.019	-0.101

Furthermore, the influence of the length of the suspending part is studied by comparing case 3 and case 4, and the simulation results are presented in Table 3-7. It is firstly noticed that the

deformation of the emitter is significantly improved by decreasing the length of the suspending part. On the other hand, the emitter temperature drop increases when adding more silicon wafer on the bottom of the emitter. As a result, there is a trade-off when selecting the length of the suspending part, and the thermal performance as well as the mechanical performance of the device could not be improved simultaneously. It should be mentioned that the length of suspending part could not be further reduced because the temperature uniformity of the emitter will be dramatically deteriorated. For example, if the length of suspending part shrinks to 5.3μm, the temperature drop of the emitter will be 78.30℃.

Table 3-7 Influence of the length of suspending part.

Case	$T_{E,max}$ (K)	$T_{E,min}$ (K)	ΔT_E (K)	$\Delta T_{D,max}$ (K)	$L_{emitter,y}$ (μm)	$L_{emitter,z}$ (μm)
3	403.72	372.86	30.86	0	+0.019	-0.101
4	403.11	368.14	34.97	0	+0.016	-0.057

Moreover, the thermal and mechanical performances of the device at higher temperature is studied by increasing the emitter temperature to about 600℃. The emitter temperature and its deformation are summarized in Table 3-8. At higher temperature, the temperature drop of the emitter becomes larger due to larger heat flux. Based on the long straight groove and bottom hole design, the detector temperature increase is still negligible. As for the directional and total deformation of the emitter, they are almost linearly larger by 1.5 times compared with the results when the emitter temperature is about 400℃.

Table 3-8 Thermal and mechanical performances at higher temperature.

Case	$T_{E,max}$ (K)	$T_{E,min}$ (K)	ΔT_E (K)	$\Delta T_{D,max}$ (K)	$L_{emitter,y}$ (μm)	$L_{emitter,z}$ (μm)
1	603.45	556.39	47.06	0	+0.029	-0.155
2	603.93	556.12	47.81	0.001	+0.030	-0.152
3	603.05	556.08	46.97	0	+0.029	-0.154
4	600.18	547.13	53.05	0	+0.024	-0.086

Based on the above simulation results and considering also the fabrication tolerance, the length of suspending part, the vertical length of the rectangular hole, and groove length are selected as 20μm, 40μm, and 300μm, respectively.

Furthermore, the fragile part of the device could be identified by plotting the equivalent thermal stress distribution, as shown in Fig. 3-15. The connecting parts between heater and emitter as well as heater and electrodes suffer from large thermal stress which could be possibly due to the sharp edges in geometrical shape.

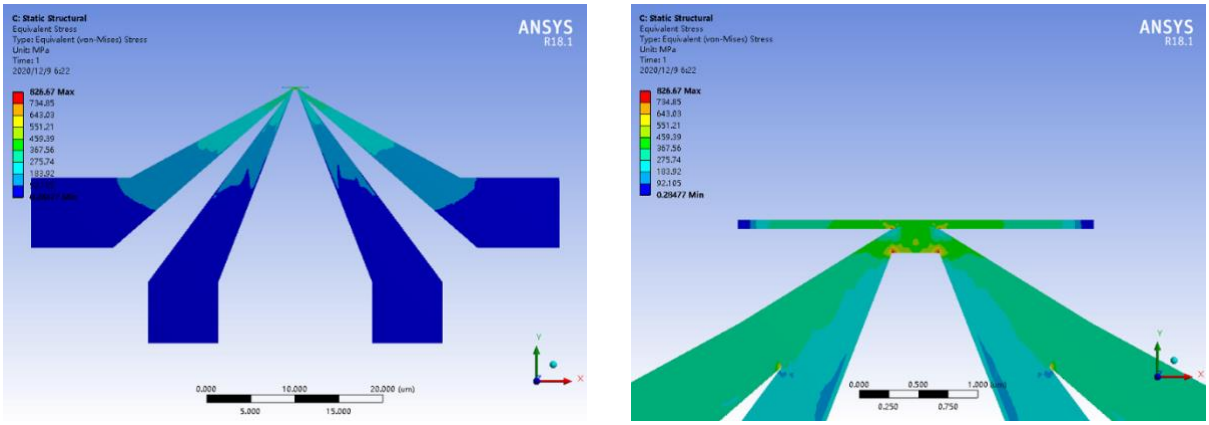

Figure 3-15 Equivalent thermal stress distribution.

3.4.3 Estimation of detector temperature increase

The detector receives the near-radiation from the emitter and a preliminary simulation is done to estimate its temperature increase. In the following simulation, the total amount of radiative energy is assumed to be 10nW. A typical temperature distribution of the detector is presented in Fig. 3-16. The temperature in the center of the detector is relatively lower than that at its ends. It is because the center part of the detector is connected to the electrodes which dissipate heat by heat conduction.

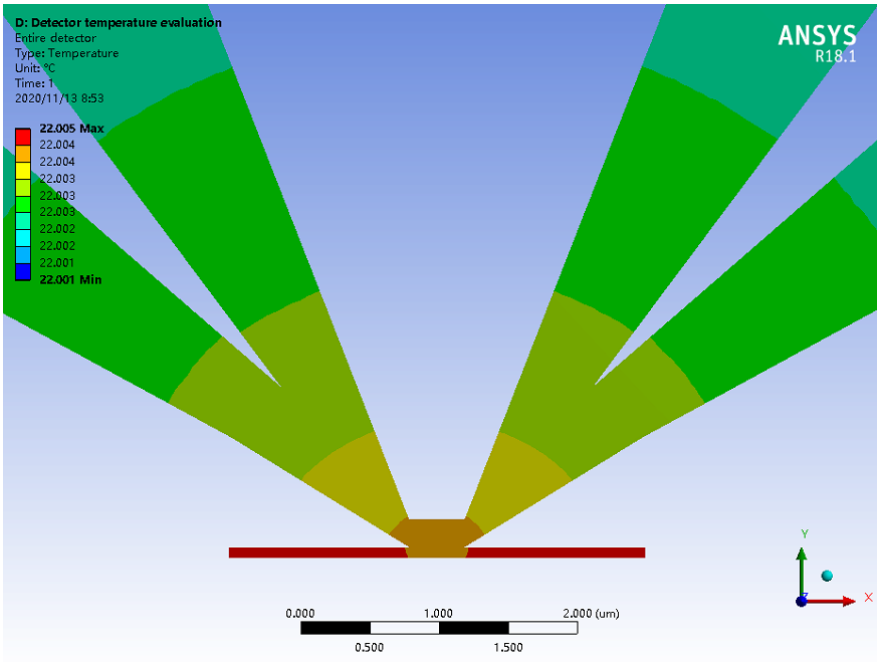

Figure 3-16 Temperature contour of the detector.

The detector temperature in the aforementioned case 1 to case 4 in Table 3-4 are calculated and presented in Table 3-9. In general, the detector temperature increase is the level of 0.003-0.005 K. The overall detector temperature increase is determined by the input radiative energy and the heat loss due to heat conduction. By enlarging the bottom hole size beneath the detector, the detector temperature could be increased as shown in case 2. However, a larger bottom hole in the silicon wafer increases difficulty in the fabrication process. Therefore, the same geometry parameters (the length of suspending part, the vertical length of the rectangular hole, and groove length) are recommended.

Table 3-9 Detector temperature increase under near-field radiation.

Case	$\Delta T_{D,max}$ (K)	$\Delta T_{D,min}$ (K)	$\Delta T_{D,average}$ (K)
1	0.004	0.003	0.0037
2	0.005	0.004	0.0047
3	0.004	0.003	0.0037
4	0.004	0.003	0.0034

3.4.4 Design with separated emitter and heater

In the previous design, one issue emerges because the SiN_x layer with high temperature will also emit thermal radiation which is regarded as noise during signal measurement. Fig. 3-17 presents the temperature contour in the SiN_x layer and the temperature distribution along the center line (x-axis direction) in the edge of this layer. It is found that the temperature is high in the region near the heater and emitter. Therefore, the influence of SiN_x layer should be eliminated during measurement.

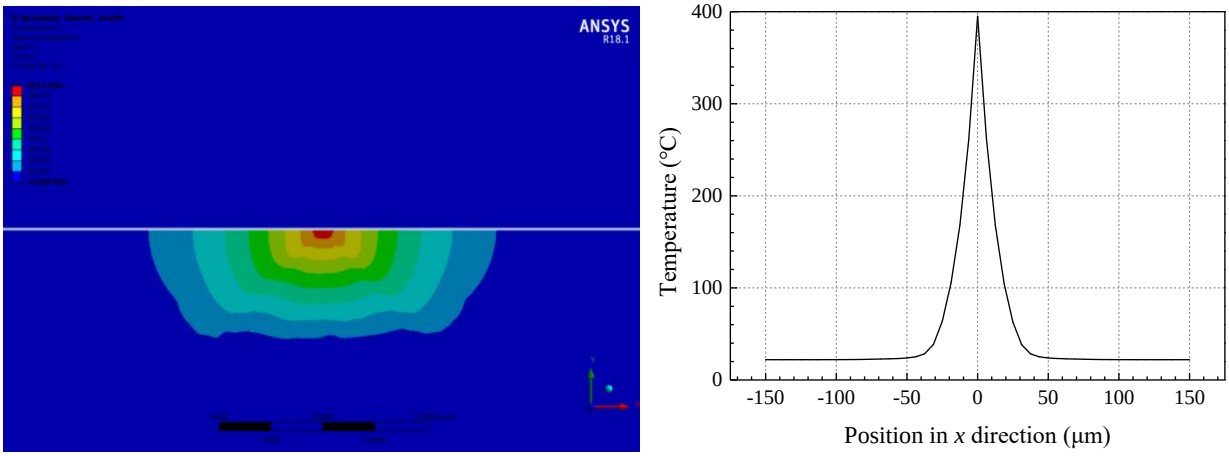

Figure 3-17 Temperature distribution in SiNx layer.

The following measurement procedure could be arranged to identify the near-field radiation signal purely from the emitter to the detector. In the first test, the complete device is used and the entire signal including noise could be measured. In the second test, the detector is removed in the device and the noise signal due to the response in the detector side is found. In the last test, the emitter is removed but the detector is kept, and the noise from the SiN_x to the detector could be recognized. It should be confirmed in the last test that the temperature distribution in the SiN_x layer remains unchanged after removing the emitter.

In order to verify this concept, a new design of device with separated emitter and heater is proposed and presented in Fig. 3-18. A small gap *d* is created to separate the emitter and heater, and the emitter is heated up by heat conduction through the SiN_x layer.

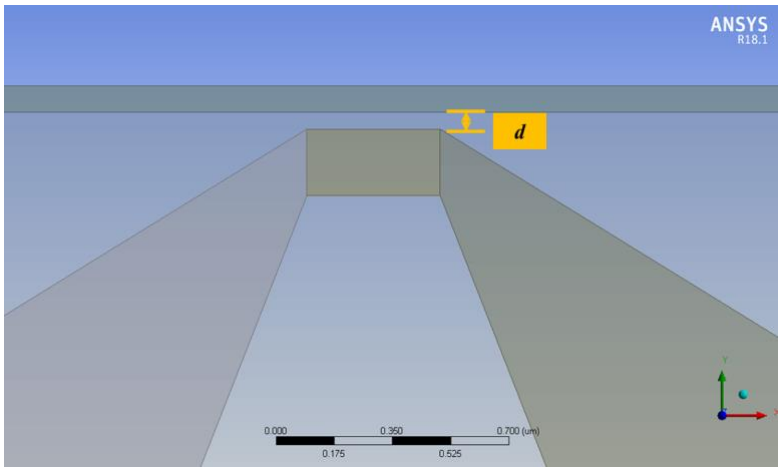

Figure 3-18 Illustration of separated emitter and heater design.

Firstly, the temperature increase of the emitter by heat conduction is checked and a typical temperature contour is presented in Fig. 3-19. It is found that emitter temperature is still increased to targeted temperature (400°C) but a larger maximum temperature difference could be expected between the emitter and heater. When the gap is set to 50nm, the maximum temperature difference between the heater and emitter is 18.6°C, and this difference will become larger as the gap increases.

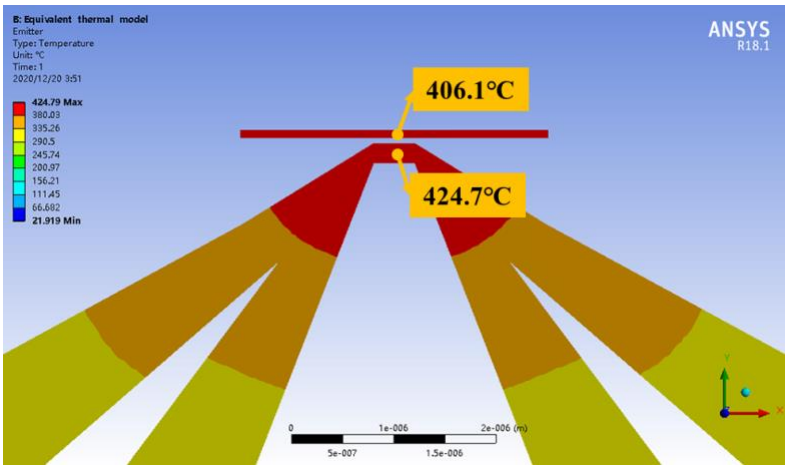

Figure 3-19 Temperature contour in the emitter/heater.

The influence of gap width is studied by setting *d* to 50, 100, and 150nm, respectively. The maximum temperature, minimum temperature, and temperature difference of the emitter are

summarized in Table 3-10. It is shown that the difference between the maximum and minimum temperature decreases compared with previous designs, which means the temperature uniformity in the emitter is improved due to the separation of the emitter and the heater. However, it should be noted that larger energy input should be applied when the gap width becomes larger.

Table 3-10 Influence of groove size on the thermal performance.

Gap width (nm)	$T_{E,max}$ (K)	$T_{E,min}$ (K)	ΔT_E (K)
50	406.66	382.67	23.99
100	402.72	381.20	21.52
150	408.69	388.40	20.29

Secondly, the temperature distribution in the SiN_x layer with or without the emitter is investigated. The gap width is fixed to 50 nm, and the energy input in these two cases are identical. The temperature contour of the SiN_x layer is presented in Fig. 3-20. It is observed that the temperature contour of the SiN_x layer is similar in the two cases. A slightly difference could be seen in the high temperature region due to the existence of the emitter. Comparing the maximum temperature in the two cases, it is found that the relative difference is only 0.71%. Considering also the similar temperature contour, it could be assumed that the temperature distribution in the SiN_x layer is unchanged with or without the emitter.

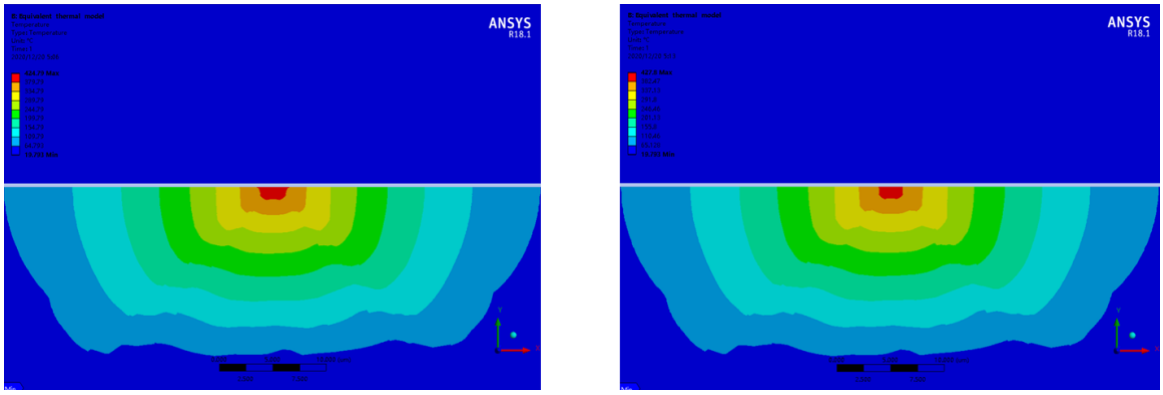

Figure 3-20 Temperature contour in the SiNx layer (a)with emitter (b)without emitter.

As a result, the above-mentioned measurement procedure could be applied to identify the near-field radiation signal purely from the emitter to the detector.

3.4.5 Conclusion

The thermal and mechanical performances of the nanoscale device for near-field radiation detection are studied based on steady-state thermal and static structural analyses. A combination of heater and emitter is proposed to improve the temperature uniformity of the emitter. A special structure with straight groove and rectangular bottom hole is designed to balance the thermal and mechanical performances of the device. Optimum geometrical parameters are also given for the next-step fabrication.

3.5 Substrate fabrication and characterization

3.5.1 Measurement method

During fabrication, stress may be presented in the thin films due to different reasons such as mismatch of the film/substrate, different in lattice structural properties, and fabrication process. In extreme cases, the film may crack, peel away, or delaminate from the substrate under large residual stress. It is therefore significant to measure the residual stress in the thin film and come up with methods to alleviate the influence of residual stress. Commonly used experimental methods include curvature method and X-ray diffraction analysis [84-87].

3.5.2 Curvature method

The preliminary work to determine the stress in thin films is done by Stoney **Error! Reference source not found.**. Stoney proposed to measure the change of curvature of the film/substrate before and after fabrication process as well as the film thickness to calculate the stress in the film based on the Stoney equation, as presented in Eq. (3.2).

$$\sigma = \frac{E_s t_s^2}{6(1-v_s)t_f}\left(\frac{1}{r} - \frac{1}{r_0}\right) \tag{3.2}$$

where, σ is the stress in the film, Es, ts, and vs are the Young's modulus, thickness and Poisson's ratio of the substrate, tf is the thickness of the film, 1/r0 and 1/r represents initial and measured curvature of the film/substrate structure. An illustration of film/substrate structure under compressive stress is shown in Figure 3-21.

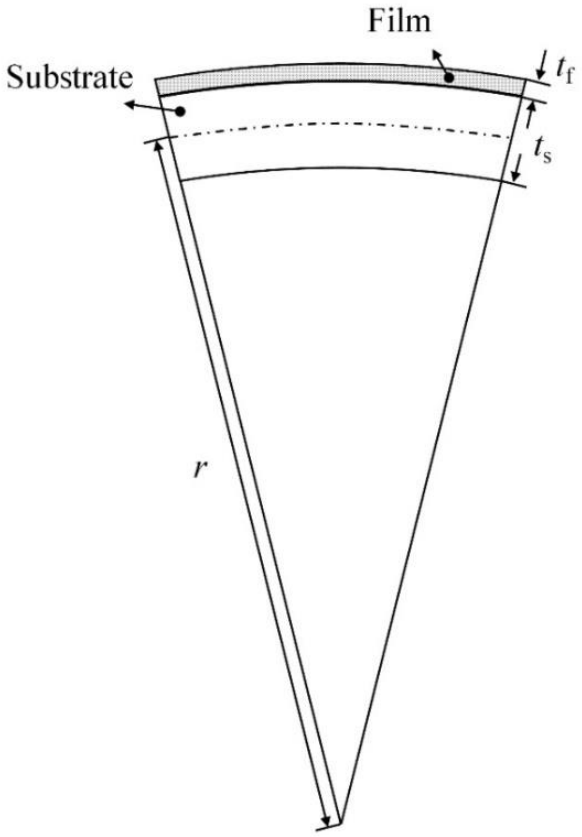

Figure 3-21 Application of Stoney equation in film/substrate structure.

The advantage of Stoney equation is that it only demands the thickness of the film and the film properties are not necessary. However, some assumptions are made for the equation which are summarized as follows.

a) The film thickness is much smaller than that of the substrate.

b) The film and substrate are homogeneous, isotropic and linearly elastic.

c) The stress component in thickness direction is zero.

d) The deformations and rotations are infinitesimal.

Ideally, for the film/substrate with uniform curvature and film thickness, the curvature changes could be measured by optical, mechanical, magnetic and electrical methods. Among different methods, the optical profilometer is usually applied to characterize the curvature of the samples. Ardigo **Error! Reference source not found.** et al. chose WYKO NT1100 optical profilometer to investigate the curvature change after TiN coated on the silicon substrate. The influence of substrate shapes on the deformation was revealed and the selection of curvature (maximum, minimum or mean value) is critical for stress calculation.

However, in most cases, the assumptions for Stoney equations are difficult to satisfy. The equation has therefore been improved to extend its application ranges. In order to consider the non-uniformity of curvature and film thickness, a localized approach using the Stoney equation was proposed. It considers that the variation in curvature and film thickness is limited in the smaller areas of substrate. For example, profilometer Tencor P-20h was used by Waters **Error! Reference source not found.** to measure the local curvature change after tungsten film deposition. The local curvature change and the calculated local residual stress in the film are shown in

Figure 3-22. It was found that that the curvature change and stress distribution are not uniform but axisymmetric due to the deposition process. Further studies presented that the transition of tensile stress to compressive occurs when the argon pressure increases.

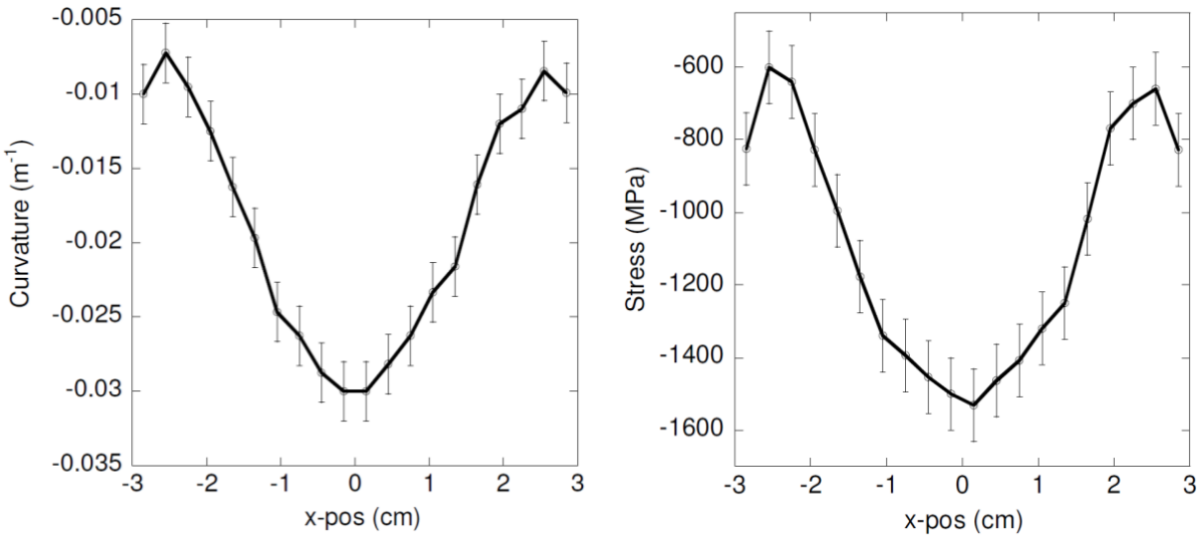

(a) Local curvature change (b) Local residual stress in film

Figure 3-22 Application of Stoney equation in non-uniform case.

Furthermore, a generalized equation for curvature in multilayer structure was proposed by Feng and Liu **Error! Reference source not found.**, as shown in Eq. (3.3). The differences in Young's modulus and growth temperature for each layer were also considered.

$$\frac{1}{R}=\frac{6\sum_i E_i d_i\left(2\sum_{j<i} d_j+d_i\right)\sum_k E_k d_k\left[\sum_{l<i}(\alpha_{l+1}-\alpha_l)\Delta T_l-\sum_{l<k}(\alpha_{l+1}-\alpha_l)\Delta T_l\right]}{\sum_i E_i d_i\left[\sum_j E_j d_j^3+3\left(2\sum_{j<i} d_j+d_i\right)\sum_k E_k d_k\left(d_i-d_k+2\sum_{l<i} d_l-2\sum_{l<k} d_l\right)\right]} \quad (3.3)$$

$$(i,j,k,l=1,2,\ldots,N)$$

where, E_i, d_i, α_i, and ΔT_i are Young's modulus, thickness, coefficient of thermal expansion, and difference between room and growth temperature of the ith layer.

3.5.3 X-ray diffraction analysis

By detecting the slight changes in the interplanar spacing, the residual stress in thin film could be determined. Based on the definition of strain, it could be calculated by initial and changed lattice spacing, as shown in Eq. (3.4).

$$\varepsilon_z = \frac{d_l - d_{l0}}{d_{l0}} \tag{3.4}$$

where, d_l and d_{l0} stand for lattice spacing before and after fabrication process. As a result, the stress in the film could be calculated by Eq. (3.5).

$$\sigma_f = -\frac{E_f \left(d_l - d_{l0}\right)}{2\nu_f d_{l0}} \tag{3.5}$$

One advantage for X-ray diffraction analysis is that it can simultaneously evaluate the thermomechanical properties. For example, Zhou et al. proposed to establish the relationship between change of lattice spacing and temperature increase. The coefficient of thermal expansion could be derived based on Eq. (3.6).

$$\alpha = \frac{\Delta d_l}{\Delta T}\frac{1}{d_{l0}} \tag{3.6}$$

However, the X-ray diffraction analysis is more difficult to implement and it is only applicable to crystalline films.

3.5.4 Theoretical estimation

When a film/substrate structure experiences a change in temperature, different materials are going to expand or shrink by different amounts. By using the definition of thermal expansion and focusing on a two-layer structure, the thermal strain and stress can be quickly estimated by Eq. (3.7) and Eq. (3.8), respectively.

$$\varepsilon_{\text{th}} = (\alpha_{\text{f}} - \alpha_{\text{s}}) \cdot (T_{\text{Dep}} - T_{\text{Room}}) \tag{3.7}$$

$$\sigma_{\text{th}} = E_{\text{f}} \cdot \varepsilon_{\text{th}} = E_{\text{f}} \cdot (\alpha_{\text{f}} - \alpha_{\text{s}}) \cdot (T_{\text{Dep}} - T_{\text{Room}}) \tag{3.8}$$

where, α_{f} and α_{s} are the coefficient of thermal expansion (CTE) of film and substrate, T_{Dep} and T_{Room} are the temperature during fabrication and room temperature.

When the CTE of the film is smaller than that of the substrate, the film suffers from compressive stress. During the cooling process from higher fabrication temperature to room temperature, all layers tend to shrink due to temperature drop. The large CTE of the substrate makes it deform more severely than the film. As a result, the film with smaller deformation is compressed by the substrate. To the contrary, the film undergoes tensile stress when the CTE of the film is larger than that of the substrate. An illustration of film/substrate deformation under compressive or tensile stress is shown in Figure 2-23. Based on the above method, the stress in the multilayer structure present could also be estimated.

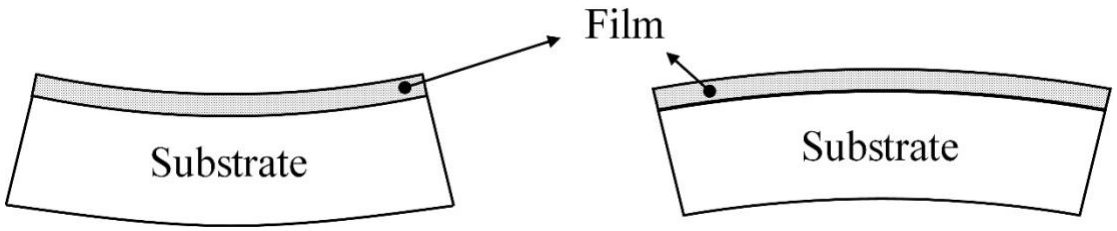

(a) Tensile stress (b) Compressive stress

Figure 2-23 Stress in thin films.

3.6 Device fabrication

3.6.1 Objective

In this section, we will introduce the process flow and details for the fabrication of the chemical sensors based on two identical metal nanowires. These nanowires should have a very

small feature (70 nm in width, 70 nm in thickness, and 3μm in length) with a very small gap between them (~50 nm). Nanowires are placed on a thin layer of silicon nitride to minimize the thermal effect by conduction. In addition, we added a trench to separate the emitter and detector from direct thermal conduction. To fabricate these nanophotonic emitters and detectors, we need a high-resolution patterning technique. We exploit the E-beam Lithography (EBL) system, ELS-G100 from Elionix, Japan. Standard contact lithography is used to pattern the electrode layer. Backside alignment and etching are performed to etch the substrate underneath the metal nanowires followed by a focused ion beam (FIB) to create a trench between the two nanowires.

The on-chip plasmonic sensor and emitter system is fabricated on the aforementioned substrate. Fig.3-1 shows the schematic of the device system, which is composed of two parts, the nano-scale sensor & emitter and micro-scale 4-probe electrodes, both made of Platinum (Pt) with a thin layer of titanium (Cr) underneath acting as an adhesion layer. Each of 4-probe electrodes is 200μm by 200μm square pads used for 4-point probe measurement of both the sensor & emitter. For sensor & emitter, the key part is the nanowire in the middle with the dimension of 70-nm wide, 70-nm thick, and 3-μm long. A 50-500nm wide trench would exist in between the sensor and emitter for studying the near-field thermal radiation.

3.6.2 Methodology and fabrication process flow

Fig. 3-24 shows the brief process flow for the fabrication of the nanophasmonic emitter and sensor. We can divide the whole process into 4 main different steps as i) patterning of metal nanowires, ii) patterning of electrodes, iii) backside etching, and iv) grooving a trench between the nanowires by FIB. In step i), we need a high-resolution patterning method to define the very small features of metal nanowires. EBL system ELS-G100 could offer down to 5nm feature, so we use this tool to achieve our 70nm wide metal nanowires. In step ii), standard contact UV lithography

was done to pattern the chromium (Cr) and gold (Au) electrode layer. Step iii) and iv) are the critical parts of our process to reduce the thermal conduction between the nanowires. In step iii), we conduct backside alignment and etch of the substrate. In step iv), a trench between the two nanowires is created by FIB.

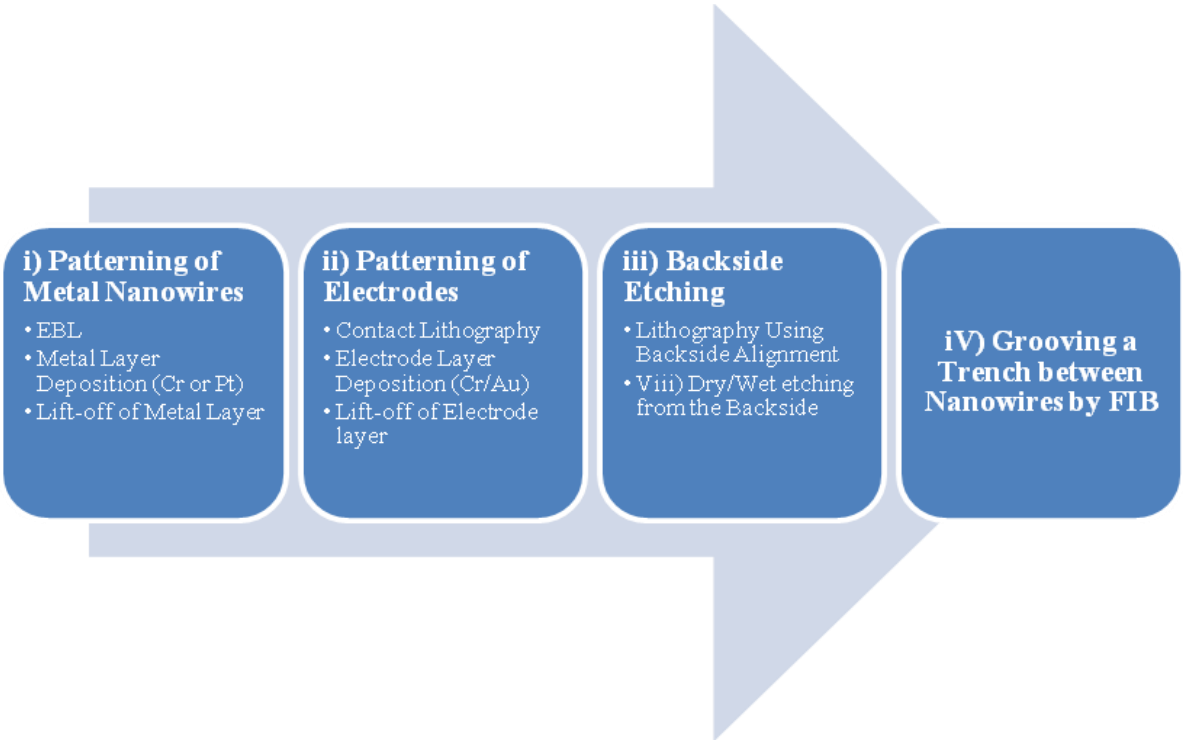

Figure 3-24 Fabrication process flow for the nanophotonic chemical sensor.

3.6.3 Fabrication challenges

We have many challenges during our fabrication process. The major challenges include i) hardening of photoresist when depositing Pt (platinum) for metal nanowires, ii) optimizing the backside etching, and iii) bending and warping of thin suspended film.

Pt is the best material for the metal nanowires due to its material properties. We use the e-beam evaporation method to deposit Pt for metal nanowires, but during the deposition, excessive heat hardens the resist and makes it hard for the lift-off process. Our approach is to

divide the deposition into several steps so that the resist layer would not heat up too much. If our target is 70 nm, we deposit 10 nm, then stop the deposition for 10 minutes to cool down the samples. Then, deposit another 10 nm and cool down again. Alternatively, we can use different metal (pure Cr) as nanowire material.

Metal nanowires should be suspended on the thin film to minimize the heat conduction through the substrate. At first, we try the Bosch process or deep reactive ion etching (DRIE) to etch all the substrate to make the metal nanowires suspended. However, the result is very uncontrollable and nonuniform, so we alternatively try silicon wet etching.

After we fabricate metal nanowires on the suspended film, the released structures would undergo bending of the film due to residual stresses. If the size of the suspended film is too wide, the distance between the nanowires would be much larger than the original design. We optimized the size of the suspended film with numerical simulation to minimize the effect due to the bending and warping of suspended structures.

3.6.4 Fabrication process flow

For this emitter and sensor system, the fabrication process sequence is critical for the stability of the device, fabrication cost, and testing. Fig. 3-25 shows the schematic of the fabrication flow. There are 4 steps included, the fabrication of sensor & emitter, fabrication of 4-probe electrode, back-side etching the hole and cutting the trench. We first pattern the sensor and emitter on the substrate via electron beam (e-beam) lithography and then align the 4-probe electrodes via photo-lithography correspondingly to ensure good contact. Then, the Bosch process is employed to etch a hole with the diameter of 50-100um from the back and finally a narrow trench would be etched via focused ion beam (FIB) to measure the near-field radiation.

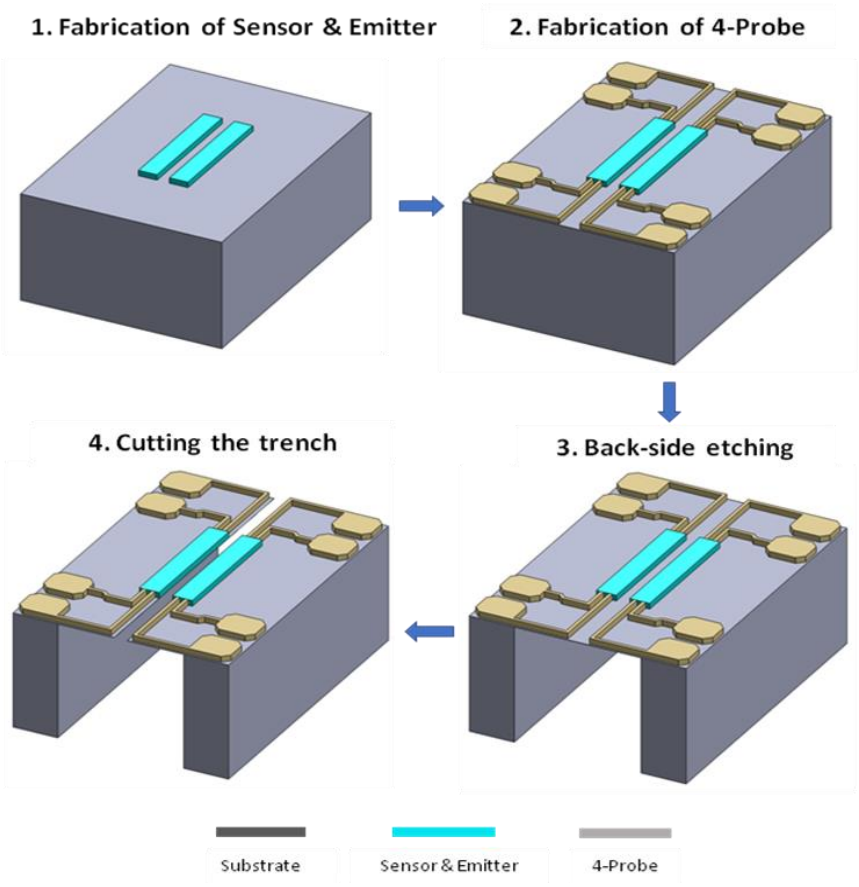

Figure 3-25 Schematic of fabrication flow of single on-chip photonic transducer.

(1) Substrate preparation (Fig. 3-26a)

4-inch <100> n-type 525-μm-thick silicon (Si) wafers with 300-nm-thick silicon nitride film on both sides were purchased from Silicon Valley Microelectronics, Inc., CA (Fig. 3-24a). Silicon nitride films were deposited by low-pressure chemical vapor deposition (LPCVD) to achieve tensile residue stress lower than 100MPa. The wafers were diced into 9mm by 9mm chips. Then the chips were immersed into acetone and cleaned by an ultrasonicator for 5 minutes. The chips were rinsed by acetone, isopropyl alcohol (IPA), and deionized (DI) water in serial order and blown by an air gun. Then the chips were dried on a hotplate at 115ºC for 1 minute.

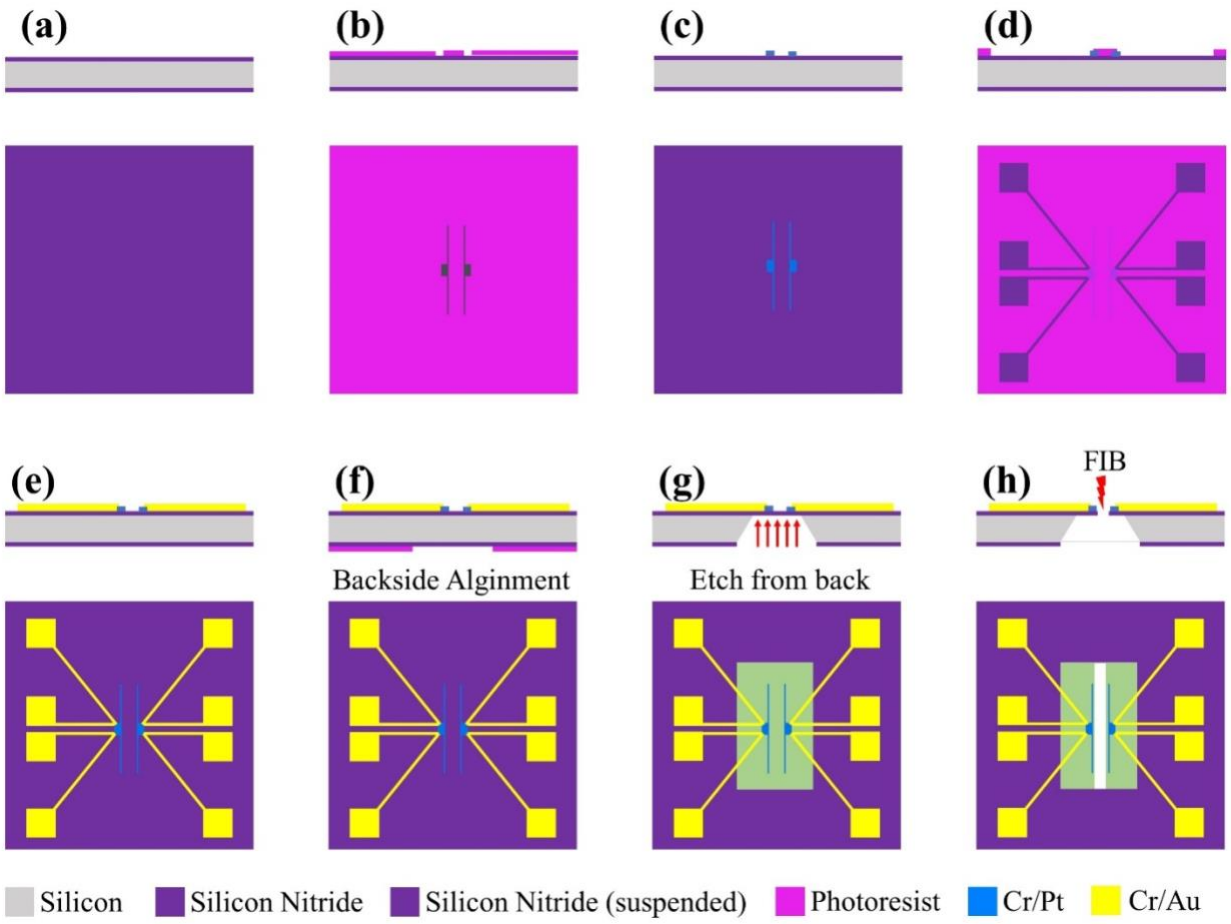

Figure 3-26 Fabrication Process Flow; (a) substrate preparation, dicing and cleaning, (b) E-beam lithography for metal nanowire patterning, (c) formation of metal nanowires by evaporation and lift-off, (d) UV lithography for electrode patterning, (e) E-beam evaporation of Cr/Au electrodes and following lift-off, (f) UV lithography from back of the substrate, (g) dry and wet etching from backside, (h) trench formation by focused ion beam.

(2) Patterning of metal nanowires (Fig. 3-26b, c)

Fig. 3-27 shows the fabrication flow of sensor & emitter. The sensor and emitter are first patterned on the pre-coated electron sensitive resist. Then the e-beam resist is chemically changed under exposure to the electrons, and the exposed areas can be dissolved during development. Therefore, the inverted pattern on the substrate would be obtained. Then we deposit 70-nm-thick

Pt layer on top of the device with a 10-nm thick Cr adhesion layer via e-beam evaporation. Furthermore, it is a cost-effective lift-off process where the material on top of the sacrificial layer would be removed easily by immersion and quick rinse with acetone. After lift-off process, the fabrication of sensor and emitter would be completed.

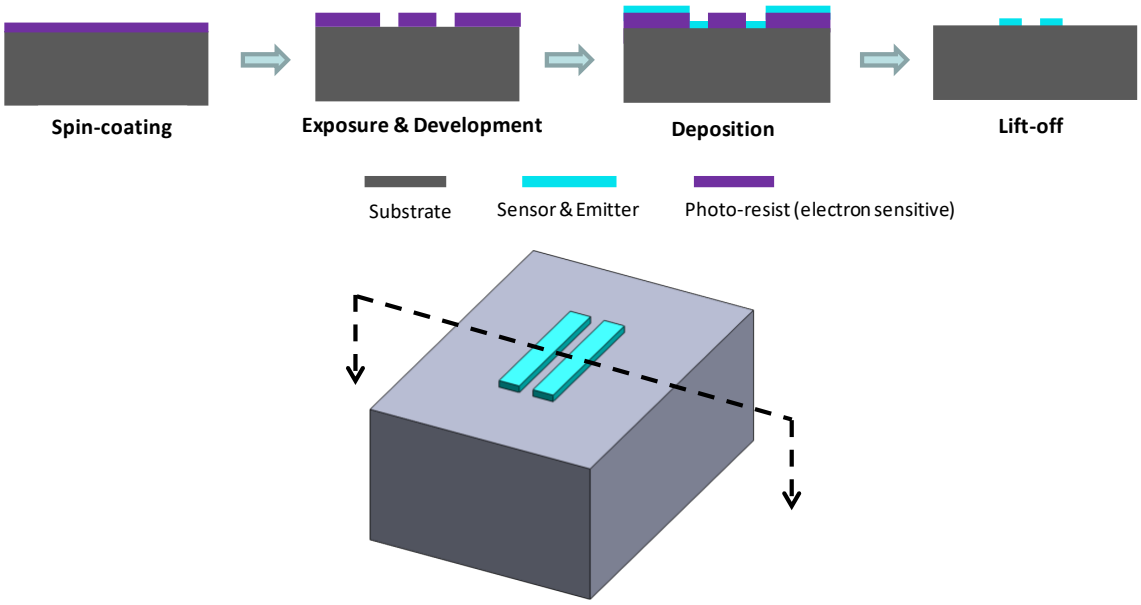

Figure 3-27 Fabrication flow of Sensor & Emitter.

A thin layer of PMMA A4 resist (Microchem Corp, USA) was spin-coated on the chips from 4.1 (600rpm 6sec + 4000rpm 60sec). Then the chips were baked on a hotplate at 180ºC for 2 minutes. ELS-G100 EBL system is used to expose the resist with the electron beam. Exposure dose of 1700μC/cm^2 was used for nanowire patterns and 1000μC/cm^2 is used for connection to electrodes. After the exposure, the PMMA layer is developed by immersing the chips in MIBK (Methyl isobutyl ketone) solution diluted in IPA (MIBK:IPA=1:3) for 1 minute, followed by subsequent rinsing with IPA for 20 seconds. Descumming of developed PMMA is done by O_2 plasma treatment using reactive ion etching (RIE) tool (10W, 10 mTorr, O_2 flowing at 20sccm, 15 seconds). Then, metal layers are deposited using an E-beam evaporation tool. Here, we had two

cases: (i) Cr/Pt nanowires or (ii) pure Cr nanowires. For (i) Cr/Pt nanowires, we successfully deposited 10nm Cr / 70nm Pt nanowires. Alternatively, we deposited pure 80 nm Cr layer to fabricate Cr nanowires instead of Cr/Pt nanowires. After finishing the E-beam evaporation, the chips are immersed in acetone overnight for the lift-off process.

Here are some experimental results about patterned nanowires. The original design is written by three different doses under E-beam lithography to minimize the proximity effect and also the connecting part of the two wires with the larger leads has a fan-shaped pad written by dose 2 as shown in Fig. 3-28. After running through analysis and proof of concept, we realize that, first only 2 doses could be used for writing, and second the fanned part would cause a large contact resistance. Therefore, we come up with the new design, where dose 3 is eliminated and also the connecting fanned pad is largely minimized to ensure the accuracy of the electrical measurement, as it is shown in Fig. 3-27.

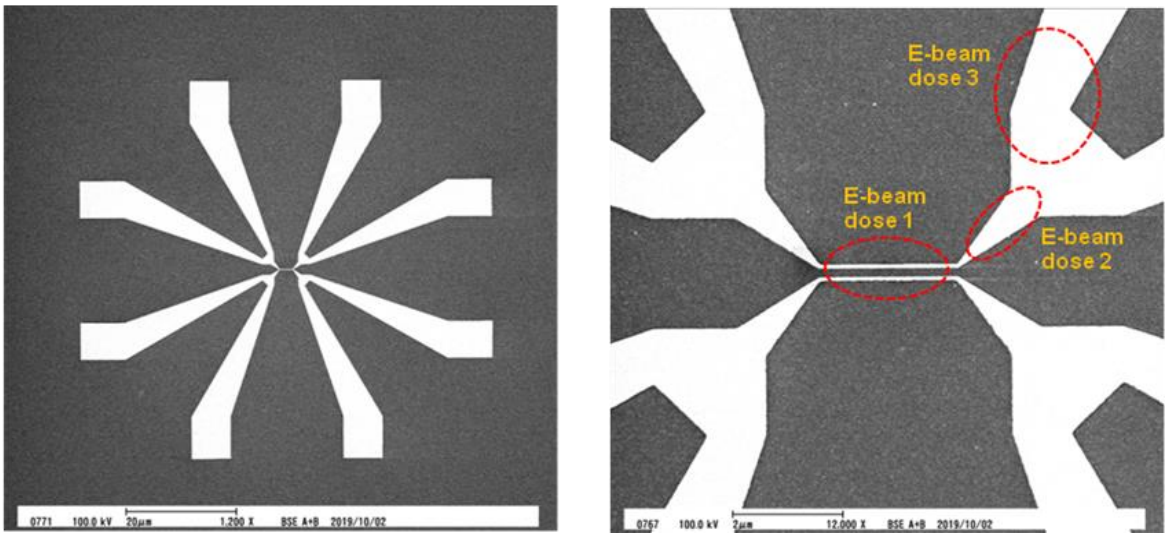

Figure 3-28 Original design of Sensor & Emitter.

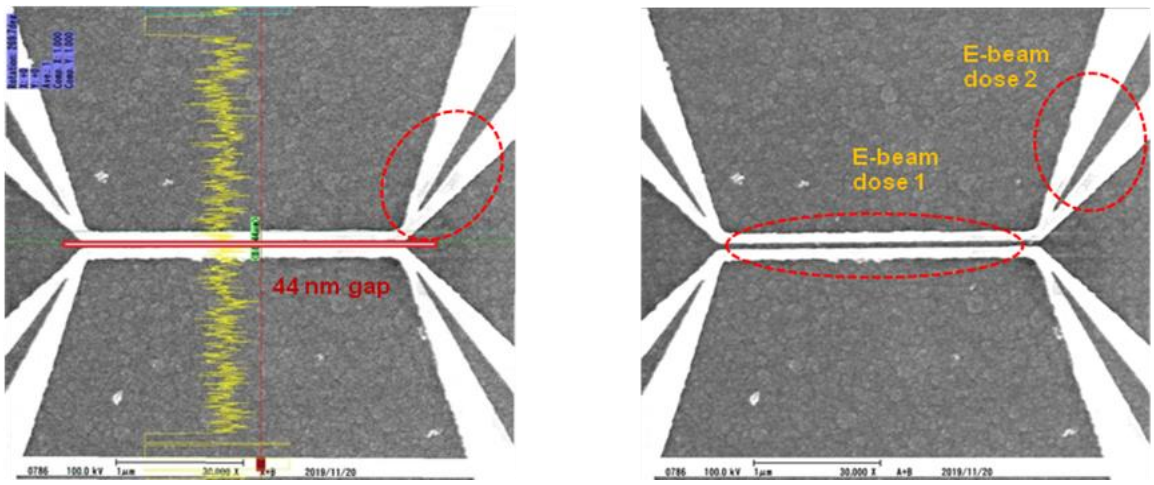

Figure 3-29 New design of Sensor & Emitter.

In addition, we tune the gap distance between the emitter and sensor by tuning the design gap and the writing dose and the results are promising showing we can control the gap 50nm and 100nm with 5nm tolerance as shown in Fig. 3-30.

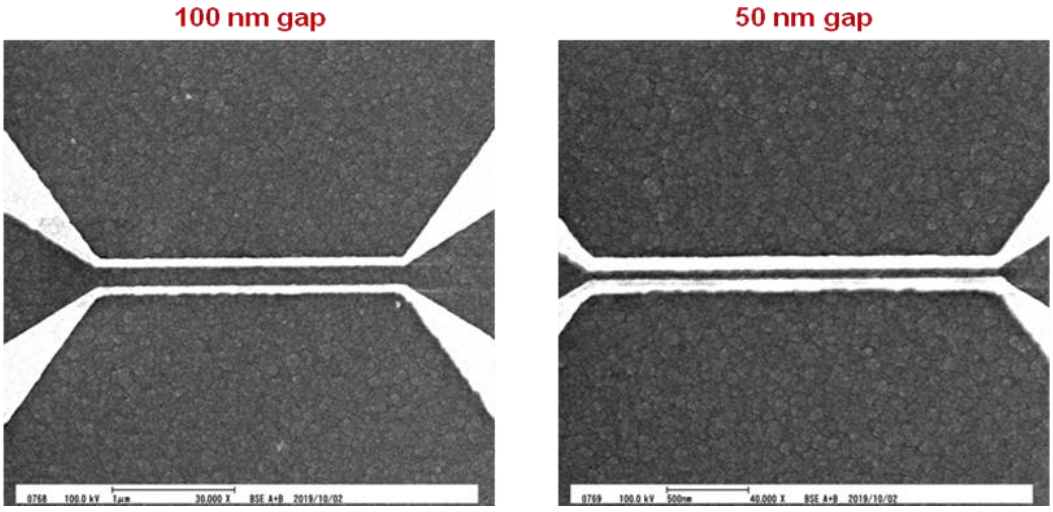

Figure 3-30 The gap between the emitter and sensor are 100nm and 50nm.

Moreover, in order to get the most resonance from the two nanowires, we extrude the two wires from the separate heating parts on each side as shown in Fig. 3-31. This would increase the resonant modes of both nanowires tremendously;herefore, the near-field emission signal would be

largely enhanced as opposed to all the previous designs. As for the previous design, the nanowires are directly connected to the electrodes, which would contribute to the current charge leakage to a certain extent. Therefore, we finalize our design as shown in Fig. 3-31.

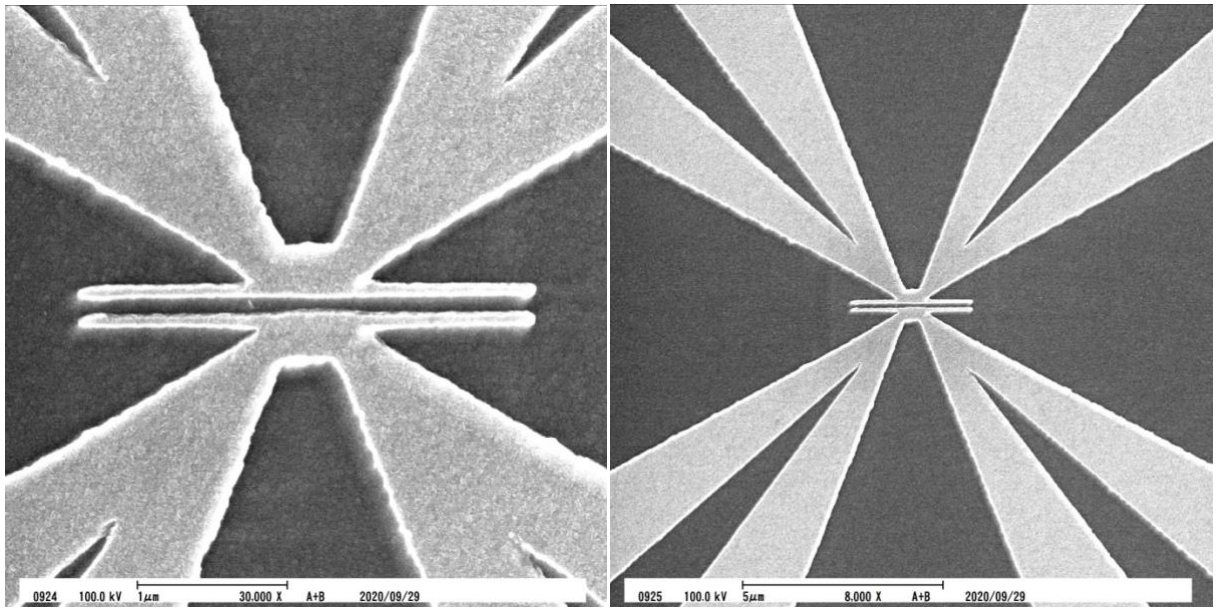

Figure 3-31 Extruded nanoplamonic structures for enhanced thermal resonance.

(3) Fabrication of 4-probe electrodes via photolithography and lift-off (Fig. 3-26d, e)

Fig. 3-32 shows the fabrication flow of the micro-scale 4-probe electrode using photo-lithography, e-beam evaporation and lift-off. Quite similar to the previous step, except that we use optical instead of e-beam lithography for micro-scale patterning, a uniform layer of ultra-violet (UV) sensitive resist is then coated on the wafer by spin-coating. Subsequent exposure and development are used to remove the irradiated region of photo-resist, and we obtain the micro-scale 4-probe pattern. Pt and Cr are deposited via e-beam evaporation and the lift-off process is employed to obtain the 4-probe electrodes.

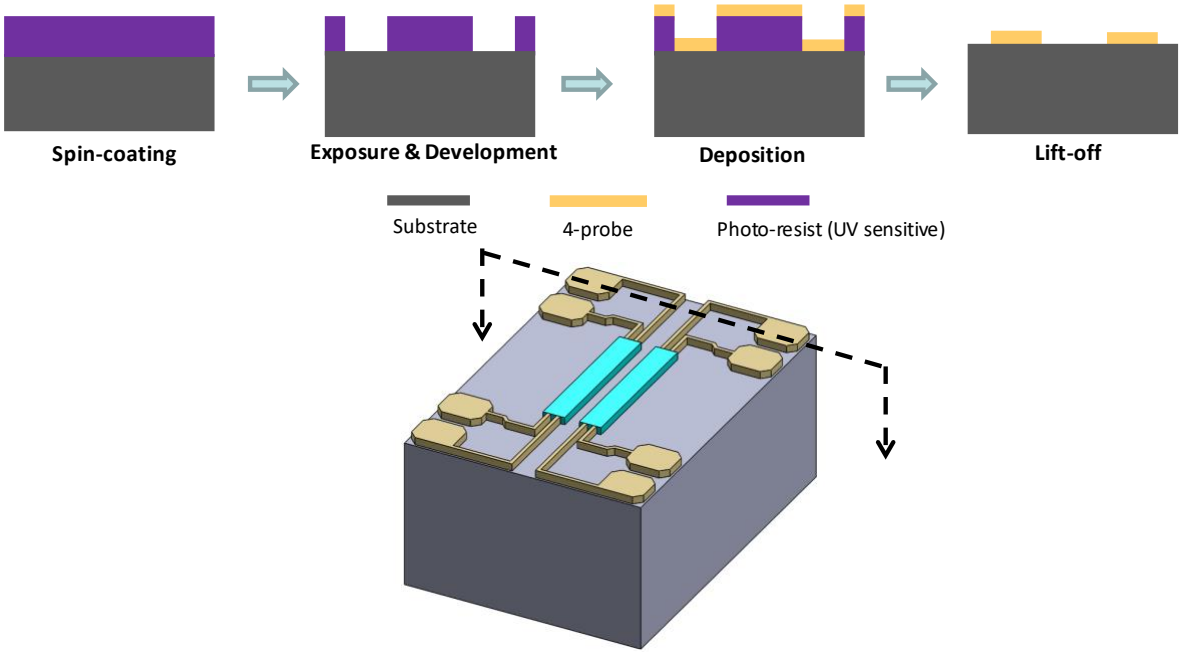

Figure 3-32 Fabrication flow of the 4-probe electrode.

The chips were strongly sonicated in an ultrasonicator with 170 kHz frequency for 10 minutes. Chips were subsequently rinsed with acetone and IPA. For dehydration, the chips were dried on a hotplate at 115ºC for 1 minute. HMDS (hexamethyldisilazane) layer was coated on the chips by HMDS vapor open. AZ P4110 (Microchemicals GMBH, Germany) photoresist was spin-coated on the chips (600rpm 6sec + 4000 rpm 60sec). Then the chips were baked on a hotplate at 95ºC for 2 minutes. The chips were exposed to UV (ultraviolet) light using a contact aligner (5W/cm^2, 60 sec). After the exposure, the photoresist layer was developed by immersing the chips in diluted AZ 400K (Microchemicals GMBH, Germany) solution (AZ 400K : DI water = 1 : 3) for 1 minute with strong agitation. The photoresist layer was treated with O_2 plasma for the descumming process (100W, O_2 flowing at 20sccm, 2 minutes). Then, Cr/Au layers were deposited using the E-beam evaporation tool (15nm Cr / 200nm Au). After finishing the E-beam evaporation, the chips were immersed in acetone overnight for the lift-off process. Fig. 3-33 shows the design schematic and optical images of the 4-probe electrode under the microscope.

Here are the results of the micro-scale 4-probe patterned with the emitter and sensor system in Fig. 3-34. We can see from the SEM image that the alignment of the emitter and sensor with the 4-probe is well-connected, which can guarantee the electrical stability for testing.

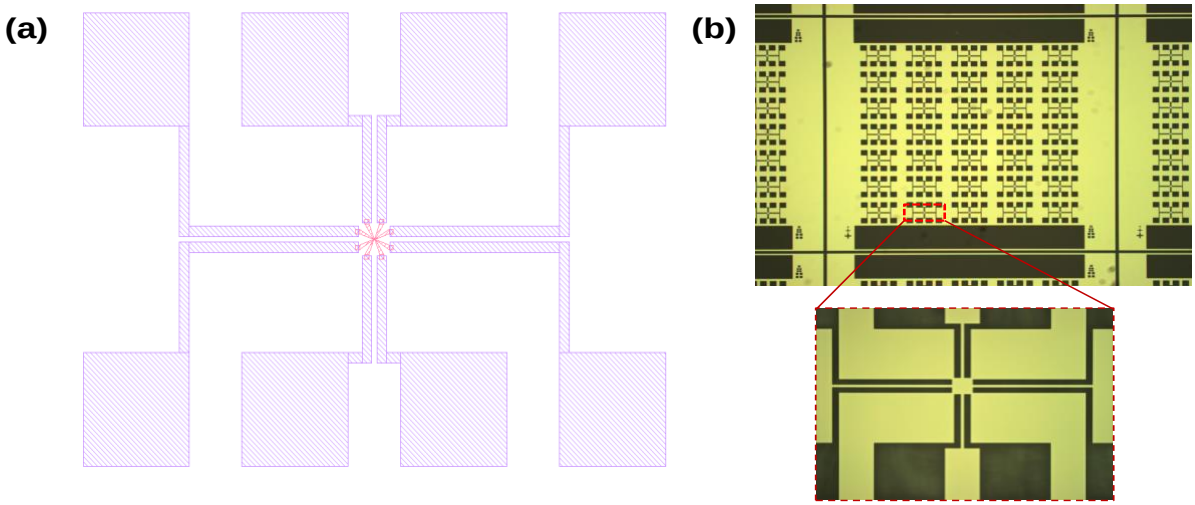

Figure 3-33 Design schematic and optical images of the 4-probe electrode.

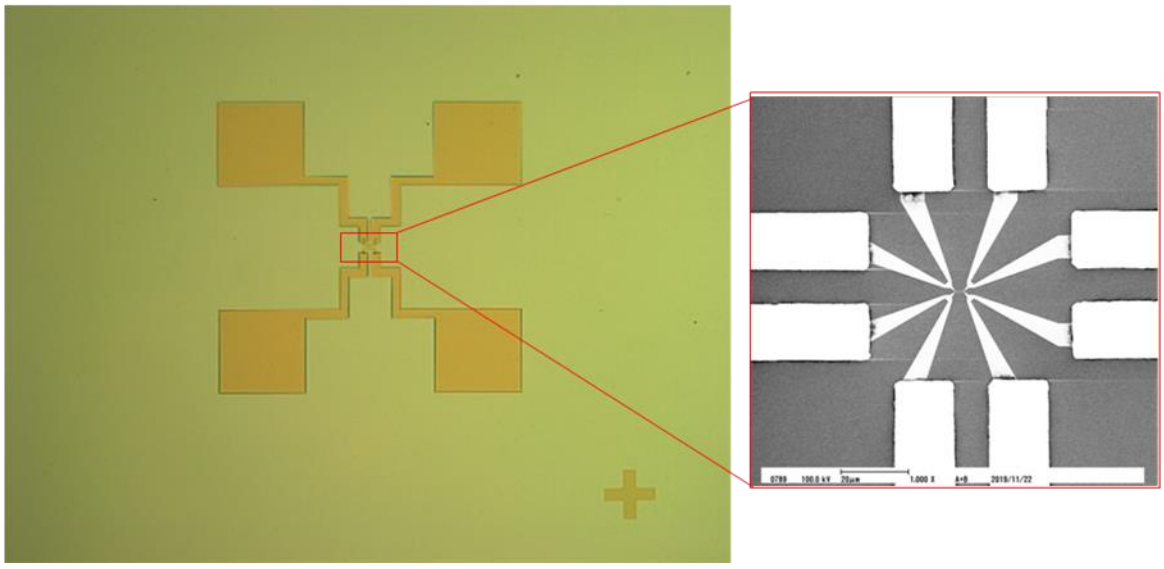

Figure 3-34 Optical and SEM images of emitter & sensor with the 4-probe electrode.

(4) Backside etching (Fig. 3-26f, g)

The chips are strongly sonicated in an ultrasonicator with 170 kHz frequency for 10 minutes. Chips are subsequently rinsed with acetone and IPA. For dehydration, the chips are dried on a hotplate at 115ºC for 1 minute. First, the device side of the chips where nanowires are presented is spin-coated with PMMA A4 resist. Then the chips are baked on a hotplate at 180ºC for 1 minute. After that, we coat the other side of the chips with HMDS (hexamethyldisilazane) layer by HMDS vapor open. The chips are spin-coated with AZ P4110 with the same recipe from 4.3. Instead of baking on a hotplate, we use a convection oven at 90ºC to bake the AZ P4110 photoresist layer (5 minutes). After the baking, the same exposure and development conditions as 4.3 are used. To etch the 300-nm-thick silicon nitride layer, we use RIE with CF4 and CHF3 mixed gases (CF4 flowing at 14 sccm, CHF3 flowing at 6 sccm, pressure at 10 mTorr, 25W, 38 minutes). Then, the chips are immersed in acetone and sonicated for cleaning. One hundred-nm-thick copper (Cu) layer is deposited on the front (device) side as a protection layer during the wet etching. Thirty wt% potassium hydroxide (KOH) solution is prepared for wet etching of Si substrate layer under the silicon nitride and metal nanowires. The chips are immersed in KOH solution at 100ºC for two hours to etch 525 μm of Si layer all the way through. To remove the Cu protection layer, the chips were immersed in Cu etchant APS-100 (Transene inc., USA) for 1 minute. Finally, a critical point dryer is used to release the suspended silicon nitride film without the failure of the structures.

Here are the results of the micro-scale 4-probe patterned with the emitter and sensor system in Fig. 3-35. We can see from the optical image that the alignment of the emitter and sensor with the 4-probe is well-connected which can guarantee the electrical stability for testing.

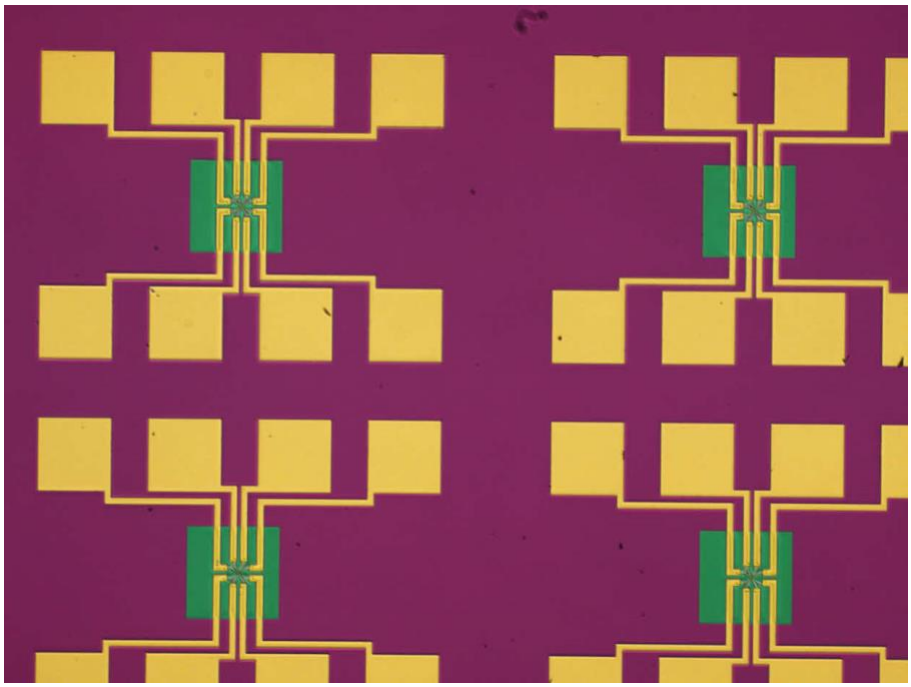

Figure 3-35 Nanoplasmonic devices after KOH wet etching.

According to the modified design, we'd like to control the distance of the emitter 16-23μm away from the edge of the etched opening. After modifying our mask design and alignment, we are able to achieve this fine adjustment as shown below in Fig. 3-36,

Figure 3-36 Nanoplasmonic devices after modified KOH wet etching.

(5) Focused ion beam (FIB) milling

FIB tool could achieve sub-100 nm width trenches by cutting the silicon nitride film between two metal nanowires. Then, the chips were wire-bonded on chip carriers for the measurement.

As we demonstrate, FIB is quite flexible and accurate at making such a narrow trench with high aspect-ratio compared to reactive ion etching (RIE). The reason is because in order to use RIE, multiple extra steps must be added to make the hard mask for etching and the process would be complicated and cost-prohibitive. Furthermore, the alignment of sensor and emitter with the trench must be challenging as well via RIE.

Lastly, FIB would be used to etch against the gap in between the sensor and emitter.

First, we use bare Si wafer as a proof of concept and the result is shown in Fig. 3-37. It is easy to cut a high aspect ratio trench with a smaller width on Si and the aspect ratio could be as high as 10.

However, when we do FIB milling on the designed substrate with the SiNx on top, it seems quite difficult to cut a high aspect ratio trench because of a low sputtering yield of SiNx compared to single crystalline silicon. Here are some results regarding cutting the trench through SiNx thin film as shown in Fig. 3-38. In addition, as the simulation results show, we only need to cut the trench in between the shorter nanowires, but a 250-300μm long trench is expected to cut through the SiNx film to avoid the heat conduction interference for the measurement.

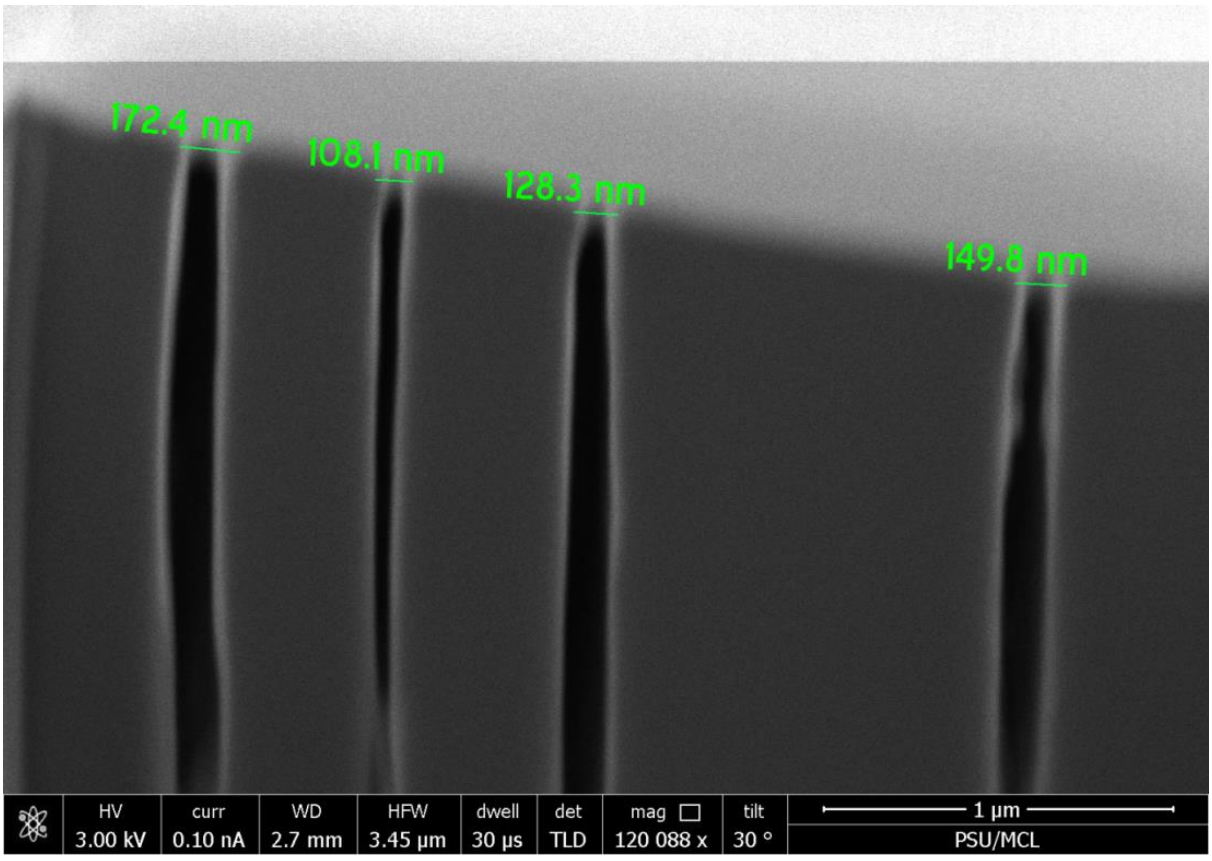

Figure 3-37 SEM image of the etching result from FIB milling silicon.

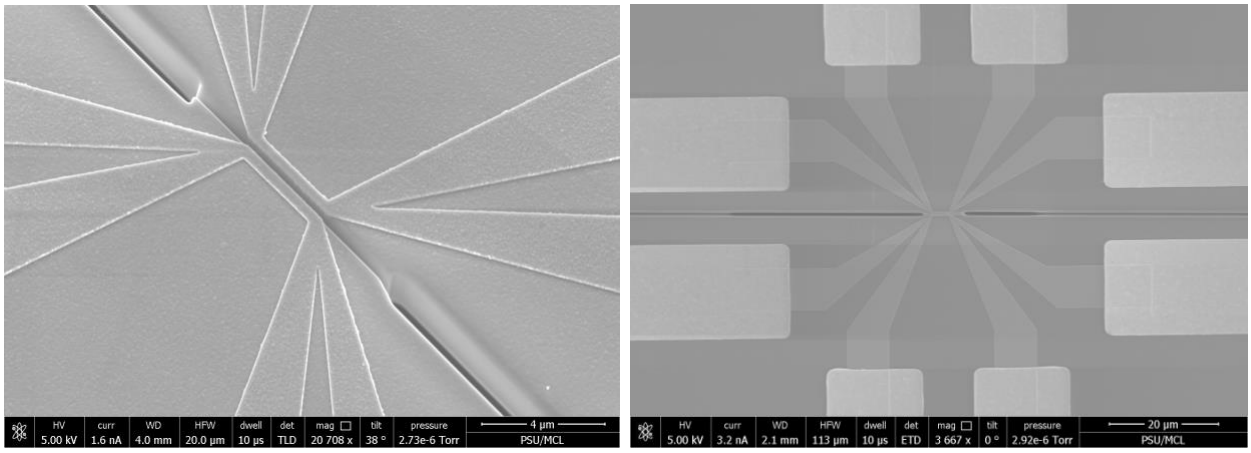

Figure 3-38 SEM image of the etching result from FIB milling SiNx.

3.6.5 Device testing and wire bonding

Based on the fabricated plasmonic emitter and sensor above, we will test their chemical sensing performance by conducting detailed characterizations thermally and optically. Our goal is to demonstrate we have the capability to measure an ultra-small near-field thermal radiation signal at the nano-scale. Therefore, we wire bond the device pad with the pads on the DIP package as shown in Fig. 3-39.

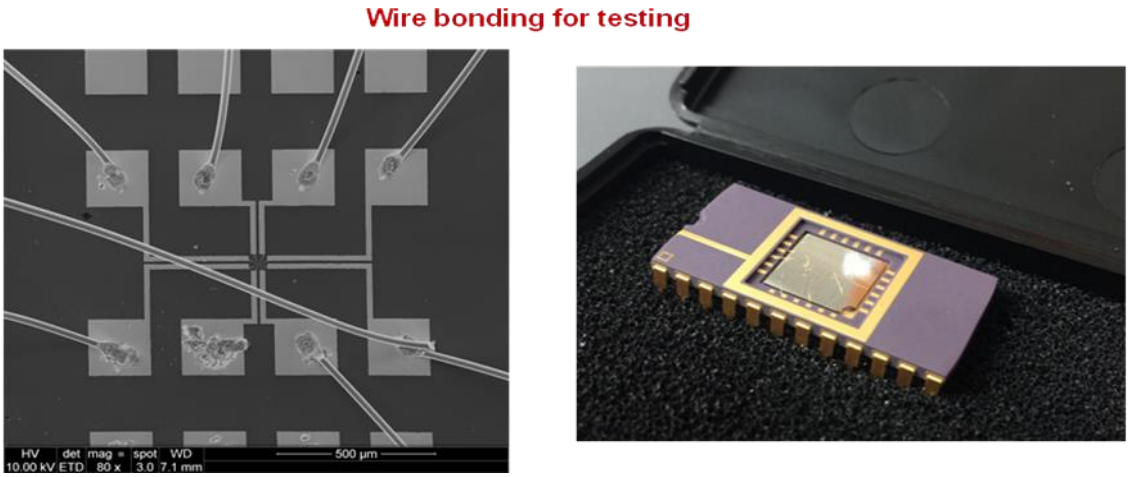

Figure 3-39 Images of the wire-bonded device and the DIP package for testing.

3.7 Thermal characterization

3.7.1 Mechanism of thermal measurement

Suspended device was first proposed by Prof. Li Shi [88] to measure the thermal conductivity of silicon nanowire in 2003. The structure is well-known for high sensitivity and straightforward heat transfer model. Such device design has been widely used to measure the thermal conductivity of nanowire [89] and nanoribbon [90], and even expanded to measure far field radiation [91, 92]. Currently steady-state heating plus high-sensitivity Wheatstone bridge is used in the Shen Lab.

3.7.2 Theory and method

Here, we use another thermal device to demonstrate the methodology of our thermal measurement. As shown in Fig. 3-40, the device is a 2mm × 2mm square chip with four pairs of suspended pads. Each pad is supported by seven 400-μm-long thin silicon nitride beams. Pt coil is deposited on the pad in serpentine shape for uniform heating and temperature sensing. Each supporting beam is linked to an electrode.

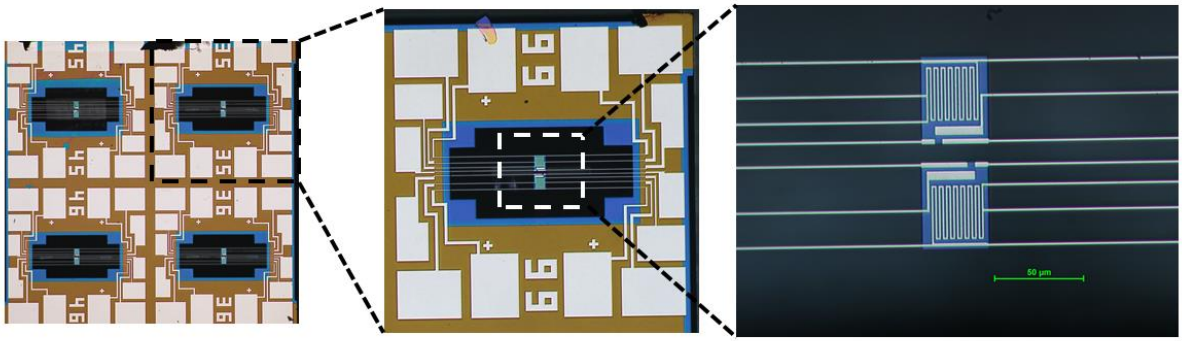

Figure 3-40 Photo of suspended thermal device.

As shown in Fig. 3-41, the nanowire sample is mounted on the device bridging the two pads. One of the pads is heated by a DC current, named heating pad. The temperature of the other pad, sensing pad, is monitored. With the help of high vacuum and radiation shield, thermal conduction is dominant, and the temperature of sensing pad is determined by how much heat is transported from the heating pad to the sensing pad via the sample. Therefore, the thermal conductivity of the sample can be determined by measuring the temperature of the heating pad T_h and sensing pad T_s using resistive thermometry.

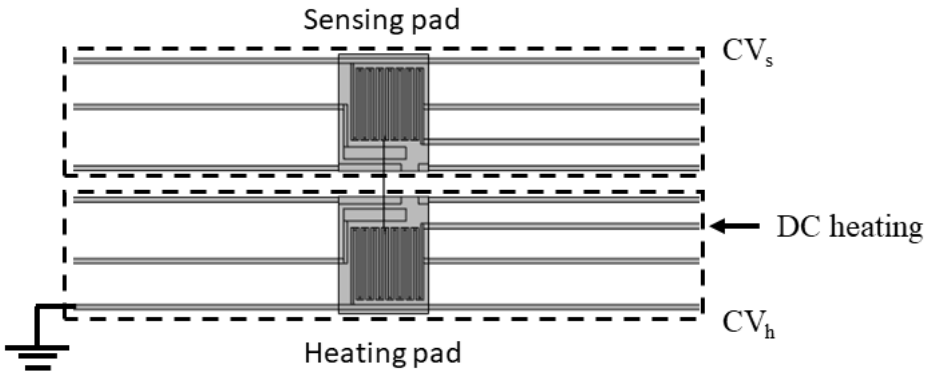

Figure 3-41 Demonstration of thermal conductivity measurement based on the suspended device.

Consider the temperature distribution of the device. Note that the surface of the pads and supporting beams is adiabatic. Temperature is uniformly distributed on the pads, linearly distributed on the non-heating supporting beams, and parabolically distributed on the heated supporting beams, respectively, as shown in Fig. 3-42.

Figure 3-42 Finite element simulation result of temperature distribution

As shown in Fig. 3-41, energy conservation about control volume about sensing pad CV$_s$ is indicated by Eq. (3.9),

$$Q_s = G_s(\Delta T_h - \Delta T_s) = G_b \Delta T_s \tag{3.9}$$

where Q_s is heat flow via the nanowire sample, G_s is thermal conductance of the sample, $G_b = 7k_bA_c/L_b$ is the thermal conductance of all supporting beams of the sensing pad, and ΔT_h and ΔT_s

are the temperature increases of heating pad and sensing pad about the ambient temperature, respectively.

Energy conservation about control volume about heating pad CV_h indicates as Eq. (3.10),

$$Q_h + 2Q_b = Q_s + Q_{nhb} + Q_{hb} \tag{3.10}$$

where $Q_h = I^2 R_h$ is the heat generation on the heating pad, $Q_b = I^2 R_b$ is the heat generation on a single heated supporting beam, $Q_{nhb} = 5G_b \Delta T_h/7$ is the heat dissipated by the non-heating supporting beams, and $Q_{hb} = 2(G_b \Delta T_h/7 + Q_b/2)$ is the heat dissipated by the heated supporting beams.

Solving the energy conservation equations (Eq. (3.11) and (3.12)) indicates that

$$G_b = \frac{Q_h + Q_b}{\Delta T_h + \Delta T_s} \tag{3.11}$$

$$G_s = G_b \frac{\Delta T_s}{\Delta T_h - \Delta T_s} \tag{3.12}$$

The temperature of the heating pad and sensing pad is determined by resistive thermometry by Eq. (3.13), where *dR*/*dT* is determined by TCR calibration measurement.

$$\Delta T = \frac{\Delta R}{dR/dT} \tag{3.13}$$

3.7.3 TCR calibration measurement

Temperature coefficient of resistance (TCR) is a fundamental parameter for thermometry, defined by Eq. (3.14),

$$\alpha = \frac{1}{R_{ref}} \frac{dR}{dT} \tag{3.14}$$

where Rref is the resistance at reference temperature such as Eq. (3.15),

$$R = R_{ref}\left[1 + \alpha\left(T - T_{ref}\right)\right] \tag{3.15}$$

The TCR measurement circuit used in Shen lab is shown in Fig. 3-43a. The internal AC voltage source of the lock-in amplifier is converted to a current source with the 10MΩ resistor. The typical sensing current used for resistance measurement is 100~400nA. Four-probe connection is applied to a serpentine coil, and the voltage across the serpentine coil is measured by lock-in amplifier. The resistance of the serpentine is then determined by voltage divided by the current of the current source. The relation between temperature and resistance is then determined by varying the ambient temperature of the cryostat. A typical measurement result of the suspended device is shown in Fig. 3-42b. Generally, metal shows a quasi-linear temperature-resistance relation. First, 2nd, and 3rd degree polynomials could be used for curve fitting and calculation of TCR. Even for the same type of material, the TCR value varies with material microstructure under different fabrication process, and material dimension if size effect occurs.

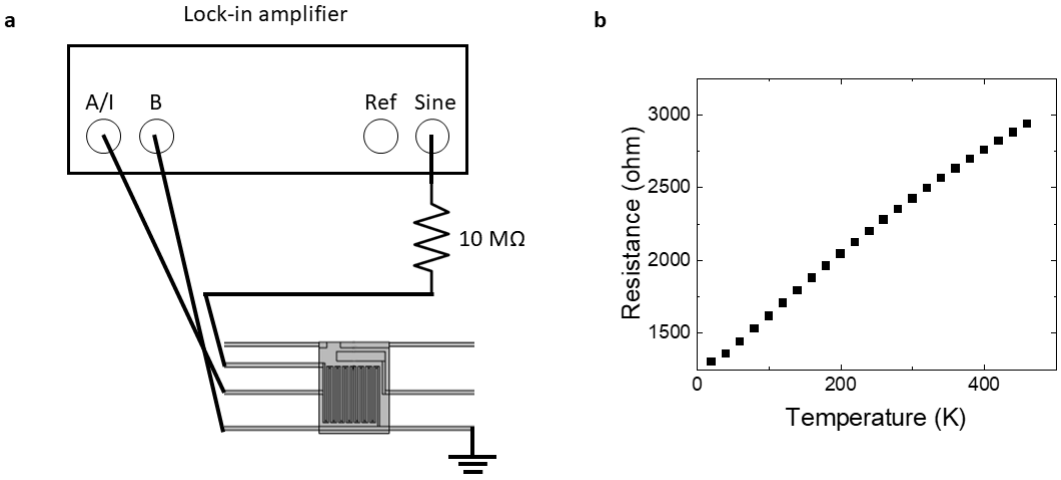

Figure 3-43 (a) Four-probe circuit for TCR measurement. (b) Typical resistance-temperature relation of the platinum coil.

3.7.4 Frequency calibration measurement

The AC sensing current could couple with DC heating current and induce additional heating to the heating pad, if the frequency of sensing current is so low that the pad temperature is able to respond to the modulated heating. Thus, a frequency calibration measurement is required for the heating pad. The circuit connection is the same as that shown in the Fig. 3-43a except an additional DC source plugged in with the AC sensing current. Calibration measurement is implemented as shown in the pseudocode below:

For AC frequency = 1 ~ 2000 Hz

For DC heating I = 0 ~ 1.5mA

Record ΔT_h at I_{max}

End

End

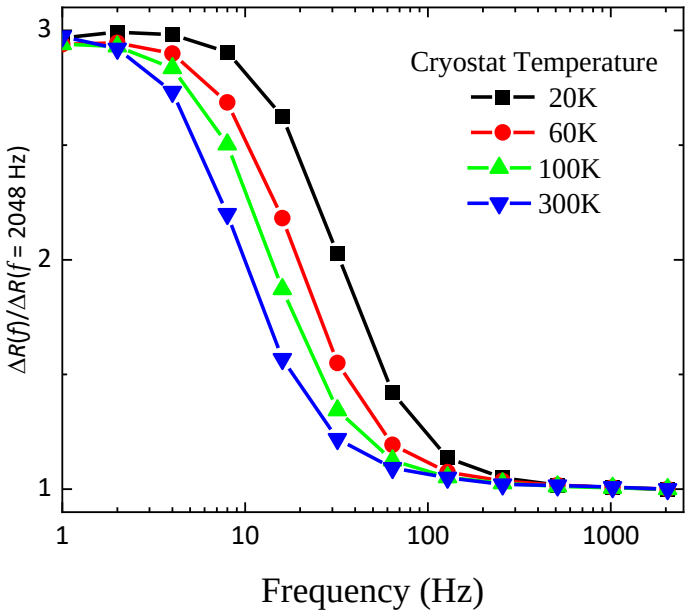

Figure 3-44 Frequency calibration of heating pad.

A typical calibration result is shown in Fig. 3-44. Specifically, the temperature increase of heating pad can be calculated by Eq. (3.16),

$$\Delta T = \begin{cases} \frac{3\Delta R}{dR/dT}, if\ f \ll 1/2\pi\tau \\ \frac{\Delta R}{dR/dT}, if\ f \gg 1/2\pi\tau \end{cases} \quad (3.16)$$

3.7.5 Four-probe thermal measurement

As mentioned, the principle of the measurement is to heat up the heating pad and then monitor the temperature of the sensing pad. The temperatures of the sensing pad and heating pad are independently monitored by two lock-in amplifiers in the four-probe circuit, as shown in Fig 3-45.

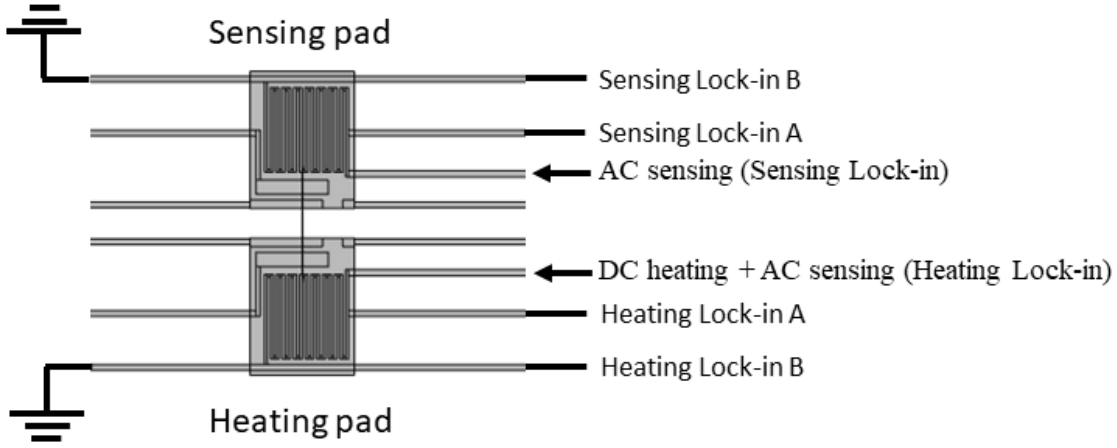

Figure 3-45 Schematic of four-probe measurement circuit

3.7.6 Wheatstone thermal measurement

Higher sensitivity of measurement requires the circuit to detect the change in the sensing pad as sensitively as possible. Therefore, four-probe circuit for the sensing pad is replaced by Wheatstone circuit, as shown in Fig. 3-46. Wheatstone bridge circuit shows much higher

sensitivity thanks to its differential circuit nature. Besides, the noise induced by temperature fluctuation is suppressed because the sensing pad and the reference pad are both within the cryostat such that the temperature fluctuation is identical. The gap voltage V_g of the Wheatstone bridge is monitored by lock-in amplifier. The resistance of the sensing pad is determined by Eq. (3.17),

$$R_s = \frac{R_4}{\left(\frac{V_g}{V_s} + \frac{R_3}{R_2+R_3}\right)} - R_4 \tag{3.17}$$

where V_s is the source voltage to power the Wheatstone circuit, which typically is 0.02 V for the suspended device. Note that there is no 10MΩ resistor used here.

Specifically, the R_s measured here is the total resistance of the serpentine coil and two supporting beams. Considering the temperature distribution, resistance increase during measurement is connected to temperature increase of the sensing pad by Eq. (3.18),

$$\Delta R_s = \left(\frac{dR_b}{dT} + \frac{dR_c}{dT}\right)\Delta T_s \tag{3.18}$$

where R_b and R_c are the resistances of a single supporting beam and serpentine coil, respectively. With TCR determined by measuring R_s, Renkun Chen *et al*[5] suggested that one should use effective resistance increase for the temperature calculation according to Eq. (3.19),

$$\Delta T_s = \frac{\Delta R_{s,eff}}{dR_s/dT} = \frac{\Delta R_s}{dR_s/dT}\left(\frac{R_b+R_c}{2R_b+R_c}\right) \tag{3.19}$$

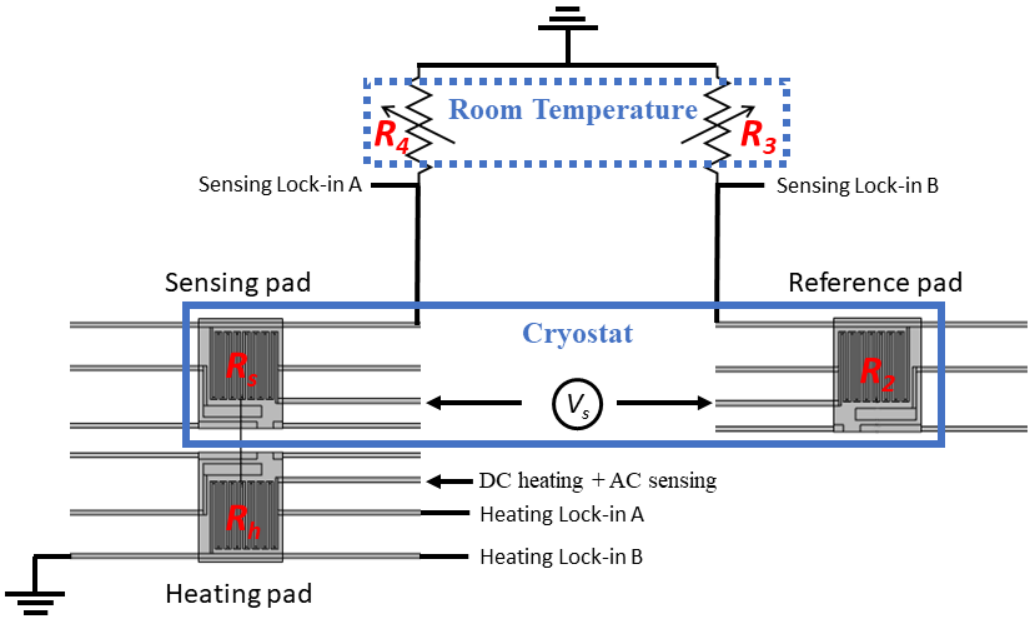

Figure 3-46 Schematic of Wheatstone measurement circuit.

3.7.7 Measurement preparation

(1) Chip mounting

DIP Chip carrier with 24 leads is used for the measurement. There are electrodes on the top surface of the chip carrier, which are to be linked with the suspended device by wire binding. The leads of the chip carrier are to be plugged in the sockets on the measurement stage in connection with the external wire box. The chip mounting procedure is

- Rinse the chip carrier with acetone and IPA to remove the amorphous silicon.
- Trim the protection metal belt to release the leads.
- Mix the thermal epoxy on a piece of glass slide with the glass pipette.
- Attach a tiny piece of mixed but uncured thermal epoxy on the DIP chip.
- Put the device on the DIP chip carrier.

- Use tweezers to push the DIP chip carrier until one corner of the device adheres to the thermal epoxy. Make sure the suspended device is horizontally placed for better accessibility of wire bonding.

(2) Wire bonding

Fig. 3-37 has shown the wire-bonded device after packaging. Westbound manual wedge bonder is used for wire bonding. The aluminum/silicon alloy wire shows high flexibility and low resistivity. The bounded wire should start from the DIP chip carrier and end at the electrode of the suspended device. Bond the wires clockwise or anticlockwise such that the bonded wires would not hinder further bonding.

(3) ESD protection

Electrostatic discharge could potentially burn out the device and is especially active during winter. ESD protection should be implemented once wire bonding begins. ESD protection procedures include,

- Use anti-static conductive foam and ESD protection box for storage.
- Wear anti-static wristband and anti-static finger glove or gloves when handling.
- Use anti-static floor mat. Wear anti-static shoes.
- Turn on static eliminator fan when handling.
- Use air humidifier to increase the air humidity of the lab. Relative humidity greater than 35% is favored.

An overview of ESD protection tools is shown in Fig. 3-47.

anti-static floor mat

static eliminator fan

Conductive foam and ESD protection box

anti-static gloves

anti-static finger gloves

anti-static wristband

Fig. 3-47 An overview of ESD protection tools.

3.7.8 Measurement procedures and the cryostat system

Electrostatic discharge could potentially damage our device. The measurement procedures include sample loading/unloading, wire connection, cryostat operation and MATLAB code running. Wire connection has been shown previously. Readers are suggested to also refer to the Scott Hall Cryostat operating procedure written by Dr. Pengfei Li, Dr. Phil Smith, et al, for information about cryostat operation. The MATLAB codes are presented here by pseudocode. Readers are also suggested to refer to the diagram written by Mr. Devarsh Vispute for information about the algorithm of the MATLAB codes.

The cryostat setup is shown in Fig. 3-48. The cryostat chamber is maintained at high vacuum by the vacuum pump. The cryostat of temperature is controlled by a Lakeshore 335 temperature controller with an electric heater and a closed-loop liquid helium cooling cycle. The

cryostat temperature can be finely fixed at any temperature from 10K to 470K with 0.01K resolution. The DIP chip sockets are at the top of chamber, which are connected to an external wire box. The links among DIP chip, sockets and wire box are shown in Fig. 3-49.

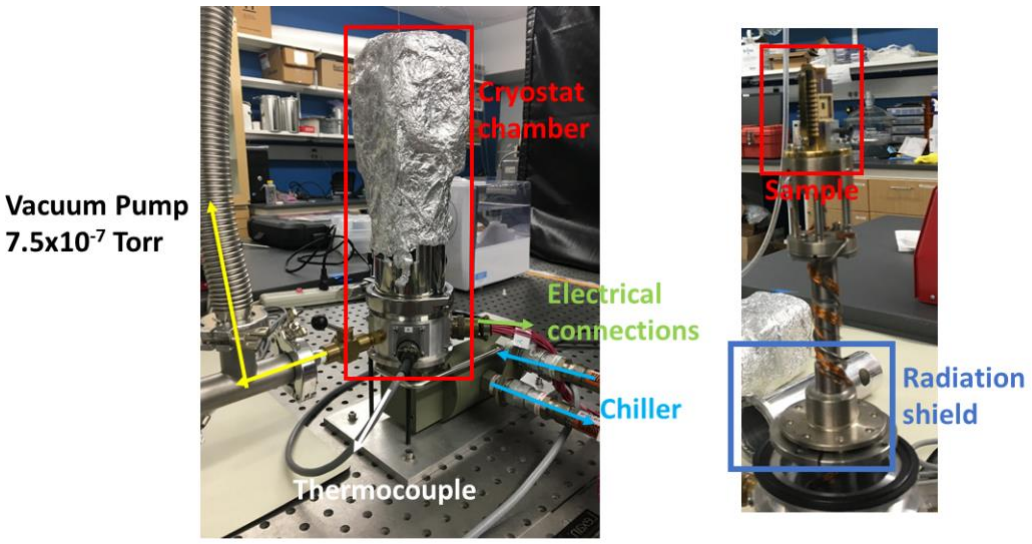

Figure 3-48 Picture of cryostat setup.

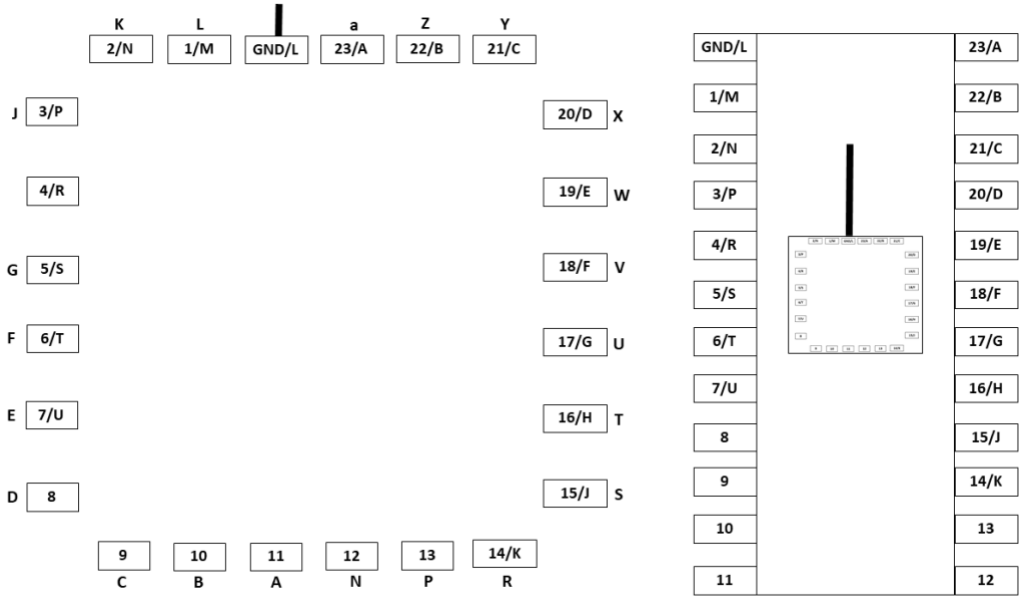

Figure 3-49 Links among DIP chip, sockets, and wire box. The outer and inner circles indicate the links of the HH cryostat and Scott Hall cryostat, respectively.

3.7.9 Thermal measurement results

The SEM picture and schematic of the nanowire are shown in Fig. 3-50a and b, respectively. Both nanowires are connected in four-probe circuit. The dimensions of the nanowire are L × W × t: 3μm × 250nm × 50nm.

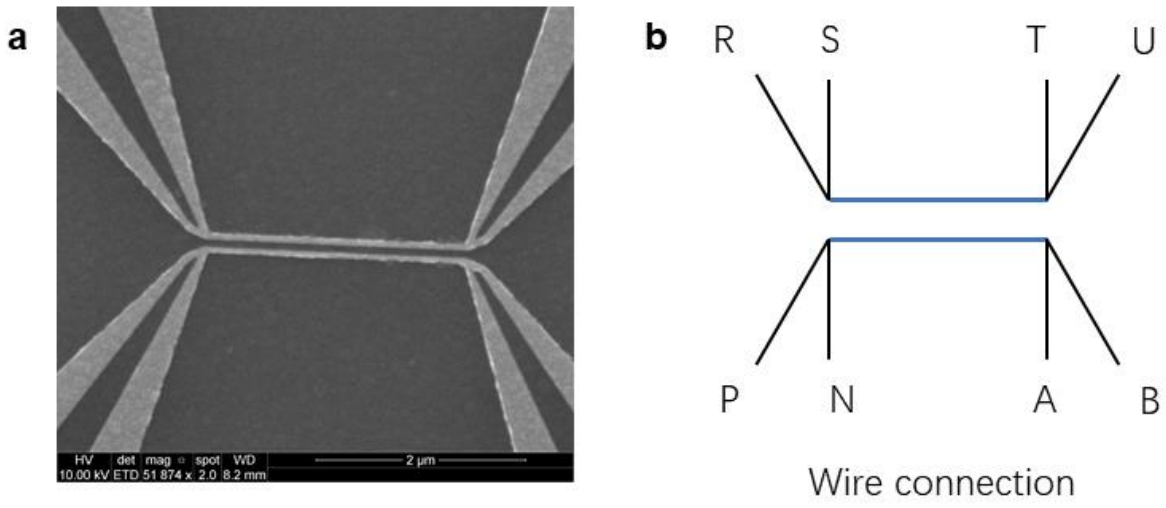

Figure 3-50a The SEM image of the nanoplasmonic structures b Schematic and wire-bonding connection of the nanowire

Firstly, the temperature-resistance relation is calibrated by varying cryostat temperature and measuring the resistance of the nanowire using lock in amplifier. Four measurements are applied as shown in the Table 3-11. The temperature-resistance relation of emitter RSTU and detector PNAB are shown in Fig. 3-51a and b, respectively. The resistance of nanowire decreases with temperature, opposite to the general trend of bulk metal. The decreasing relation could be relevant to the tiny thickness of deposition and potential size effect.

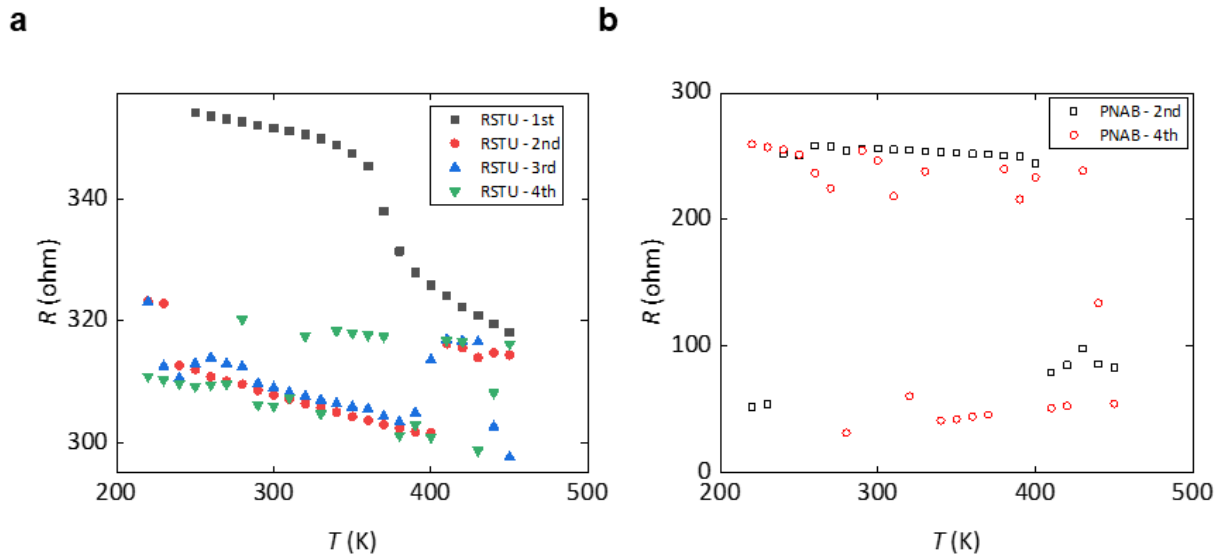

Figure 3-51a Temperature-resistance relation of emitter RSTU b Temperature-resistance relation of sensor PNAB

Table 3-11 Different measurement results.

Number	RSTU	PNAB
1	Connected	Open
2	Connected	Connected
3	Connected	Connected, no sensing current
4	Connected	Connected

Linear fitting is applied to determine the temperature coefficient of resistance (TCR), as shown in Fig. 3-52. TCR of the nanowires is calculated by, where R_0 is the resistance at 300K.

$$TCR_{PNAB} = \frac{1}{R_0}\frac{dR}{dT} = \frac{1}{256.0} \times 0.06537K^{-1} = 2.55 \times 10^{-4}K^{-1}$$

$$TCR_{RSTU} = \frac{1}{R_0}\frac{dR}{dT} = \frac{1}{307.8} \times 0.07112K^{-1} = 2.31 \times 10^{-4}K^{-1}$$

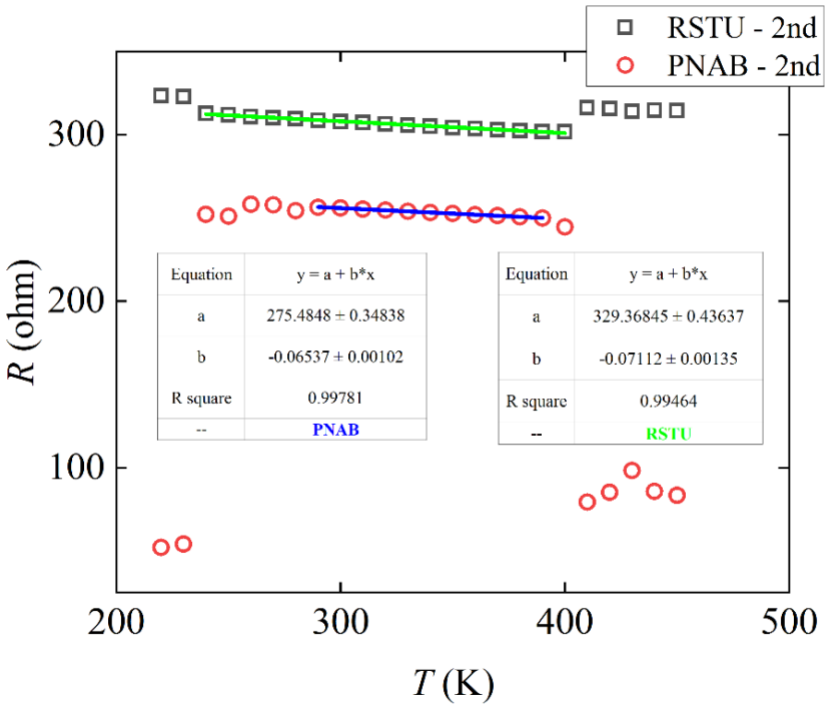

Figure 3-52 Linear fitting of R-T data.

Next, a DC heating test is applied to the emitter to determine the proper current required to heat up the emitter. As shown in Fig. 3-53a, 0.2mA current could induce about ~10K increase of the average temperature of the emitter. Note that temperature increase is proportional to the square of current based on 1D conduction model. A rough calculation indicates that ~1.41mA DC current could induce ~500K temperature increase. Thus, the DC current is increased to 1.5mA, as shown in Fig. 3-54. However, the resistance of the nanowire decreases with the low current but increases with the high current. A plausible explanation to the turning of the trend is that the TCR of this nanowire might not be a constant at a wider temperature regime so that the resistance shows a random relationship with the temperature. The next thing we will do is to calibrate the nanowire at a stage system with a wider range of temperatures for example the linkam stage system.

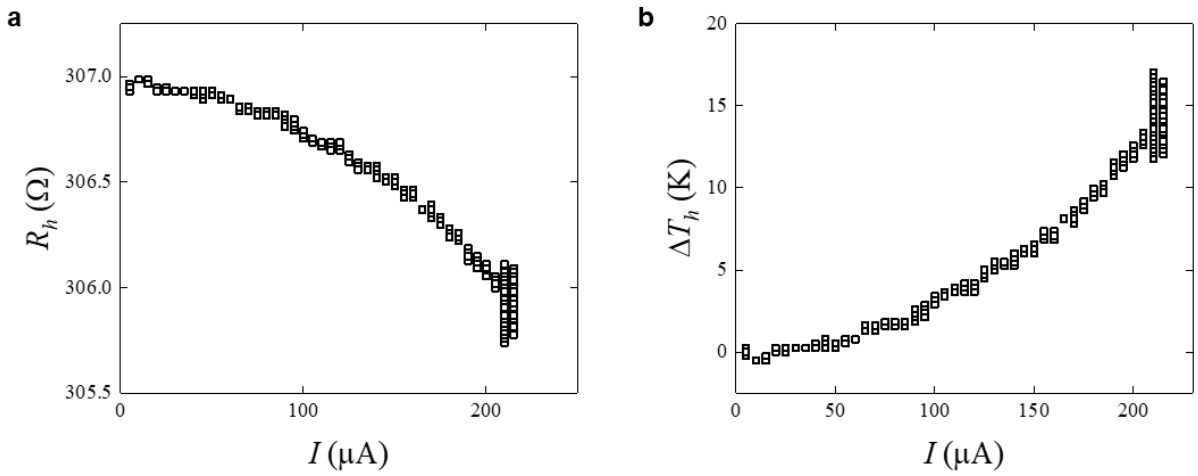

Figure 3-53 DC heating test of emitter RSTU. a resistance-current relation b corresponding increase of mean temperature.

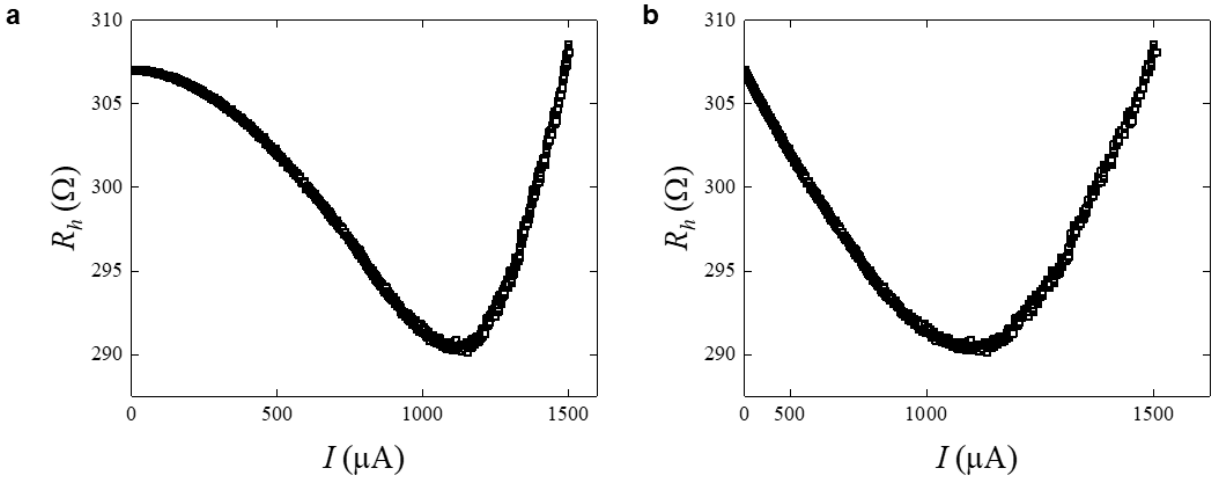

Figure 3-54 DC heating test of emitter RSTU. a linear scale of current b square scale of current.

Lastly, Wheatstone bridge is connected to the sensor to monitor the temperature change when the emitter is heated up, as shown in Fig. 3-55. The result shown in Fig. 3-55 is very interesting because a decreasing gap voltage here indicates decreasing temperature of the sensor. Next, once we figure out the temperature-resistance relationship at the full range, we will examine the validity of this result.

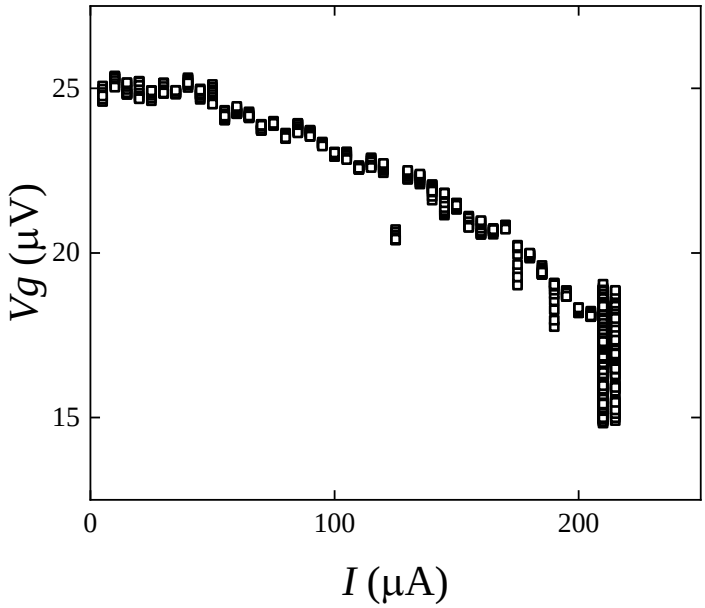

Figure 3-55 Gap voltage of Wheatstone bridge for sensor PNAB during emitter heating.

4 Conclusion and future work

4.1 Conclusion

In this dissertation, I studied the thermal emission from the nanoplasmonic structures in both near- and far-field including nanoscale plasmonic structures including metasurfaces, 2D materials, electrically-driven single emitter, etc. First of all, I first conducted numerical simulations to control the directionality of narrow-band perfect thermal emission using a nanoscale Yagi–Uda antenna consisting of nanowire arrays. Second, I designed and fabricated single plasmonic array structures and electrically-activating plasmonic device via the state-of-the-art micro and nanofabrication including e-beam lithography, photolithography, e-beam evaporation, RIE, wet etching, FIB, etc. Finally, I utilized the commericial system including microscope, FTIR, lock-in amplifier, etc. to characterize the unique properties of the nanoplasmonic structures from both thermal and optical perspectives.

4.2 Outlook and Future work

Nanoplasmonic structures have demonstrated the ability to completely alter the thermal emission power and spectrum despite the classic Planck's law. Therefore, nanoplasmonic structures have the ability and potential to compensate the disadvantage of thermal radiation in particular its randomness and incoherency. My thesis has demonstrated it from a few different perspectives and more comprehensive studies might be needed.

From the fabrication perspective, we can optimize the process flow and change the gap of device, meanwhile the repeatability of the fabrication should be further enhanced while the measurement accuracy is pushed to the limit. The fabrication of nanoantenna should be interesting for our group to explore.

From the optical and thermal measurement perspective, we can further increase SNR. Therefore we can further push the measurement limit to study the emission spectrum from even smaller nanoplasmonic structures.

References

[1] A. W. Rodriguez, M. T. H. Reid, and S. G. Johnson, Phys. Rev. B 88, 054305 (2013).

[2] A. Volokitin and B. Persson, Rev. Mod. Phys. 79, 1291 (2007).

[3] P. C. Chaumet, A. Rahmani, F. de Fornel, and J.-P. Dufour, Phys. Rev. B 58, 2310 (1998).

[4] A. C. Jones and M. B. Raschke, Nano Lett. 12, 1475 (2012).

[5] Y. De Wilde, F. Formanek, R. Carminati, B. Gralak, P.-A. Lemoine, K. Joulain, J.-P. Mulet, Y. Chen, and J.-J. Greffet, Nature 444, 740 (2006).

[6] P. Ben-Abdallah and S.-A. Biehs, Phys. Rev. Lett. 112, 044301 (2014).

[7] A. Narayanaswamy, S. Shen, and G. Chen, Phys. Rev. B 78, 115303 (2008).

[8] J. Shi, P. Li, B. Liu, and S. Shen, Appl. Phys. Lett. 102, 183114 (2013).

[9] S.-B. Wen, J. Heat Transfer 132, 072704 (2010).

[10] B. Liu and S. Shen, Phys. Rev. B 87, 115403 (2013).

[11] J. Shi, B. Liu, P. Li, L. Y. Ng, and S. Shen, Nano Lett. 15, 1217 (2015).

[12] B. Liu, Y. Liu, and S. Shen, Phys. Rev. B 90, 195411 (2014).

[13] P. Ben-Abdallah, K. Joulain, J. Drevillon, and G. Domingues, J. Appl. Phys. 106, 044306 (2009).

[14] S. Ingvarsson, L. J. Klein, Y. Au, A. James, and H. F. Hamann, Opt. Express 15, 11249 (2007).

[15] S. Shen, A. Narayanaswamy, and G. Chen, Nano Lett. 9, 2909 (2009).

[16] J. A. Schuller, T. Taubner, and M. L. Brongersma, Nat. Photonics 3, 658 (2009).

[17] J. A. Schuller, T. Taubner, and M. L. Brongersma, Nat. Photonics 3, 658 (2009).

[18] T. Inoue, M. De Zoysa, T. Asano, and S. Noda, Optica 2, 27 (2015).

[19] C. Wuttke and A. Rauschenbeutel, Phys. Rev. Lett. 111, 024301 (2013).

[20] S. Basu, Z. M. Zhang, and C. J. Fu, Int. J. Energy Res. 33, 1203 (2009).

[21] A. Rodriguez, O. Ilic, P. Bermel, I. Celanovic, J. Joannopoulos, M. Soljačić, and S. Johnson, Phys. Rev. Lett. 107, 114302 (2011).

[22] P. A. Belov, R. Marqués, S. I. Maslovski, I. S. Nefedov, M. Silveirinha, C. R. Simovski, and S. A. Tretyakov, Phys. Rev. B 67, 113103 (2003).

[23] K. Joulain, J.-P. Mulet, F. Marquier, R. Carminati, and J.-J. Greffet, Surf. Sci. Rep. 57, 59 (2005).

[24] M. Laroche, R. Carminati, and J.-J. Greffet, J. Appl. Phys. 100, 063704 (2006).

[25] A. Lenert, D. M. Bierman, Y. Nam, W. R. Chan, I. Celanovic, and E. N. Wang, Nat. Nanotechnol. 9, 126 (2014).

[26] V. A. Golyk, M. Krüger, and M. Kardar, Phys. Rev. E 85, 046603 (2012).

[27] A. Narayanaswamy, S. Shen, and G. Chen, Phys. Rev. B 78, 115303 (2008).

[28] S. Molesky and Z. Jacob, Phys. Rev. B 91, 205435 (2015).

[29] L. Zhu, A. Raman, K. X. Wang, M. A. Anoma, and S. Fan, Optica 1, 32 (2014).

[30] V. A. Golyk, M. Krüger, and M. Kardar, Phys. Rev. E 85, 046603 (2012).

[31] A. Narayanaswamy, S. Shen, and G. Chen, Phys. Rev. B 78, 115303 (2008).

[32] L. A. Falkovsky, J. Phys. Conf. Ser. 129, 012004 (2008).

[33] G. Shvets, S. Trendafilov, J. Pendry, and a. Sarychev, Phys. Rev. Lett. 99, 053903 (2007).

[34] S.-A. Biehs, P. Ben-Abdallah, F. S. S. Rosa, K. Joulain, and J.-J. Greffet, Opt. Express 19, A1088 (2011).

[35] D. Costantini, et al. "Plasmonic metasurface for directional and frequency-selective thermal emission.", Physical Review Applied 4, No. 1 (2015).

[36] T. Ribaudo, et al. "Highly directional thermal emission from two-dimensional silicon structures." Optics express 21, No. 6 (2013).

[37] Y. H. Kan, C. Y. Zhao, and Z. M. Zhang, Phys. Rev. B 99, 035433 (2019).

[38] C. A. Balanis. "Antenna theory: a review." Proceedings of the IEEE, 80, 1 (1992).

[39] L. Z. Zheng, and D. N. C. Tse. "Diversity and multiplexing: a fundamental tradeoff in multiple-antenna channels." IEEE TRANSACTIONS ON INFORMATION THEORY, 49, 5 (2003).

[40] L. C. Godara. "Application of antenna arrays to mobile communications. II. Beam-forming and direction-of-arrival considerations." Proceedings of the IEEE, 85, 8 (1997).

[41] D. S. Shiu, G. J. Foschini, M. J. Gans, and J. M. Kahn, "Fading correlation and its effect on the capacity of multielement antenna systems", IEEE Transactions on Communications, 48, 3 (2000).

[42] Y. W. Hsu, T. C. Huang, H. S. Lin, and Y. C. Lin, "Dual-polarized Quasi Yagi–Uda antennas with End Fire radiation for millimeter-wave MIMO terminals", IEEE Transactions on Antennas and Propagation, 65, No. 12 (2017).

[43] Y. W. Hsu, T. C. Huang, H. S. Lin, and Y. C. Lin, "Dual-polarized Quasi Yagi–Uda antennas with EndFire radiation for millimeter-wave MIMO terminals", IEEE Transactions on Antennas and Propagation, 65, No. 12 (2017).

[44] H. Galal, M. Agio, "Highly efficient light extraction and directional emission from large refractive-index materials with a planar Yagi-Uda antenna", IEEE Optical Materials Express, 7, No. 5 (2017).

[45] F. Liang, Z. Yang, Y. Xie, H. Li, D. Zhao, "Beam-Scanning Microstrip Quasi-Yagi–Uda Antenna Based on Hybrid Metal-Graphene Materials", IEEE Photonics Technology Lett., 30, No. 12, 2018

[46] S. Wang, Z. Hu, W. Wang, S. Qi, and W. Wu, "Analysis and design of sea‐water monopole Yagi‐Uda antenna with pattern reconfigurability", International Journal of RF and Microwave Computer-aided Engineering, 28, e21399 (2018).

[47] K. B. Crozier, A. Sundaramurthy, G. S. Kino, and C. F. Quate, "Optical antennas: Resonators for local field enhancement", J. Appl. Phys. 94, 4632-4642 (2003).

[48] P. J. Schuck, D. P. Fromm, A. Sundaramurthy, G. S. Kino, and W. E. Moerner. "Improving the Mismatch between Light and Nanoscale Objects with Gold Bowtie Nanoantennas", Phys. Rev. Lett. 94, 017402 (2005).

[49] P. M¨uhlschlegel, H. J. Eisler, O. J. F. Martin, B. Hecht, and D. W. Pohl, "Resonant Optical Antennas", Science 308, 1607 (2005).

[50] D. P. Fromm, A. Sundaramurthy, P. J. Schuck, G. Kino, and W. E. Moerner, "Gap-dependent optical coupling of single "bowtie" nanoantennas resonant in the visible", Nano Lett. 4, 957-961 (2004).

[51] S. Arslanagic, R. W. Ziolkowaski, "Highly Subwavelength, Superdirective Cylindrical Nanoantenna", Phys. Rev. Lett., 120, 237401 (2018).

[52] W. Rieger, J. J. Heremans, H. Ruan, Y. Kang, and R. Claus, "Yagi-Uda nanoantenna enhanced metal-semiconductor-metal photodetector", Appl. Phys. Lett., 113, 023102 (2018).

[53] A. Vaskin, J. Bohn, K. E. Chong, T. Bucher, M. Zilk, "Directional and Spectral Shaping of Light Emission with Mie-Resonant Silicon Nanoantenna Arrays", ACS Photonics, 5, 1359-1364 (2018).

[54] T. Kosako, H. F. Hofmann, and Y. Kadoya, "Directional control of light by a nano-optical Yagi–Uda antenna", Nature Photonics, 4, 312 - 315 (2010).

[55] J. N. Farahani, D. W. Pohl, H. J. Eisler, and B. D. Hecht, “Single quantum dot coupled to a scanning optical antenna: a tunable superemitter”, Phys. Rev. Lett., 95, 017402 (2005).

[56] B. A. Liu, W. Gong, B. W. Yu, P. F. Li and S. Shen, “Perfect thermal emission by nanoscale transmission line resonators”, Nano Lett., 17, 666-672 (2017).

[57] J. Y. Li, B. A. Liu, and S. Shen, “Tunable narrow-band near-field thermal emitters based on resonant metamaterials”, Phys. Rev. B, 96.7 (2017).

[58] B. A. Liu, and S. Shen, “Broadband near-field radiative thermal emitter/absorber based on hyperbolic metamaterials: Direct numerical simulation by the Wiener chaos expansion method”, Phys. Rev. B 87.11 (2013).

[59] B. A. Liu, J. Y. Li, S. Shen, “Resonant thermal infrared emitters in near-and far-fields”, ACS Photonics 4.6 (2017).

[60] S. M. Rytov, Y. A. Kravtsov, V. I. Tatarskii, Principles of Statistical Radiophysics, Springer-Verlag, (1989) Vol. 3

[61] C. Sauvan, et al. “Theory of the spontaneous optical emission of nanosize photonic and plasmon resonators”, Phys. Rev. Lett 110.23 (2013).

[62] B. A. Liu, Y. M. Liu, and S. Shen, “Thermal plasmonic interconnects in graphene”, Phys. Rev. B 90.19 (2014).

[63] A. W. Rodriguez, M. T. H. Reid and S. G. Johnson, “Fluctuating-surface-current formulation of radiative heat transfer: theory and applications”, Phys. Rev. B 88(2013).

[64] B. W. Yu, J. Y. Li, S. Shen, “Directional control of narrow-band thermal emission from nanoantennas,” Journal of Photonics for Energy, 9 (3), 032712 (2019).

[65] B. A. Liu, W. Gong, B. W. Yu, P. F. Li, S. Shen, “Perfect thermal emission by nanoscale transmission line resonators,” Nano Letters, 17, 2, 666-672 (2017).

[66] J. Y. Li, B. W. Yu, S. Shen, “Scale law of far-field thermal radiation from plasmonic metasurfaces,” Physical Review Letters, 124 (13), 137401 (2020).

[67] G. Shvets, S. Trendafilov, J. Pendry, and a. Sarychev, Phys. Rev. Lett. 99, 053903 (2007).

[68] J. Y. Li, B. A. Liu, and S. Shen, “Graphene surface plasmons mediated thermal radiation”, Journal of Optics 20.2 (2018).

[69] L. A. Falkovsky, J. Phys. Conf. Ser. 129, 012004 (2008).

[70] G. Shvets, S. Trendafilov, J. Pendry, and a. Sarychev, Phys. Rev. Lett. 99, 053903 (2007).

[71] A. W. Rodriguez, M. T. H. Reid, and S. G. Johnson, Phys. Rev. B 86, 220302 (2012).

[72] A. W. Rodriguez, M. T. H. Reid, and S. G. Johnson, Phys. Rev. B 86, 220302 (2012).

[73] C. Tai, IEEE Antennas and Propagation Society., and IEEE Microwave Theory and

Techniques Society., *Dyadic Green Functions in Electromagnetic Theory* (IEEE Press, 1994).

[74] J. C. Slater and G. F. Koster, Phys. Rev. 94, 1498 (1954).

[75] B. Liu, J. Li, and S. Shen, ACS Photonics 4, 1552 (2017).

[76] A. C. Jones and M. B. Raschke, Nano Lett. 12, 1475 (2012).

[77] C. R. Otey, W. T. Lau, and S. Fan, Phys. Rev. Lett. 104, 154301 (2010).

[78] S. Basu and M. Francoeur, Appl. Phys. Lett. 98, 113106 (2011).

[79] S.-A. Biehs, F. S. S. Rosa, and P. Ben-Abdallah, Appl. Phys. Lett. 98, 243102 (2011).

[80] X. Luo, T. Qiu, W. Lu, and Z. Ni, Mater. Sci. Eng. R Reports 74, 351 (2013).

[81] A. W. Rodriguez, M. T. H. Reid, and S. G. Johnson, Phys. Rev. B 88, 054305 (2013).

[82] Y. G. Zhang, et al. Fourier Transform Infrared Spectroscopy Approach for Measurements of Photoluminescence and Electroluminescence in Mid-Infrared. Review of Scientific Instruments 83, 053106 (2012).

[83] S.-A. Biehs, Eur. Phys. J. B 58, 423 (2007).

[84] G. G.Stoney. The tension of metallic films deposited by electrolysis[J]. Proceedings of the Royal Society of London. Series A, Containing Papers of a Mathematical and Physical Character, 1909, 82(553): 172-175.

[85] M. R.Ardigo, M. Ahmed, A. Besnard. Stoney formula: Investigation of curvature measurements by optical profilometer. Advanced Materials Research. Trans Tech Publications Ltd, 2014, 996: 361-366.

[86] L. N. Medgyesi-Mitschang, J. M. Putnam, and M. B. Gedera, J. Opt. Soc. Am. A 11, 1383 (1994).

[87] Z. Feng, H. Liu. Generalized formula for curvature radius and layer stresses caused by thermal strain in semiconductor multilayer structures[J]. Journal of Applied physics, 1983, 54 (1): 83-85.

[88] L. Shi, et al. Measuring thermal and thermoelectric properties of one-dimensional nanostructures using a microfabricated device. J. Heat Transfer 125, 881–888 (2003).

[89] R. Shrestha, et al. Crystalline polymer nanofibers with ultra-high strength and thermal conductivity. Nat. Commun. 9, 1–9 (2018).

[90] H. Wang, et al. Experimental study of thermal rectification in suspended monolayer graphene. Nat. Commun. 8, 15843 (2017).

[91] D. Thompson, et al. Hundred-fold enhancement in far-field radiative heat transfer over the blackbody limit. Nature 561, 216–221 (2018).

[92] M. C. Wingert, Z. C. Y. Chen, S.Kwon, J. Xiang, & R. Chen, Ultra-sensitive thermal conductance measurement of one-dimensional nanostructures enhanced by differential bridge. Rev. Sci. Instrum. 83, 024901 (2012).